DEVELOPMENT OF A MILI-NEWTON LEVEL THRUST STAND FOR THRUST MEASUREMENTS OF ELECTRIC PROPULSION SYSTEMS AND UK90 HALL EFFECT THRUSTER

by

Uğur Kokal

B.S., Mechanical Engineering, Boğaziçi University, 2015

Submitted to the Institute for Graduate Studies in
Science and Engineering in partial fulfillment of
the requirements for the degree of
Master of Science

Graduate Program in Mechanical Engineering
Boğaziçi University

2019

DEVELOPMENT OF A MILI-NEWTON LEVEL THRUST STAND FOR THRUST MEASUREMENTS OF ELECTRIC PROPULSION SYSTEMS AND UK90 HALL EFFECT THRUSTER

APPROVED BY:

Assoc. Prof. Murat Çelik (Thesis Supervisor)	.....
Assoc. Prof. Şebnem Özüpek	.....
Assist. Prof. Arif Karabeyoğlu	.....

DATE OF APPROVAL: 18.12.2018

ACKNOWLEDGEMENTS

I would like to express my gratitude to my advisor Prof. Murat Çelik for his continuous support of my research, and for his motivation, enthusiasm, and immense knowledge. I also want to thank him for allowing me to explore the broad field of propulsion and experimentation. I have learned a lot about scientific research and academic world during laboratory hours.

I would like to thank the members of my thesis committee, Prof. Şebnem Özüpek and Prof. Arif Karabeyoğlu for their time and help in the preparation process of this dissertation.

I am grateful to Prof. Hüseyin Kurt for his support, patience and immense knowledge over a broad area. His willingness to share his knowledge contributed greatly to this research.

I would like to thank my colleague Nazlı Turan for her invaluable contributions and sincere friendship during our studies. Also, I am grateful to Mehmet Serhan Yıldız for his constant support and friendship.

I would like to acknowledge the financial support of Scientific and Technological Research Council of Turkey (TÜBİTAK) under the project number 214M572, and also Bogazici University Scientific Projects Office (BAP) under the project number BAP-11482.

Finally, I must express my gratitude to my mother, Gülden Kokal, and my father, Hasan Kokal for providing me with invaluable support and continuous encouragement throughout my years of study and through the process of researching and writing this thesis. This accomplishment would not have been possible without them.

ABSTRACT

DEVELOPMENT OF A MILI-NEWTON LEVEL THRUST STAND FOR THRUST MEASUREMENTS OF ELECTRIC PROPULSION SYSTEMS AND UK90 HALL EFFECT THRUSTER

Since 1960's, electric propulsion systems have been used on spacecraft for orbital maneuvers and deep space missions. Electric propulsion systems can operate at high specific impulse levels and can deliver very high delta-V in a mission. However, they generate very low thrust. In this study, a thrust stand is developed and built for the thrust measurements of electric thrusters. The thrust stand that is developed is based on inverted pendulum configuration, and can measure thrust forces at mili-Newton levels. Thrust stand design is optimized for high sensitivity at the desired thrust levels. By using the thrust stand, measurements are conducted for the electric propulsion systems that are developed so far in BUSTLab (Bogazici University Space Technologies Laboratory). Also, development process of UK90 Hall thruster is investigated in detail. UK90 Hall thruster is an SPT type Hall thruster with 1500 W power level, which is suitable for orbital maneuvers such as station keeping and orbit transfers. Magnetic and thermal analysis are conducted for Hall thruster and design parameters are optimized for high efficiency. Thermal analyses are conducted for the hollow cathode that is developed at BUSTLab. Also, with the experience gained from the previous radio-frequency ion thruster designs, a new design is developed for BURFIT-80 ion thruster. The RF ion thruster is manufactured and tested.

ÖZET

ELEKTRİKLİ İTKİ SİSTEMLERİ İÇİN MİLİNEWTON SEVİYESİ İTKİ ÖLÇÜM SİSTEMİNİN VE UK90 HALL ETKİSİ İTKİ SİSTEMİNİN GELİŞTİRİLMESİ

Elektrikli itki sistemleri 1960'lardan beri uzay araçlarında yörünge manevraları ve derin uzay görevlerinde kullanılmaktadır. Elektrikli itki sistemleri yüksek özgül impuls değerlerine sahip olabilmeleri sayesinde bir görev sırasında yüksek delta-V sağlayabilmektedir. Ancak düşük itki kuvvetleri üretmektedirler. Bu çalışmada elektrikli itki sistemlerinin itki ölçümleri için bir itki ölçüm sistemi geliştirilmiştir. Geliştirilen itki ölçüm sistemi ters sarkaç mekanizmasına sahiptir ve mili Newton seviyelerinde itkileri ölçebilmektedir. İtki ölçüm sistemi ölçülecek itki seviyelerinde yüksek hassasiyete sahip olacak şekilde optimize edilmiştir. Bu ölçüm sistemi kullanılarak şu ana kadar BUSTLab (Boğaziçi Üniversitesi Uzay Teknolojileri Laboratuvarı) bünyesinde geliştirilen elektrikli itki sistemlerinin testleri yapılmıştır. Ayrıca UK90 Hall itki motorunun geliştirilme süreci detaylıca anlatılmıştır. UK90 Hall itki sistemi 1500 W güç seviyesinde SPT tipi bir Hall itki motorudur ve uyduların yörünge koruma ve yörünge transfer görevlerine uygundur. Hall itki sistemi için manyetik ve ısıl analizler yapılmış ve tasarım parametreleri yüksek verim için optimize edilmiştir. BUSTLab'da geliştirilmiş olan oyuk katot için de ısıl analizler yapılmıştır. Ayrıca önceki radyofrekans iyon motoru tasarımlarından elde edinilen deneyimler ışığında BURFIT-80 iyon motoru için yeni bir tasarım yapılmıştır. RF iyon motoru üretilmiş ve test edilmiştir.

TABLE OF CONTENTS

ACKNOWLEDGEMENTS iii
ABSTRACT iv
ÖZET v
LIST OF FIGURES x
LIST OF TABLES xix
LIST OF SYMBOLS xx
LIST OF ACRONYMS/ABBREVIATIONS xxiii
1. INTRODUCTION 1
1.1. Chemical Propulsion Systems 4
1.1.1. Solid Propellant 4
1.1.2. Liquid Propellant 5
1.1.3. Hybrid Rockets 5
1.2. Electric Propulsion Systems 6
1.2.1. Electrothermal Systems 8
1.2.1.1. Resistojets 8
1.2.1.2. Arcjets 9
1.2.1.3. Microwave Electrothermal Thrusters 9
1.2.2. Electrostatic Propulsion Systems 10
1.2.2.1. Ion Thrusters 11
1.2.2.2. Hall Thrusters 12
1.2.2.3. Electrospray and FEEP Thrusters 13
1.2.3. Electromagnetic Propulsion Systems 13
1.3. History of Electric Propulsion 14
1.4. Thrust Measurements 18
1.5. Thrust Stand Configurations 19
1.5.1. Hanging Pendulum Thrust Stand 19
1.5.2. Inverted Pendulum Thrust Stand 19
1.5.3. Torsional Pendulum Thrust Stand 20
1.5.4. Folded Pendulum Thrust Stand 20

1.6. Thrust Stands in Literature 21
1.6.1. ONERA Micro-Newton Thrust Stand 21
1.6.2. NASA Glenn Research Center High Power Trust Stand 22
1.6.3. DLR Electric Propulsion Test Facility Thrust Stand 24
1.6.4. Astrium Highly Precise Micro-Newton Thrust Stand 25
1.6.5. ESA Micro-Newton Thrust Balance 28
1.6.6. Thales Alenia Space Italia Nanobalance Facility 28
1.6.7. University of Southampton Thrust Balance 30
1.6.8. University of Southampton High Accuracy Impulsive Thrust Stand 30
1.6.9. FOTEC μN Thrust Stand 32
1.6.10. ARC Seibersdorf Research GmbH Thrust Stand 33
1.6.11. University of Tokyo Thrust Stand for Low Impulse Measurement 34
1.7. Contribution of this Work 35
2. DEVELOPMENT OF THRUST STAND 37
2.1. Design Constraints and Requirements 37
2.2. Thrust Stand Characteristics 38
2.2.1. Natural Frequency 38
2.2.2. Stiffness 39
2.2.3. Settling Time 40
2.3. Thrust Stand Design 40
2.4. Modelling and Analysis of Thrust Stand 43
2.4.1. General Model of Thrust Stand 43
2.4.2. Numerical Solution of the Thrust Stand Response 49
2.4.3. Analytical Solution of the Thrust Stand Response 57
2.4.4. Analytical Model of Thin Flexures 59
2.4.5. Numerical Model of Thrust Stand with Flexures 63
2.4.6. Strength Analysis of Flexures 64
2.5. Components of the Thrust Stand 67
2.5.1. Flexural Strips 67
2.5.2. Sensors 68
2.5.2.1. Displacement Sensor 68

2.5.2.2. Thermocouples 70
2.5.3. Calibration System 71
2.5.4. Damping System 74
2.5.5. Counterweights 75
2.5.6. Control System 76
2.5.7. Cabling and Piping 77
2.5.8. Main Linear Stage 77
2.6. Thermal Analysis and Thermal System Design of Thrust Stand 79
2.7. Thrust Stand Operational Procedures 81
2.7.1. Thrust Stand Setup 81
2.7.2. Safety Locks 82
2.7.3. Counterweight Adjustment 82
2.7.4. Thrust Stand Positioning with Linear Stage 83
2.7.5. Calibration of Thrust Stand 83
2.8. Uncertainty Analysis 85
3. DEVELOPMENT OF UK90 HALL THRUSTER 87
3.1. Internal Cathode Configuration 88
3.2. Scaling of Hall Thruster 90
3.3. Theoretical Operational Characteristics 93
3.4. Magnetic Topology of Hall Thruster 98
3.5. Magnetic Modelling of Hall Thruster 101
3.6. BUSTLab Hollow Cathode 105
3.7. Thermal Modelling of Hall Thruster 111
3.8. UK90 Hall Thruster Design and Manufacture 114
4. EXPERIMENTS AND RESULTS 121
4.1. Experimental Setup 121
4.2. HK40 Hall Thruster 122
4.3. Microwave Electrothermal Thruster 125
4.4. UK90 Hall Thruster 128
5. CONCLUSION 130
5.1. Future Work 134

REFERENCES 136
APPENDIX A: BURFIT-80 ION THRUSTER DESIGN 149

LIST OF FIGURES

Figure 1.1. Propulsion Systems 1

Figure 1.2. Thrust and specific impulse values of experimental and flight propulsion systems. [1] 6

Figure 1.3. Applications of electric propulsion systems according to power consumption and specific impulse [2] 8

Figure 1.4. Commonly used electric propulsion systems [3] 9

Figure 1.5. a) 3D drawing of MET, b) MET operation with nitrogen propellant 10

Figure 1.6. Schematic of an RF ion thruster [4] 12

Figure 1.7. Schematic of a Hall thruster [5] 13

Figure 1.8. Operational parameters of propulsion systems that are used in space [6] 14

Figure 1.9. Distribution of GEO satellites according to the Hall thrusters [7] . 17

Figure 1.10. Torsional pendulum thrust stand concept [8] 20

Figure 1.11. Kinematic diagram of the folded pendulum concept [9] 21

Figure 1.12. Configuration of the ONERA Micro-Newton Balance [10] 22

Figure 1.13. Schematic diagram of the inverted pendulum thrust stand of NASA Glenn [11] 23

Figure 1.14. Waterfall configuration of power lines. [11] 24

Figure 1.15. 3D model of the mechanical parts of the thrust stand (left) [12], thrust stand in its finished state (right) [13] 25

Figure 1.16. a) Cold gas test setup in DLR vacuum chamber [13], Ion engine mounted on the thrust stand in DLR vacuum chamber [12] 26

Figure 1.17. Parallel arms of the inverted pendulum thrust stand [14]. 27

Figure 1.18. Pictures of the whole Astrium thrust stand assembly, outside of the vacuum chamber. [14] 27

Figure 1.19. Micro-Newton Thrust Balance assembly installed on base plate [15] 28

Figure 1.20. Block diagram of the nano-balance [16] 29

Figure 1.21. Nano-Balance test set up [16] 30

Figure 1.22. Complete thrust stand assembly schematic [17] 31

Figure 1.23. Design of the torsional thrust balance [18] 31

Figure 1.24. FOTEC μN Torsion thrust balance [19] 32

Figure 1.25. Test setup of FOTEC thrust balance at ESTEC [19] 33

Figure 1.26. ARC-SR μN thrust balance [20] 33

Figure 1.27. Schematic diagram of the thrust stand. [21] 34

Figure 2.1. Example of Fourier Transform used to evaluate the natural frequency [18] 39

Figure 2.2. Counterbalanced Inverted Double Pendulum Concept 41

Figure 2.3. Torsional Pivot Bearings 42

Figure 2.4. 3D drawing of Thrust Stand with HK40 Hall Thruster 42

Figure 2.5. Free Body Diagram of Thrust Stand 44

Figure 2.6. Free Body Diagram of Upper Plate 45

Figure 2.7. Free Body Diagram of Bottom Plate 45

Figure 2.8. Free Body Diagram of Rear Plate (Front Plate is also similar) . . 45

Figure 2.9. Thrust Balance Response with 10 mN Thrust and Base Excitation with Frequency of 1 Hz 50

Figure 2.10. Thrust Stand Response vs. Stiffness at 10 mN Thrust 52

Figure 2.11. Thrust Stand Response vs. Thrust and Stiffness 52

Figure 2.12. Thrust Stand Response vs. Mass Difference and Stiffness 53

Figure 2.13. Settling Time vs. Damping Constant 54

Figure 2.14. Overshoot Rate vs. Damping Constant 55

Figure 2.15. Natural Frequency of the Thrust Stand vs. Pivot Stiffness 55

Figure 2.16. Transmissibility of the Thrust Stand 56

Figure 2.17. Transmissibility vs. Vertical Mass Difference 57

Figure 2.18. Simplification of the pendulum structure as one strip and a pendulum arm (left), free body diagram of the strip (right) 60

Figure 2.19. Bending diagrams of flexural elements 61

Figure 2.20. Finite element modelling of thrust stand 63

Figure 2.21. Finite element solutions of thrust stand with 0.1 mm flexure thickness for 20 mN thrust, a) Contour plot of displacement of pendulum structure, b) Side view of pendulum deflection 65

Figure 2.22. Bending of the flexural strips, von Mises stress within the flexures are shown for applied thrust of 20 mN 65

Figure 2.23. Displacement for 0.1 mm flexure thickness a) at different thrust levels, b) at different flexure thickness values 66

Figure 2.24. Transient displacement of thrust stand with 0.1 mm flexure thickness for 20 mN thrust 66

Figure 2.25. 3D drawing of flexural strips a) Between the pendulum and support frame, b) Between the pendulum and upper platform 67

Figure 2.26. LVDT displacement sensor 68

Figure 2.27. 3D drawing of the displacement sensor assembly 69

Figure 2.28. Displacement sensor assembly and counterweights 70

Figure 2.29. Load cell that is used in calibration 71

Figure 2.30. Initial calibration mechanism design with load cell and voice coil, and LVDT assembly 72

Figure 2.31. 3D drawing of the calibration mechanism with load cell and linear stage 73

Figure 2.32. Side view of thrust stand with RF Ion Thruster 74

Figure 2.33. Eddy current damping system: Electromagnets and copper plate that is attached to the bottom plate 75

Figure 2.34. Control hardware 76

Figure 2.35. Control system schematic 77

Figure 2.36. Waterfall cabling and piping configuration 78

Figure 2.37. Thrust stand mounted on the linear stage 79

Figure 2.38. Thermal insulation of thrust stand 80

Figure 2.39. Thermal analysis of thrust stand: a) 40 W cathode power, b) 40 W cathode power with radiation shield, c) 200 W cathode power . 81

Figure 2.40. Thrust stand components in vacuum chamber 82

Figure 2.41. Thrust stand outer frame 83

Figure 2.42. Safety locks 84

Figure 2.43. Calibration Algorithm 84

Figure 2.44. Calibration data with linear fit and 95% prediction interval 86

Figure 3.1. 3D drawing of Hall thruster with internal hollow cathode configuration 87

Figure 3.2. Hall thruster voltage schematic [22] 88

Figure 3.3. BUSTLab hollow cathode 90

Figure 3.4. Hall thruster operation schematic [22] 92

Figure 3.5. Numerical simulation results of a magnetically shielded thruster: Plasma potential is on the left and electron temperature is on the right [23] 100

Figure 3.6. 3D mesh grid of Hall thruster 102

Figure 3.7. Thruster magnetic model design parameters 103

Figure 3.8. Parametric sweep channel width, a) 12 mm, b) 16 mm, c) 20 mm . 103

Figure 3.9. Parametric sweep of magnetic pole thickness, a) 2 mm, b) 4 mm, c) 6 mm 104

Figure 3.10. Parametric sweep of the gap between magnetic shields and BN channel, a) 0.5 mm, b) 2.5 mm, c) 4.5 mm 104

Figure 3.11. Parametric sweep of the gap between magnetic shields and poles, a) 1 mm, b) 2 mm, c) 3 mm 105

Figure 3.12. Parametric sweep of magnetic shield thickness, a) 1 mm, b) 3 mm, c) 5 mm 105

Figure 3.13. a) Optimized magnetic topology in discharge channel, b) Magnetic flux density (G) along the discharge channel in axial direction . . 106

Figure 3.14. Emission current densities of BaO-W and LaB_6 vs. temperature [24] 107

Figure 3.15. A schematic of cathode operation mechanism 108

Figure 3.16. Mesh grid of the axisymmetric 2D computational domain of cathode 108

Figure 3.17. Thermal conductivity and surface emissivity of cathode materials [25] 109

Figure 3.18. a) Temperature distribution in the cathode, b) Heat flux in the cathode 110

Figure 3.19. a) Radiosity of cathode inner surfaces, b) Electrical potential distribution (V) in the orifice region of the cathode 111

Figure 3.20. Mesh grid of thermal analysis and heat inputs 112

Figure 3.21. Thermal analysis of thruster: a) Without cathode power, b) With cathode power 113

Figure 3.22. 3D drawing of Hall thruster with radiator plate 114

Figure 3.23. Thermal analysis of thruster with radiator 115

Figure 3.24. 3D drawings of Hall thruster 116

Figure 3.25. Magnetic circuit assembly with inner ceramic spool 117

Figure 3.26. a) Anode assembly, b) Anode mounted inside discharge channel . 118

Figure 3.27. a) Mounting of support backplate and cathode, b) Cabling of Hall thruster 118

Figure 3.28. Completed assembly of Hall thruster with radiator (left) and without radiator (right) 119

Figure 3.29. Magnetic field measurements with Gaussmeter 119

Figure 3.30. Magnetic flux density (Gauss) at the discharge channel exit for different coil currents 120

Figure 4.1. BUSTLab vacuum chamber 121

Figure 4.2. a) HK40 Hall thruster, b) HK40 Hall thruster during operation . . 122

Figure 4.3. HK40 Hall thruster mounted on thrust stand 123

Figure 4.4. Thrust and specific impulse characteristics of HK40 Hall thruster . 124

Figure 4.5. a) Microwave electrothermal thruster, b) MET during operation . 125

Figure 4.6. MET mounted on the thrust stand 126

Figure 4.7. Performance characteristics of MET 127

Figure 4.8. Thrust characteristics of MET 127

Figure 4.9. Initial operation on UK90 Hall thruster 128

Figure 4.10. Front view of thruster operation 129

Figure 4.11. Plume of internal cathode 129

Figure A.1. BURFIT-80 Ion Thruster with Hollow Cathode 149

Figure A.2. Section view of BURFIT-80 Ion Thruster 150

Figure A.3. Copper antenna wrapped around the discharge channel 151

Figure A.4. Exploded view of BURFIT-80 Ion Thruster 152

Figure A.5. Operation of BURFIT-80 Ion Thruster 152

LIST OF TABLES

Table 3.1. Operational parameters and dimensions of various Hall thrusters [26–32] 91

Table 4.1. Performance characteristics of HK40 Hall thruster 124

LIST OF SYMBOLS

A	Area
A_x	Horizontal excitation amplitude
A_y	Vertical excitation amplitude
B	Magnetic Field
c	Damping constant
c_{eddy}	Damping constant
D	Channel outer diameter
E	Electric field
e	Elementary charge
F	Force
F_{eddy}	Eddy damping force
F_{thrust}	Thrust generated by the thruster
F_x	Horizontal force
F_y	Vertical force
g_0	Gravitational acceleration on Earth's surface
H	Arm length of pendulum
$h_{thruster}$	Distance between thrust vector and center of gravity of the upper plate
I	Area moment of inertia
I_d	Discharge current
I_{sp}	Specific impulse
I_w	Ion flow to walls
J_t	Moment of inertia
j	Emission current density
k	Stiffness
L	Channel Length
M	Dry mass of spacecraft
M_a	Atomic mass of propellant
M_0	Initial mass of spacecraft

M_{dif}	Mass difference between upper and lower parts of thrust stand
M_f	Final mass of spacecraft
M_p	Propellant mass
m	Electron mass
$\dot{m}$	Propellant mass flow rate
$\dot{m}_a$	Anode mass flow rate
$\dot{m}_i$	Ion mass flow rate
m_{cw}	Counterweight mass
$m_{thruster}$	Thruster mass
P_a	Power loss to anode
P_d	Discharge power
P_i	Power loss to ionization
P_w	Power loss to walls
P_b	Beam kinetic energy
R^2	Coefficient of Determination
r_e	Larmor radius
q	Electric charge
T	Thrust
T_0	Torque
T_e	Electron temperature in Kelvin
T_{eV}	Electron temperature in eV
T_w	Emitter material wall temperature
t	Time
V	Velocity
V_b	Beam acceleration voltage
V_c	Cathode coupling voltage
V_d	Discharge voltage
V_e	Exhaust velocity
V_i	Ionization energy
v	Particle velocity
v_{th}	Thermal velocity

w	Channel width
x_b	Horizontal excitation
y_b	Vertical excitation
ΔV	Velocity change
η_a	Anode efficiency
η_c	Cathode efficiency
η_i	Power fraction loss to ionization
η_j	Current efficiency
$\eta_l oss$	Total heat loss
η_o	Electrical utilization efficiency
η_T	Total efficiency
η_v	Voltage utilization
η_w	Power fraction loss to walls
η_ϕ	Beam divergence loss
ω_b	Frequency of vibration
ω_c	Cyclotron frequency
ϕ	Work function
σ	Stress
θ	Deflection angle

LIST OF ACRONYMS/ABBREVIATIONS

2D	Two Dimensional
3D	Three Dimensional
AST	Advanced Space Technologies
BaO-W	Barium-Oxide Impregnated Tungsten
BHT	Busek Hall Effect Thruster
BN	Boron Nitride
BURFIT	Bogazici University Radio-Frequency Ion Thruster
BUSTLab	Bogazici University Space Technologies Laboratory
CAD	Computer-Aided Design
DART	Double Asteroid Redirection Test
DC	Direct Current
DLR	Deutsches Zentrum für Luft- und Raumfahrt
ECR	Electron Cyclotron Resonance
EMI	Electromagnetic Interference
ESA	European Space Agency
ESTEC	European Space Research and Technology Centre
FEEP	Field Emission Electric Propulsion
GEO	Geostationary Earth Orbit
GTO	Geostationary Transfer Orbit
H_2O_2	Hydrogen Peroxide
HERMeS	Hall Effect Rocket with Magnetic Shielding
ICP	Inductively Coupled Plasma
JAXA	Japan Aerospace Exploration Agency
JPL	Jet Propulsion Laboratory
LaB_6	Lanthanum Hexaboride
LEO	Low Earth Orbit
LH_2	Liquid Hydrogen
LISA	Laser Interferometer Space Antenna

LOX	Liquid Oxygen
LVDT	Linear Variable Differential Transformer
MET	Microwave Electrothermal Thruster
MPD	Magnetoplasmadynamic
N_2H_4	Hydrazine
NASA	National Aeronautics and Space Administration
NGGM	Next Generation Gravity Mission
NSTAR	NASA Solar Electric Propulsion Technology Applications Readiness
ONERA	Office National d'Etudes et de Recherches Aerospatiales
PEEK	Polyether Ether Ketone
PID	Proportional Integral Derivative
PPT	Pulsed Plasma Thruster
RF	Radio Frequency
RIT	Radiofrequency Ion Thruster
SMART	Small Mission for Advanced Research in Technology
SCCM	Standard Cubic Centimeters per Minute
SPT	Stationary Plasma Thruster
XIPS	Xenon Ion Propulsion System

1. INTRODUCTION

Spacecraft perform their maneuvers by using propulsion systems. These maneuvers can be the launch of the spacecraft from the Earth's surface with a launch vehicle or space maneuvers such as orbit maintenance and orbital transfers. Propulsion systems can be separated according to their energy source and operation principles. Commonly used propulsion systems are chemical and electric propulsion systems as shown in Figure 1.1. In chemical propulsion systems, propellants are combusted and then accelerated by expanding through a converging-diverging nozzle. In electric propulsion, electrical energy that is supplied from solar panels or nuclear reactors is converted to the kinetic energy. Also, there are alternative experimental propulsion systems such as nuclear rockets and solar sails [33].

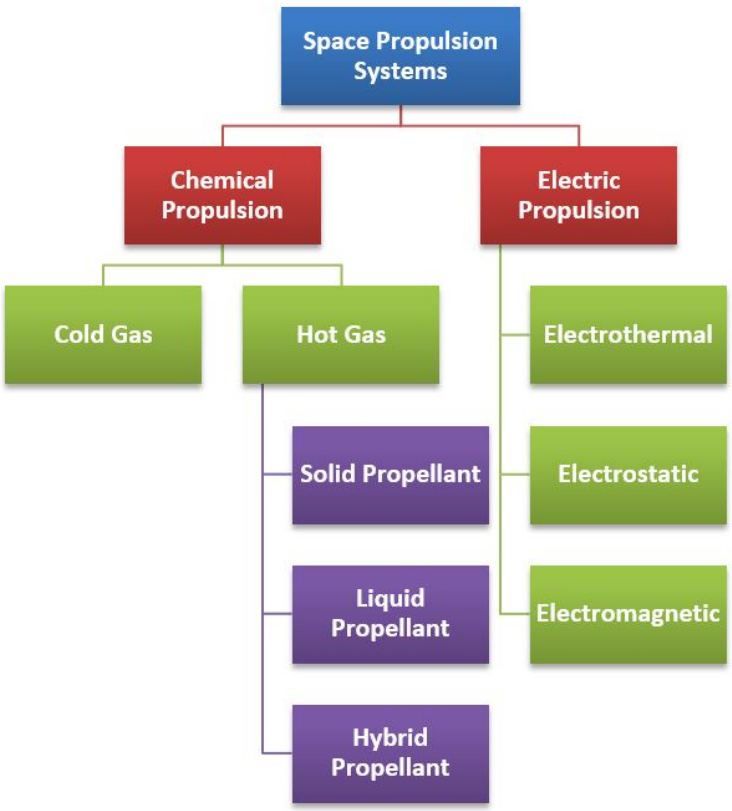

Figure 1.1. Propulsion Systems

Working principle of propulsion systems is based on the conversation of momentum. When a mass is accelerated and ejected from a spacecraft, thrust is generated and the spacecraft is accelerated in opposite direction. Thrust can be defined by using Newton's 2nd Law:

$$Force = M\frac{dV}{dt} \tag{1.1}$$

where, $Force$ is the applied thrust (T) to the spacecraft, M is the mass of the spacecraft, and $\frac{dV}{dt}$ is the velocity change of the spacecraft. The thrust applied to the spacecraft is equal and in opposite direction with the force that accelerates the propellant in opposite direction. Thus, thrust can be described as:

$$T = \dot{m}V_e \tag{1.2}$$

where, T is thrust, $\dot{m}$ is propellant mass flow rate and V_e is exhaust velocity of the expelled propellant. As the propellant carried on the spacecraft, total mass of the spacecraft changes with the propellant consumption. Considering this situation, Russian school teacher Konstantin Tsiolkovsky (1857-1935) derived the rocket equation (Equation 1.3) in his article "Investigation of Universal Space by Means of Reactive Devices" in 1903 [34]. It can be said that modern rocketry and astronautics started with Tsiolkovsky's article.

$$\Delta V = V_e ln\left(\frac{M_0}{M_f}\right) \tag{1.3}$$

where, ΔV is velocity change, V_e is exhaust velocity of the propellant, M_0 is the initial mass of the spacecraft and M_f is the final mass of the spacecraft. Propellant mass is defined as:

$$M_p = M_0 - M_f \tag{1.4}$$

where, M_p is the propellant mass that is expelled during the maneuver. Generally, effectiveness of the propulsion systems are described with the specific impulse (I_{sp}), which is usually expressed in seconds [33].

$$I_{sp} = \frac{T}{\dot{m} g_0} = \frac{V_e}{g_0} \tag{1.5}$$

where, T is thrust, $\dot{m}$ is mass flow rate of propellant, g_0 is gravitational acceleration on Earth's surface and V_e is exhaust velocity. Specific impulse describe how efficiently the propulsion system accelerates the propellant and generates thrust. Higher I_{sp} values mean that the propulsion system produce thrust with less propellant. As the spacecraft mass is one of the critical cost determining factors, specific impulse value of the propulsion system is important. By substituting equation 1.5 into equation 1.3, an ideal rocket equation with I_{sp} term can be found:

$$\Delta V = I_{sp} g_0 ln \left(\frac{M_0}{M_f} \right) \tag{1.6}$$

As can be seen in equation 1.6, I_{sp} values of propulsion systems are critical for the maneuvers of spacecraft. Missions that requires high ΔV values such as deep space missions require high I_{sp} values.

1.1. Chemical Propulsion Systems

In a chemical thruster, the maximum available exhaust velocity and therefore I_{sp} is limited with the energy density of the propellant. Thrust is generated by accelerating a heated propellant through a converging-diverging nozzle. Propellant is heated with chemical reactions inside combustion chambers. Chemical propulsion systems can be separated into solid, liquid and hybrid systems [2].

1.1.1. Solid Propellant

Solid propellant rockets utilize solid grain propellants that include both oxidizer and fuel. The propellant grain is shaped as a hollow cylinder in most solid rockets. When the combustion is initiated with an igniter, the propellant starts to burn, thus pressure and temperature within the rocket increase. Hot pressurized combustion products are expanded through a converging-diverging nozzle. Specific impulses up to 300 s may be achieved with solid propellants.

Major advantage of solid rockets is that they have few or no moving parts. Also, as the propellant is stored in solid form, they require less volume and can be stored for long durations. However, the major drawback of the solid rockets is that once the combustion is initiated, it is impossible to control or stop the combustion. Also, as both the fuel and oxidizer exist together in the propellant grain, solid rockets have inherent storage and operational risks. Solid rockets are used commonly in first stages of launch vehicles. They are also used in ballistic missiles [2].

1.1.2. Liquid Propellant

In liquid rocket engines, reaction of one or more propellants in liquid form generates high pressure and hot gases in a combustion chamber. Thrust is generated by accelerating the reaction products through a nozzle. Propellants can be pressurized with turbopumps or are stored pressurized in tanks. Main advantages of liquid rocket engines are that they are throttleable and can be reignited several times and can provide higher specific impulses than solid rockets. Liquid rocket engines are separated into two categories: monopropellant and bipropellant rockets.

In monopropellant rockets, a single propellant such as hydrazine (N_2H_4) or hydrogen peroxide (H_2O_2) is decomposed exothermically as it flows through a catalytic bed. Monopropellant rockets operate with I_{sp} levels up to 240 s. They are generally used for attitude control of the spacecraft.

In bipropellant rockets, fuel and oxidizer are mixed and burned in a combustion chamber. Commonly used fuels are liquid hydrogen (LH_2) and kerosene, while liquid oxygen (LOX) is the most common oxidizer. Bipropellant rockets can be used at launch vehicles and also utilized for orbital maneuvers. Their I_{sp} values are between 270-465 s. Highest practical I_{sp} that can be achieved with bipropellants is about 465 s with LOX/LH_2 combustion [34].

1.1.3. Hybrid Rockets

A third class of the chemical propulsion systems is the hybrid rockets, which combines some properties of liquid and solid rocket engines. In hybrid rockets, solid fuel is burned with a liquid oxidizer. Liquid oxidizer is stored in an oxidizer tank and fed to the solid fuel grain. Hybrid rockets can provide specific impulses up to 330 s, also can be restarted and throttled by controlling the oxidizer flow rate. They offer a potentially lower cost and safer operation than liquid and solid rocket engines [35].

1.2. Electric Propulsion Systems

Unlike chemical propulsion, electrical propulsion does not depend to the energy density of the propellant. In electric propulsion, energy supplied from an external source such as solar energy or nuclear reactors, is converted to the kinetic energy of the propellant, thus much higher I_{sp} levels can be achieved as shown in Figure 1.2 [36].

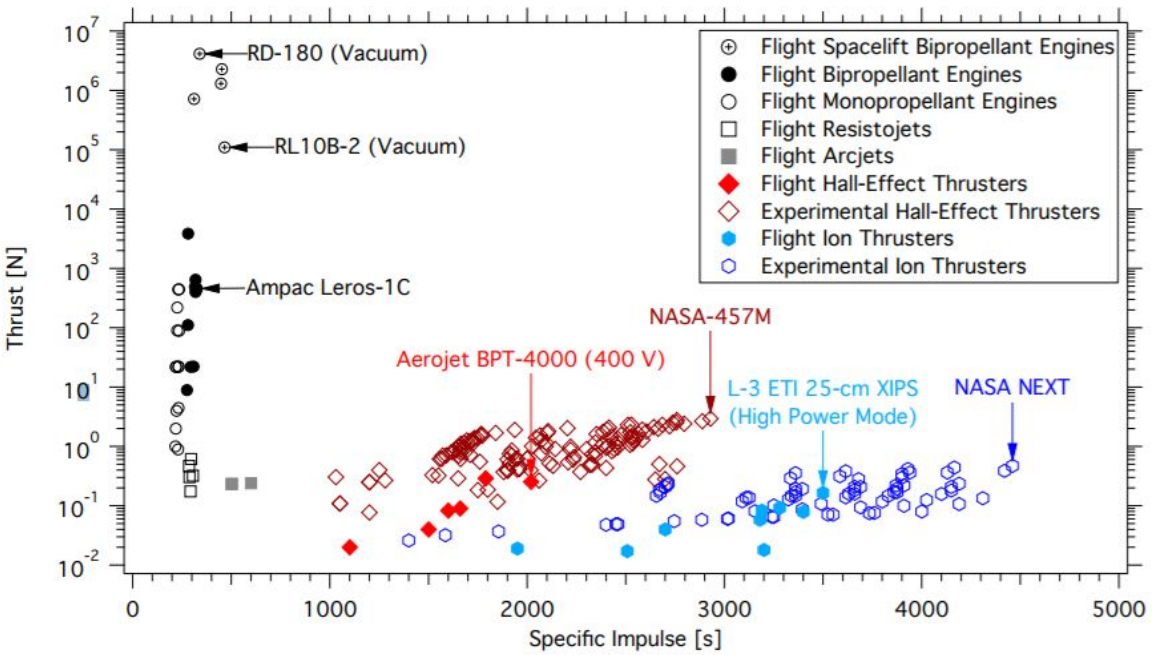

Figure 1.2. Thrust and specific impulse values of experimental and flight propulsion systems. [1]

Electric propulsion systems provide lower thrusts and have low thrust/mass ratio, therefore they cannot be used in launch vehicles. However, they are suitable for in-space applications. These applications are shown in Figure 1.3 and can be summarized as:

- Station keeping: Electric propulsion systems are commonly used for north-south and east-west station keeping maneuvers for GEO (Geostationary Earth Orbit) satellites. In a typical GEO communication satellite, usually four thruster systems are placed at four corners of the satellites for station keeping.

North-south station keeping maneuvers require 45-55 m/s ΔV per year, while east-west station keeping maneuvers require about 3-6 m/s per year [33]. Usually at GEO satellites thrusters are operated once for every two week. Electric propulsion systems are used in LEO (Low Earth Orbit) satellites for both station keeping and drag compensation, which requires ΔV between 60 and 500 m/s.

- Attitude control: Electric propulsion systems can be used to control the attitude, which means the orientation, of the satellite. In precise operations low thrust systems such as electrospray and FEEP (Field Emission Electric Propulsion) thrusters can be used for precise control of satellite attitude.
- Momentum unloading: As the reaction wheels control the attitude of the satellites, they accumulate angular momentum, which has to be unloaded. Electric propulsion systems can be used to extract angular momentum from the spacecraft.
- Orbit raising: After spacecraft is launched into a LEO or GTO (Geostationary Transfer Orbit), it can be transfered to its mission orbit such as GEO with on board electric propulsion systems. Completing the transfer with electric propulsion saves fuel and reduces cost. Transfer maneuver requires a ΔV between 2500 and 4000 m/s.
- Deep space maneuvers: Deep space missions require high ΔV, which is suitable for electric propulsion systems. With electric propulsion, payload ratio of an spacecraft can be increased and travel durations can be decreased. Reaching escape velocity from Earth orbit requires between 3600 and 4000 m/s ΔV.
- Collision avoidance maneuvers: Satellites perform evasive maneuvers to avoid any possible collision with space junks or other satellites. These maneuvers usually require ΔV between 150 and 4600 m/s.

According to acceleration methods, electric propulsion systems can be separated into three categories: electrostatic, electromagnetic and electrothermal electric propulsion systems.

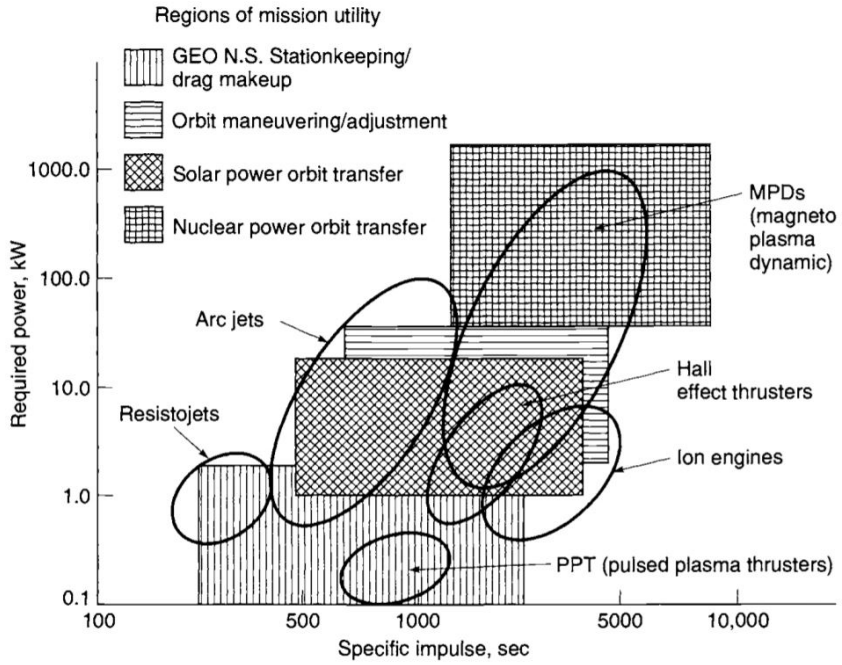

Figure 1.3. Applications of electric propulsion systems according to power consumption and specific impulse [2]

1.2.1. Electrothermal Systems

In electrothermal systems, propellant is heated with electrical energy and then accelerated through a converging-diverging nozzle. Electrothermal systems are similar to the chemical propulsion systems, therefore lighter propellants provide higher specific impulses. Most common electrothermal systems are resistojets and arcjets (Figure 1.4). Also, experimental systems such as inductive systems are developed.

1.2.1.1. Resistojets. In resistojets, propellant is heated with a resistive heater element. Heated propellant is then expelled through a nozzle. Resistojets can yield I_{sp} levels up to 300 s. Most resistojets use hydrazine (N_2H_4) as propellant. Adding a resistojet element to a hydrazine monopropellant system can increase the I_{sp} of the propulsion system by about 80 s [34].

1.2.1.2. Arcjets. In arcjets, propellant is heated with a plasma arc that is generated between a cathode and anode, that are placed inside the nozzle. Propellant can be heated to much higher temperatures than the wall material can endure, as the propellant is heated directly with an electric arc. Thus, specific impulses up to 700 s can be achievable with arcjets. As propellant, hydrazine and ammonia is used in most arcjet thrusters [3] .

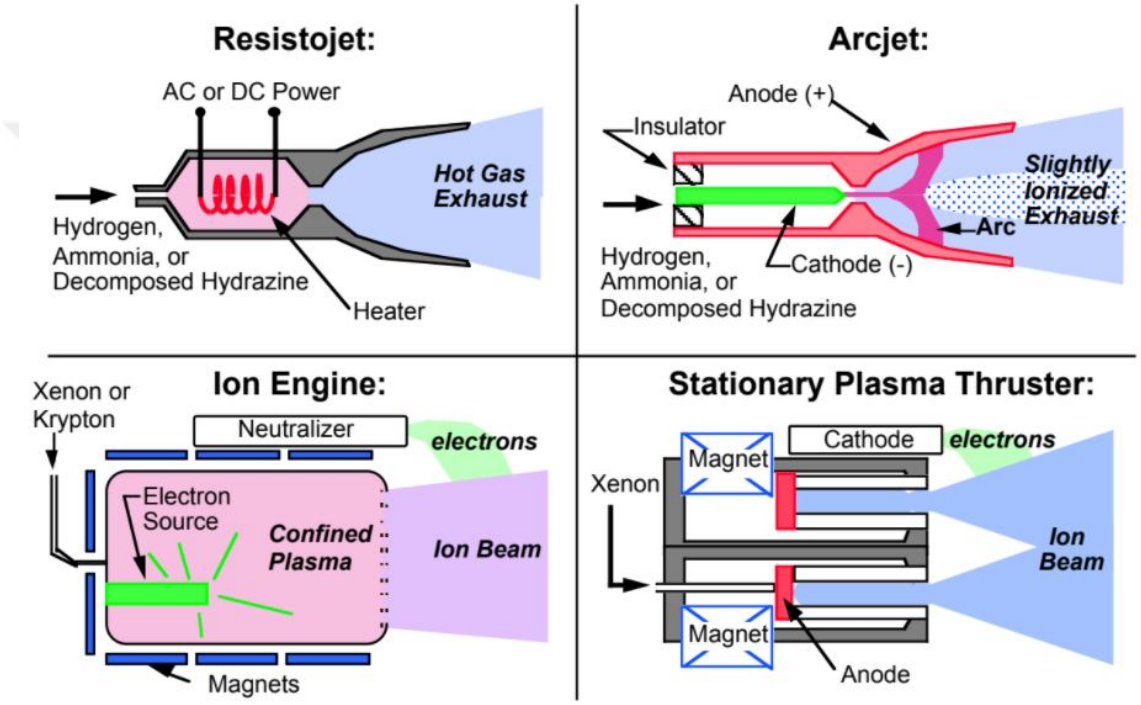

Figure 1.4. Commonly used electric propulsion systems [3]

1.2.1.3. Microwave Electrothermal Thrusters. The resistojets and arcjets have inherent limitations, such as the thermal limitations of the resistive element of resistojets and electrode erosion of arcjets. Therefore, alternative experimental methods are proposed such as microwave electrothermal thrusters (MET). In MET, propellant is heated with an inductively generated plasma. The thruster consists of a microwave resonance cavity, in which a standing wave is generated. Alternating electric field of the standing wave couples with the electrons of the gas in the cavity and generates a plasma near the nozzle exit. Propellant is injected into the cavity and as it swirls around the plasma, it is heated and then accelerated through a converging-diverging nozzle [37].

MET avoids the problems that other electrothermal systems have, as it heats the propellant with a floating plasma and it is electrodeless. A MET system is developed at BUSTLab by Mehmet Serhan Yildiz [38]. 3D drawing and operation of the thruster is shown in Figure 1.5.

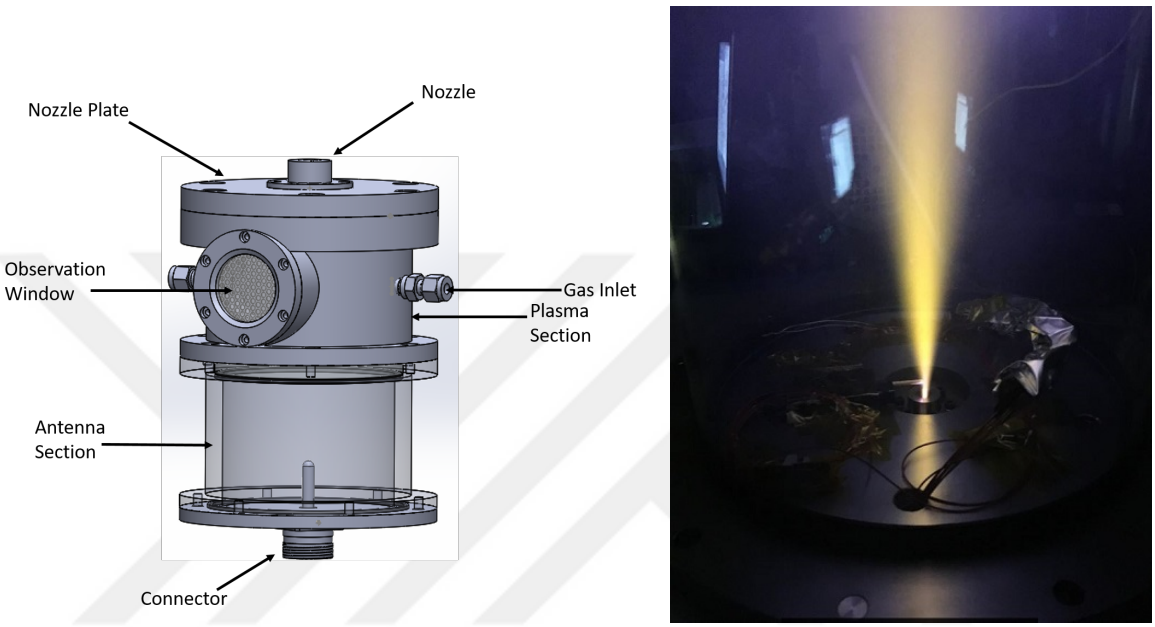

Figure 1.5. a) 3D drawing of MET, b) MET operation with nitrogen propellant

1.2.2. Electrostatic Propulsion Systems

In electrostatic propulsion systems, the propellant is ionized with various methods and then accelerated with Coulomb force:

$$F = qE \tag{1.7}$$

where, F is the force applied on the particle, q is the electric charge and E is the electric field. As the electrically charged particles can be accelerated to very high speeds with electric fields, very high I_{sp} values are achievable with electrostatic thrusters [39].

Since positively charged ions are more heavier than electrons, ions are accelerated in electrostatic thrusters. Therefore, the electrostatic thrusters require neutralisers to avoid charge accumulation on the spacecraft. Most commonly used neutralisers are hollow cathodes, which emit electrons via thermionic emission process. In electrostatic thrusters, heavier propellants are preferred to provide higher thrust. Most commonly used propellant is xenon, also other propellants such as krypton, bismuth and argon may be used. Electrostatic thrusters can be separated into two main categories: ion thrusters and Hall thrusters.

1.2.2.1. Ion Thrusters. Ion thrusters ionize the propellant inside a discharge chamber with different methods. Ions are extracted from the plasma inside the discharge chamber and accelerated to high speed with voltage applied to grids, therefore they are also called gridded ion thrusters. Grids are perforated plates with aligned holes. Generally two or three grids are used in ion thrusters. A high voltage is applied to screen grid, which is in contact with the plasma inside the discharge chamber. In order to avoid electron flux from the cathode to the discharge chamber, a negative voltage is applied to the accelerator grid, which is the outer grid. Potential difference between the grids generate an electric field, which accelerates ions to high speeds. I_{sp} values up to 10 000 s is achievable with ion thrusters. Ion thrusters do not confine and accelerate ions in a quasineutral plasma, therefore their thrust levels are limited with the saturation of charge density [6].

Ion thrusters use different ionization methods. In Kaufmann type ion thrusters, a hollow cathode is placed inside the discharge chamber, and propellant is ionized by electron bombardment. In RF (Radiofrequency) ion thrusters, an RF coil is wrapped around the discharge chamber as shown in Figure 1.6. The alternating current in the coil induces electric and magnetic fields in the discharge chamber and ionizes the propellant. In microwave ion thrusters, microwaves are used for ionization. Historically, Kaufmann type ion thrusters have been developed in USA, RF ion thrusters have been developed in Germany and microwave ion thrusters have been studied in Japan.

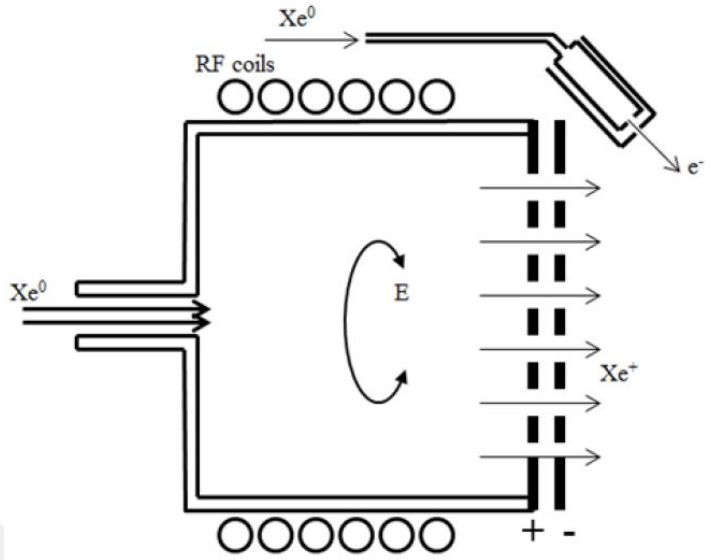

Figure 1.6. Schematic of an RF ion thruster [4]

1.2.2.2. Hall Thrusters. Hall thrusters utilize the cathode as both the neutraliser and the ionizer. Electrons that are emitted from the cathode is pulled to the anode, which is placed deep inside an annular discharge channel. Usually anode is utilized as the propellant injector to the discharge channel. Discharge channel walls are made of dielectric materials such as boron nitride (BN) in SPT (Stationary Plasma Thruster) type Hall thrusters, which are the most commonly used Hall thrusters. The electrons that flow towards the anode collide with the propellant atoms and ionize them. A radial magnetic field at the channel exit traps the electrons in a Hall current along the magnetic field lines. The radial magnetic lens topology at the channel exit is generated with a magnetic circuit that uses electromagnets or permanent magnets. Reduced electron motion along the axial direction generates an electric field at the channel exit. Ions are accelerated with the axial electric field. As the ions are accelerated in a quasineutral plasma, charge density is not a limitation for Hall thrusters, and they can provide higher specific thrust than ion thrusters. Hall thrusters can provide I_{sp} levels between 1000 and 3000 s [40].

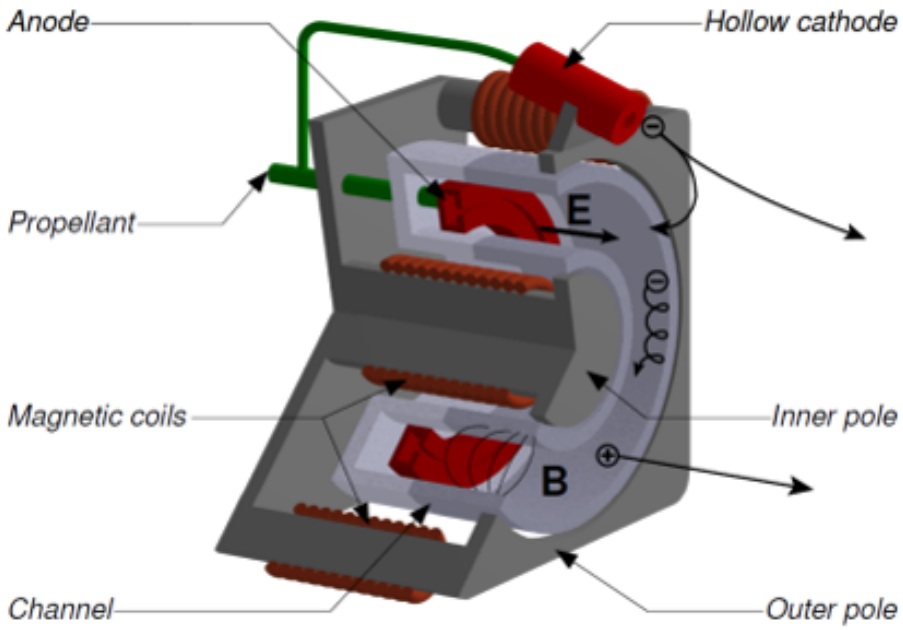

Figure 1.7. Schematic of a Hall thruster [5]

1.2.2.3. Electrospray and FEEP Thrusters. Electrospray and FEEP (Field Emission Electric Propulsion) thrusters extract ions from conductive liquid that are fed with small needles with high electric fields. They provide low thrust and are used generally at small satellites or for precision attitude control.

1.2.3. Electromagnetic Propulsion Systems

Electromagnetic thrusters accelerate ions with the Lorentz force:

$$\mathbf{F} = q\mathbf{v} \times \mathbf{B} \tag{1.8}$$

where, F is the acceleration force, q is the electric charge, v is the particle velocity and B is the magnetic field. Main electromagnetic systems are magnetoplasmadynamic (MPD) thrusters and pulsed plasma thrusters (PPT). In PPTs, a self induced magnetic field accelerates the propellant. The magnetic field is generated with the current that flows through the plasma which flows between electrodes. Pulsed high intensity electric currents are fed with capacitors. In PPTs, solid propellants such as Teflon can be used. The plasma discharge ablates the propellant surface and ionizes the vapour. PPTs can provide I_{sp} up to 1200 s. MPD thrusters ionizes and accelerates propellant through a nozzle with very high current plasma arc. MPD thrusters can provide high thrust densities at high power levels and can operate with different propellants. Also, they do not require neutralisers. Operational parameters of the propulsion systems are shown in Table 1.8.

Thruster	Specific Impulse (s)	Input Power (kW)	Efficiency Range (%)	Propellant
Cold gas	50–75	—	—	Various
Chemical (monopropellant)	150–225	—	—	N_2H_4 H_2O_2
Chemical (bipropellant)	300–450	—	—	Various
Resistojet	300	0.5–1	65–90	N_2H_4 monoprop
Arcjet	500–600	0.9–2.2	25–45	N_2H_4 monoprop
Ion thruster	2500–3600	0.4–4.3	40–80	Xenon
Hall thrusters	1500–2000	1.5–4.5	35–60	Xenon
PPTs	850–1200	<0.2	7–13	Teflon

Figure 1.8. Operational parameters of propulsion systems that are used in space [6]

1.3. History of Electric Propulsion

In the late 1800's and early 1900's the experiments with the cathode rays, such as the experiments conducted by J. J. Thomson and others showed that velocities that can be obtained by accelerating particles electrostatically can be much greater than any other known method, such as thermal expansion [41].

American scientist Robert H. Goddard (1882-1945) mentioned in his notebook in 1906 that a high reaction force may generated with very high velocity particles that are accelerated electrostatically [42]. In 1911, Tsiolkovsy published the first article that mentions electric propulsion. In 1913, Goddard patented a method for producing ions by confining the electrons with magnetic fields which resembles the discharge chambers of modern electric thrusters. Also, in 1917 Goddard patented the first electrostatic thruster prototype. In 1929, German scientist H. Oberth investigated the possible capabilities of electric propulsion in his book "Wege zur Raumschiffart" (Ways to Space Flight). He explained that electric propulsion systems requires less propellant than chemical propulsion systems. He also mentioned about the possible use of electric propulsion in attitude control of satellites. An extensive analysis of electric propulsion was conducted by Ernst Stuhlinger in his book "Ion Propulsion for Space Flight" in 1964 [36].

After 1960's several development projects were initiated in different countries. SERT-1 (Space Electric Rocket Test) was the first use of electric propulsion in space, which was launched in 1964. Kaufmann type ion thrusters are tested on SERT-1 probe. Also in 1964, PPT thrusters are used for attitude control of Russian Zond-2 satellite. In 1965, resistojets were used in Vela satellite of USA. In 1968, PPT's were used on US satellites of LES (Lincoln Experimental Satellite) and NOVA. In 1971, the first Hall thruster SPT-60, which is developed at Fakel Design Bureau in Russia, is used in Meteor satellite. Since then SPT Hall thrusters have dominated the electric propulsion market with more than 200 SPT Hall thrusters that are launched. SPT-100 is especially important as it is used on 72 satellites so far as shown in Figure 1.9. First commercial GEO satellites that use electric propulsion were Intelsat V satellites that were launched in 1981. They utilized resistojets for station keeping maneuvres. Later, arcjets were used in 1993 at Telstar 201 for station keeping at GEO, which showed that the utilization of electric propulsion reduces mass and therefore the costs of satellites. After that, electric propulsion systems began to be used more extensively for east-west and north-south station keeping maneuvres [7].

In 1995, a 13 cm Kaufman type ion thruster that is developed in Japan by MELCO (Mitsubishi Electric Corporation) was launched at Engineering Test Satellite 6 (ETS-6). In United States, XIPS (Xenon Ion Propulsion System) that is developed by Hughes/Boeing was launched in 1997 on PAS-5 satellite. Deep Space 1 was the first deep space mission with electric propulsion that is launched in 1998. On Deep Space 1, NSTAR (NASA Solar Electric Propulsion Technology Applications Readiness) ion thruster was used. Later in 1999, 25 cm XIPS ion thrusters are started to be used on 702 satellite platforms of Boeing for station keeping maneuvers. So far, XIPS-13 thruster has been used on 22 satelites, and XIPS-25 has been used on 31 satellites. In 2001, Artemis satellite of ESA was launched to GEO. However, because of a launcher malfunction, satellite completed its transfer to GEO with its RIT-10 ion thrusters that are developed by Astrium. RIT (Radiofrequency Ion Thruster) was first developed in University of Giessen in Germany and then developed at Astrium.

In 2003, Hayabusa 1 spacecraft was launched by JAXA for a sample return mission to an asteroid. μ10 ECR ion thruster, which utilizes microwaves are used on Hayabusa 1. In 2003, ESA launched SMART-1 spacecraft (Small Mission for Advanced Research in Technology) to lunar orbit. A single PPS-1350 Hall thruster that is developed by Snecma in France, was used on SMART-1. Travel from GTO to lunar orbit took 13 months, while the thruster used only 75 kg of xenon propellant and operated between 460-1200 W power levels. First American Hall thruster BHT-200 that is developed by Busek, was launched on TacSat-2 satellite in 2006. Electric propulsion systems proved their advantages further with the Dawn mission, which launched in 2007. With the 2.5 kW NSTAR ion thruster, Dawn spacecraft orbited Vesta and Ceres asteroids in 10 years.

With the developments in solar panels and thruster systems, electric propulsion systems have become an attractive solution for propulsion needs of GEO satellites. Utilization of Hall thrusters and ion thrusters increases as they provide higher I_{sp} levels than alternatives. The recent trend in GEO satellites is towards all electric satellites, which do not utilize any chemical propulsion systems.

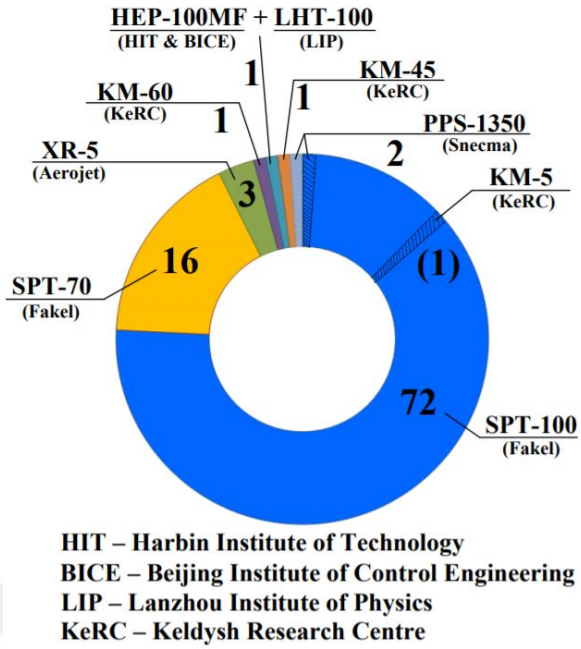

Figure 1.9. Distribution of GEO satellites according to the Hall thrusters [7]

In 2015, first all electric satellite of Boeing Eutelsat 115 West B was launched, which completed transfer from GTO to GEO with XIPS-25 thrusters [43]. It was also the first time two GEO communication satellites were stacked together in launch. In 2017, Eutelsat 172 B that was manufactured by Airbus was launched by Ariane 5 into GTO. It completed its transfer with Hall thrusters. Currently Airbus is producing six all electric satellites with E300 EOR satellite platform. Also, in Japan JAXA is planning to launch ETS 9 (Engineering Test Satellite) in 2021, to test their all electric bus systems. SPT-140 Hall thrusters are selected for the system. In US, XR-5 Hall thruster will be used for orbit raising missions at A2100 platform of Lockheed Martin and at GEOStar-3 platform of Orbital ATK. So far electric propulsion systems such as Hall thrusters, ion thrusters, and arcjets are used in 208 satellites. 46% of these satellites utilized Hall thrusters.

LEO satellites require different maneuvers than GEO systems, such as drag compensation. Power limitations in smaller LEO satellites have constrained the electric propulsion usage in LEO systems. Also, as the delta V requirements of LEO systems

are low, need to use electric propulsion is lower. So far 19 LEO satellites utilized electric propulsion systems such as PPTs, arcjets, Hall thrusters and ion engines. However, this situation may change in the future. Planned satellite constellation projects such as OneWeb and Starlink of SpaceX, which will provide internet access to the whole world, will use electric propulsion systems for orbital maneuvers. Electric propulsion may enable maneuvers that are not possible with chemical systems. Satellite servicing, repair and refuel missions may be possible. Also, with the development of air breathing electric propulsion systems, Very Low Earth Orbit missions may become possible.

So far seven deep space and lunar missions are performed with electric propulsion systems, and five of them utilized ion thrusters. Several deep space electric propulsion missions are planned to be launched. European BepiColombo mission to Mercury is launched in 2018. It utilizes gridded ion thrusters. DART (Double Asteroid Redirection Test) mission of NASA, forecasted to be launched in 2021, will utilize 7.5 kW NEXT-C gridded ion thruster. DART mission will be a demonstration of an asteroid redirection mission for planetary defence. The spacecraft will crash to near Earth asteroid Didymos.

1.4. Thrust Measurements

Although very high exhaust velocities and I_{sp} values can be generated with electric propulsion systems, achievable thrust levels are low due to limited external energy sources. Therefore, conventional thrust measurement systems that can be used with chemical rockets cannot be used with electric propulsion systems. Also, thrust to mass ratio of electric propulsion systems is very low, hence thrust measurement systems for electric thrusters have to be designed so that the thrust force of the thrusters can be differentiated from the weight of the thruster. In order to achieve this goal, pendulum based thrust stands developed [8]. In a pendulum mechanism, the thrust vector and the gravity vector can be separated, thus very low thrust values can be measured without being affected by the weight of the thruster. Several pendulum configurations are developed for thrust measurements of the electric propulsion systems. These are hanging pendulum, inverted pendulum, torsional pendulum and folded pendulum.

1.5. Thrust Stand Configurations

1.5.1. Hanging Pendulum Thrust Stand

In hanging pendulum configuration, the pendulum arm is attached through a top joint. Thruster is mounted on the bottom of the arm. Building and operating hanging pendulums are relatively easier than other configurations. The major advantage of the hanging pendulum configuration is stability. They are less influenced by external perturbations and test conditions that cause drift in the measurements. The major disadvantage of the hanging pendulum is that the sensitivity is influenced by the length of the pendulum arm, therefore sensitive thrust stands require large vacuum facilities. Also the response of the thrust stand is dependent on the mass of the thruster. However these factors can be dealt with careful calibration and proper equipments [8].

1.5.2. Inverted Pendulum Thrust Stand

In inverted pendulum configuration, a vertical pendulum arm is attached to a bottom pivot. The thruster is mounted on the top of the arm. Inverted pendulum configuration enables compactness and high sensitivity. The sensitivity strongly depends on flexure stiffness, which can be affected by external factors such as temperature and vibrations [11]. Also due to their compact size, they are vulnerable to heat that is absorbed from the thruster. Thermal shrouds and active cooling are often necessary to minimize the drifts at the measurements [8].

Using counterweights can reduce the sensitivity to the shifts in gravity vector, however using counterweights reduces compactness. Using parallel linkages to keep the thruster horizontal throughout the operation avoids rotation of the thrust vector, besides position of the thruster does not have a significant effect on the measurement accuracy. Also, with a parallel linkage structure, the point, where the calibration force is applied does not affect the calibration. However using parallel linkages increases complexity [12].

1.5.3. Torsional Pendulum Thrust Stand

The rotation axis of torsional thrust stands is parallel to the gravity vector (Figure 1.10), thus its response is independent of the thruster mass [18]. Torsional thrust stands have higher sensitivity and stability than inverted pendulum thrust stands. Since a long horizontal arm is needed for low thrust measurements, torsional thrust stands may cause problems in smaller vacuum facilities. Using counterweights decreases sensitivity to gravity effects, however increases the length of the pendulum arm [8].

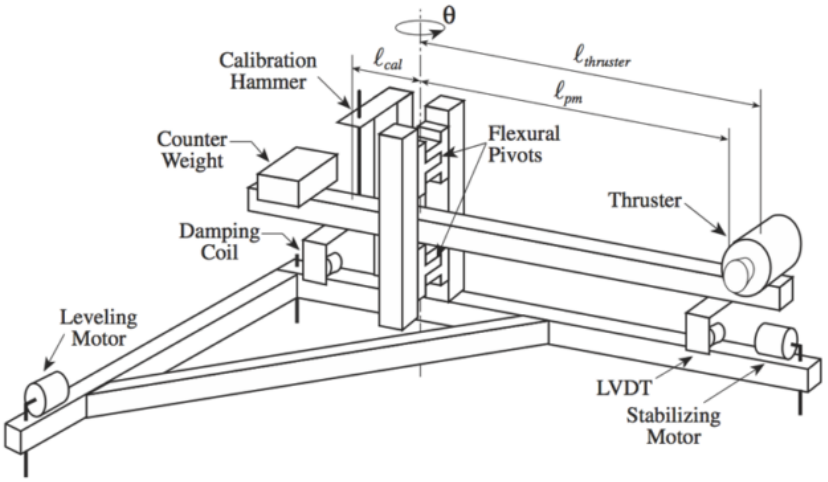

Figure 1.10. Torsional pendulum thrust stand concept [8]

1.5.4. Folded Pendulum Thrust Stand

Folded Pendulum concept was used for the purpose of ultra-low vibration isolation. Folded pendulums are used as seismometers and wave detectors because of their high sensitivity. Folded pendulums are combinations of hanging and inverted pendulums. Restoring force of the hanging side balances the unstable inverted pendulum side (Figure 1.11), thus a high sensitivity can be achieved [9].

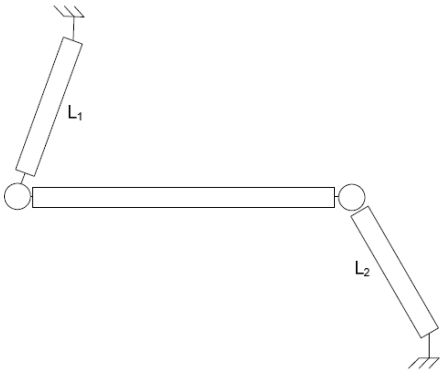

Figure 1.11. Kinematic diagram of the folded pendulum concept [9]

1.6. Thrust Stands in Literature

Thrust stands are one of the main test equipments of the electric propulsion system development processes. So far several thrust stands have been developed at different research facilities around the world. In this section a comprehensive review of these thrust stands is conducted.

1.6.1. ONERA Micro-Newton Thrust Stand

The ONERA (French Aerospace Research Agency) micro-Newton balance is a hanging pendulum with frictionless pivots (Figure 1.12). Thrust measurement range is from 0.01 mN to 1 mN. Two measurement modes are used. In open loop measurement, the pendulum is free to move, and in closed loop measurement a feedback loop utilizes a coil actuator to maintain the pendulum vertical. This mode reduces external perturbations that are caused by cables etc.

The ONERA thrust stand utilizes two accelerometers. One accelerometer measures the inclination of the pendulum, and the second accelerometer measures the vibrations of the support structure. Vibration signal is subtracted from displacement signal during thrust measurements. Pendulum displacement is measured with capacitive sensors.

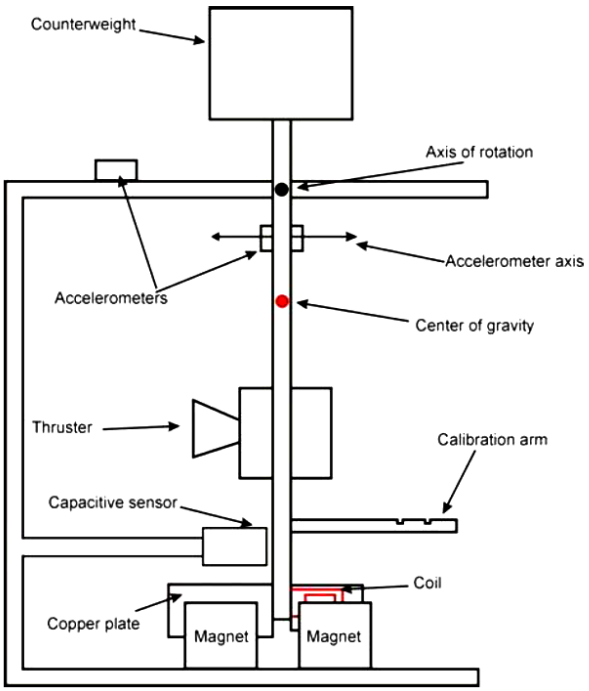

Figure 1.12. Configuration of the ONERA Micro-Newton Balance [10]

During calibration, small weights are placed on a horizontal arm attached to the pendulum. Placed weights generate a torque that represents the thrust. Calibration at low thrust levels is achieved using a voice coil. Thrust stand utilizes an Eddy current damping system, which consists of a copper plate that is attached to the pendulum, and permanent magnets. Also, a coil is used for active damping. Counterweights are used to balance the weight of the thruster. By changing the position of the counterweights, center of gravity of the pendulum can be changed, so that sensitivity and natural frequency of the thrust stand can be changed.

1.6.2. NASA Glenn Research Center High Power Trust Stand

The NASA Glenn thrust stand is an inverted pendulum thrust stand (Figure 1.13) [11]. Thrusters with masses up to 250 kg can be supported. Thrust measurement range is from 1 mN to 5 N. The uncertainty in the thrust measurements is ±0.6%. With an active control, inverted pendulum structure is kept at a stationary position

during the measurements, so that any change in the direction of thrust vector is avoided and measurement errors are minimized. As actuator a voice coil is utilized. Pendulum displacement is measured with a LVDT (Linear Variable Differential Transformer).

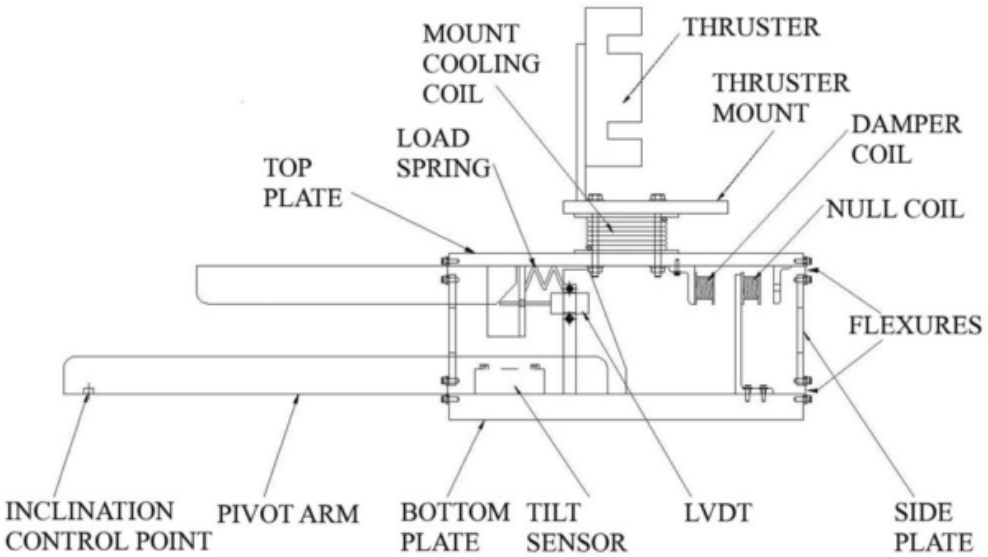

Figure 1.13. Schematic diagram of the inverted pendulum thrust stand of NASA Glenn [11]

Stiffness of the system is adjusted with a spring, thus the required restoring force can be adjusted according to the thruster mass and thrust level. Pendulum structure is assembled with eight thin stainless steel flexures, which provide one degree of freedom to the stand. Displacement of the pendulum is measured with a LVDT displacement sensor. Thrust stand is calibrated by applying small weights to simulate thrust, while a voice coil applies a counter force. Calibration line is calculated by comparing the applied current to the coil and applied weights.

Measurement accuracy may be affected from temperature changes. In order to keep the thrust stand at constant temperature, the thrust stand is actively cooled by a cooling system. Inclination of the thrust may also affect the measurement accuracy. Therefore, inclination of the thrust stand is adjusted with a leveling system. inclination is measured with a tilt sensor and adjustment are performed with a DC motor and a

piezoelectric stack.

The major error sources are moving pieces within the stand, such as flexures, spring, and power wires. The error is determined by using hysteresis and drift of the zero offset and calibration slope. Measured error is ±0.6% of measurement range. The power cables are mounted in a waterfall configuration (Figure 1.14). In this configuration any thermal expansion in the wires will lead to forces in the direction normal to the thrust vector, thus the measurements are not affected by temperature variations in cables. These lines provide also a damping effect.

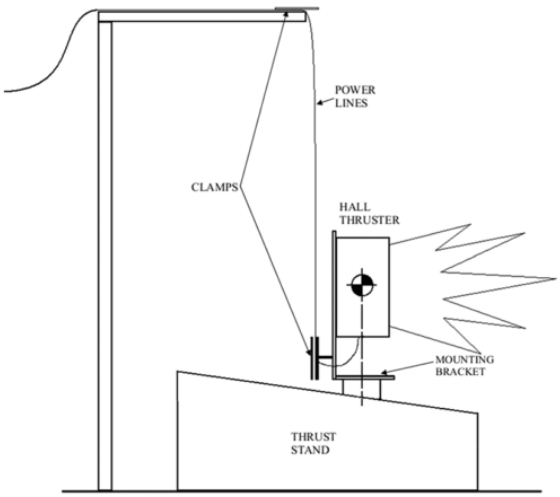

Figure 1.14. Waterfall configuration of power lines. [11]

1.6.3. DLR Electric Propulsion Test Facility Thrust Stand

The thrust stand that is developed by DLR (German Aerospace Center) is an inverted pendulum type, counter-balanced, electromagnetic force compensated thrust stand (Figure 1.15). Thrust measurement range is from 0.1 to 1000 mN. Thrust stand consists of a stiff parallelogram connected to the support structure by flexible joints. Thrust stand is shielded with metal plates, so that electromagnetic interferences between the propulsion system and electronic equipments of the thrust stand are avoided. Long term drift of the thrust stand is smaller than ±250 μN over 27 hours and thermal drift is smaller than 0.1 % per degree [13].

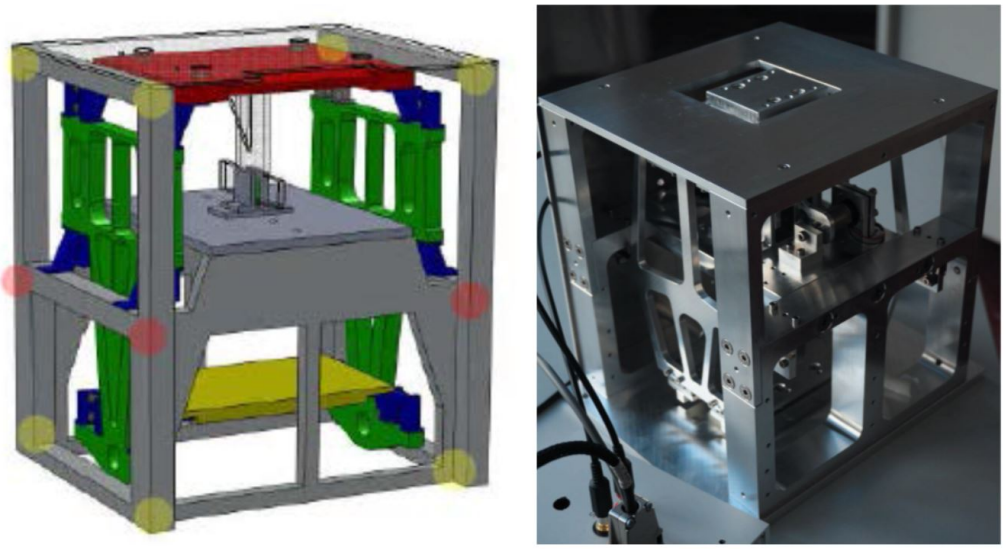

Figure 1.15. 3D model of the mechanical parts of the thrust stand (left) [12], thrust stand in its finished state (right) [13]

A capacitive displacement sensor is utilized for displacement measurement. An active control system with a voice coil actuator is used to compensate the thrust force in order to keep the pendulum at vertical position. The voice coil actuator is also used as a magnetic damper. To minimize hysteresis or other perturbations, cables and tubes are mounted in a "cable harp" holder configuration as shown in Figure 1.16. The cable lengths are adjusted so that the distance between the bending points of a cable or tube is the same as between the corresponding flexible bearings. Thrust stand is calibrated by applying known masses through a thin wire over a pulley. Calibration can be applied during the tests, so that the effects of thermal drifts can be observed.

1.6.4. Astrium Highly Precise Micro-Newton Thrust Stand

A micro-Newton thrust stand, developed by Astrium Satellites Friedrichshafen has a thrust range between 1 and 100 μN with a thrust resolution of 0.3 μN. Natural frequency of the pendulum is 0.77 Hz [14]. The structure consists of two symmetrical hanging pendulums: A reference pendulum and a measurement pendulum.

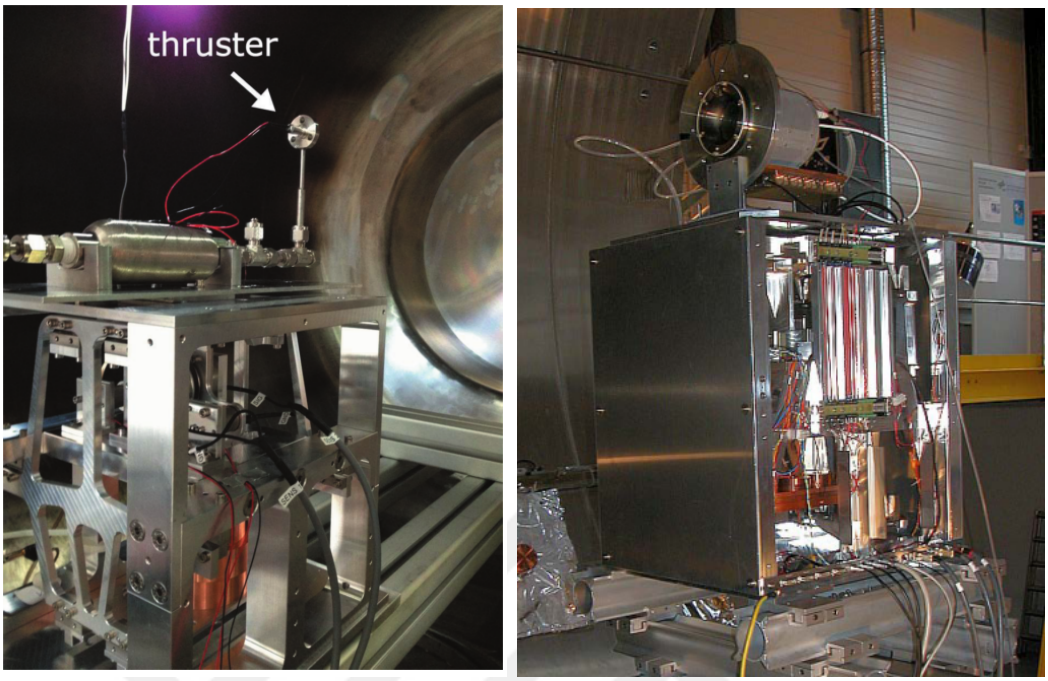

Figure 1.16. a) Cold gas test setup in DLR vacuum chamber [13], Ion engine mounted on the thrust stand in DLR vacuum chamber [12]

Thruster is hanged on the measurement pendulum and a dummy weight with the same physical properties with the thruster is hanged on the reference pendulum (Figure 1.17). The symmetrical setup is used to reduce the noise in the output signal. Each pendulum is connected to the support structure by four leaf springs. These leaf springs operate as frictionless pivots (Figure 1.18).

The thrust stand utilizes an Eddy current damping mechanism, which consists of permanent magnets that are mounted on support frame and aluminum plates that are attached to the pendulums. As displacement sensor, a laser interferometer is utilized. With the interferometer the displacement between two pendulum arm is measured. Thrust stand is calibrated with an electromagnetic actuator.

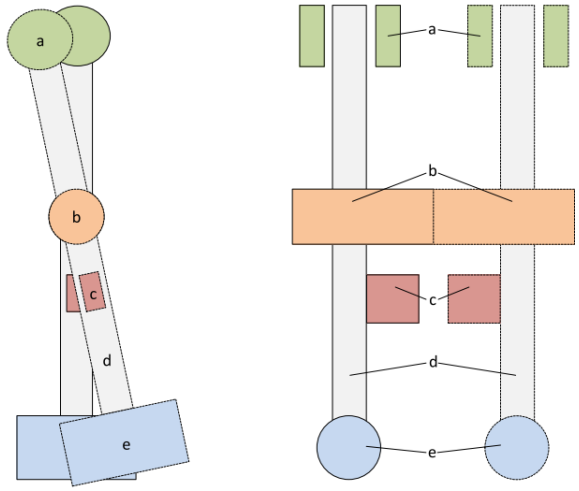

Figure 1.17. Parallel arms of the inverted pendulum thrust stand [14].

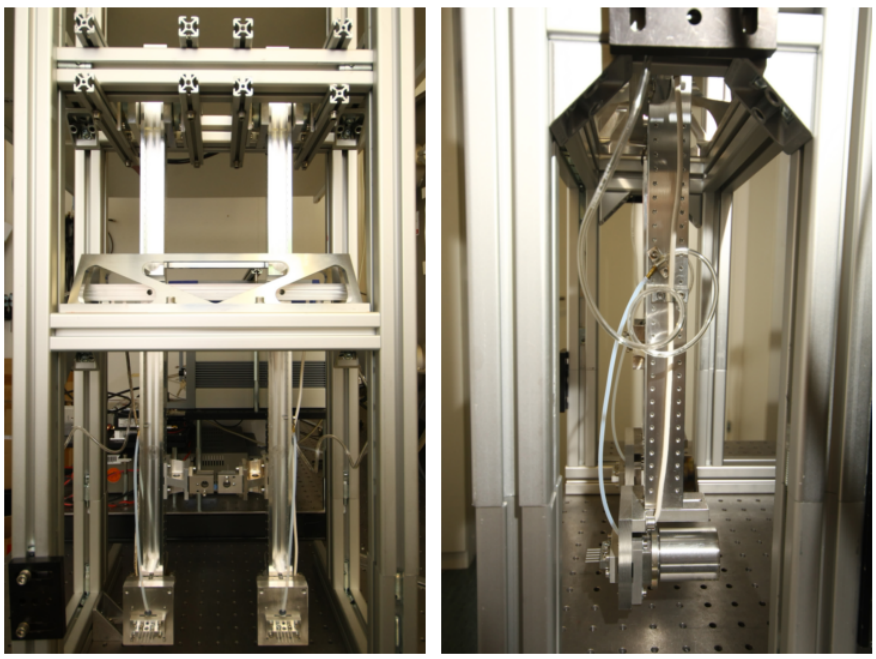

Figure 1.18. Pictures of the whole Astrium thrust stand assembly, outside of the vacuum chamber. [14]

1.6.5. ESA Micro-Newton Thrust Balance

In the ESA Propulsion Laboratory (EPL) a micro-Newton thrust stand is developed. Thrust stand has a thrust range from 1 to 500 μN with an uncertainty of $\pm$ 1μN. Thrust stand consists of two folded pendulum mechanisms (Figure 1.11): a reference assembly and a measurement assembly. The thruster is placed in the measurement assembly and a dummy weight is placed on the reference assembly. Inclination of the thrust stand is controlled with motorized micrometers (Figure 1.19). For each pendulum assembly a capacitive displacement sensor is used to measure the displacement of the pendulum. Voice coils are used as actuators to keep the pendulums at stationary position. As both pendulums are affected from same vibrations, a filtered measurement can be obtained by comparing the measurements of both pendulums.

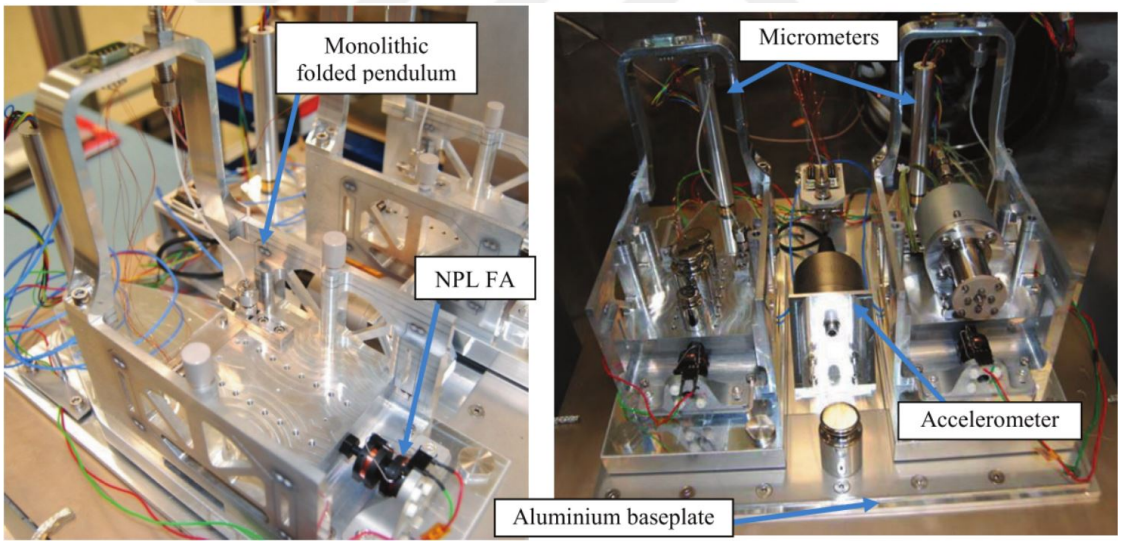

Figure 1.19. Micro-Newton Thrust Balance assembly installed on base plate [15]

1.6.6. Thales Alenia Space Italia Nanobalance Facility

The thrust stand, which is developed by Thales Alenia Space Italia has a thrust range up to 1 mN with a resolution of 0.5 μN [16]. It consists of two parallel inverted pendulum arms, which are made of copper-beryllium alloy. The pendulum arms are connected to a rigid block through flexible joints. The support plate is made of Zerodur.

Thruster is mounted on the measurement arm, while a dummy mass is mounted on the reference arm. The system is designed to have a natural frequency of 13 Hz. The displacement between the pendulum arms is measured with a laser interferometer. Also, a voice coil actuator is used for calibration.

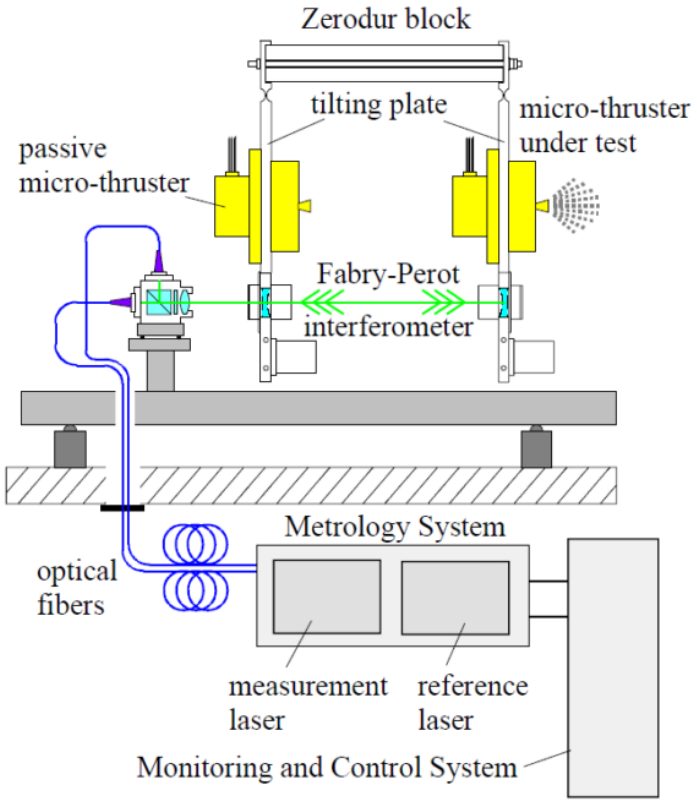

Figure 1.20. Block diagram of the nano-balance [16]

Inclination of the thrust stand is adjusted with a control system, which consists of three piezoelectric motors installed on the plate. A tilt sensor, which is placed on top of a Zerodur spacer, provides feedback. In order to reduce additional perturbations, a water cooling system is installed, so that the thruster temperature increase during the operation is avoided (Figure 1.21). The water cooling system includes a copper plate connected to the thruster.

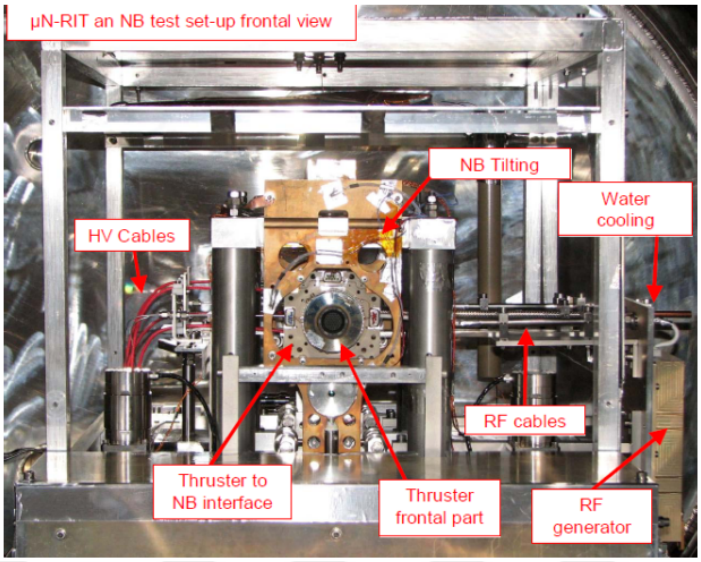

Figure 1.21. Nano-Balance test set up [16]

.

1.6.7. University of Southampton Thrust Balance

The thrust balance developed at the University of Southampton is a hanging pendulum thrust balance (Figure 1.22). Measured thrust levels are in the range of 0.05 to 0.4 mN. The thrust stand consists of a hanging pendulum made of stainless steel. The thruster is mounted on the bottom part of the pendulum. Thin stainless steel pivots are used, thus the pendulum arm has only one degree of freedom. The thruster carrier is thermally isolated from the rest of the pendulum via two Macor blocks to minimize heat conduction from the thruster. An interferometer is utilized as the displacement sensor. [17].

1.6.8. University of Southampton High Accuracy Impulsive Thrust Stand

An impulsive thrust stand is developed by the University of Southampton. The thrust stand can measure impulse bits of a typical Pulsed Plasma Thrusters for pico and nano-satellites in the range of 20-120 μN [19]. Torsional pendulum configuration is used (Figure 1.23).

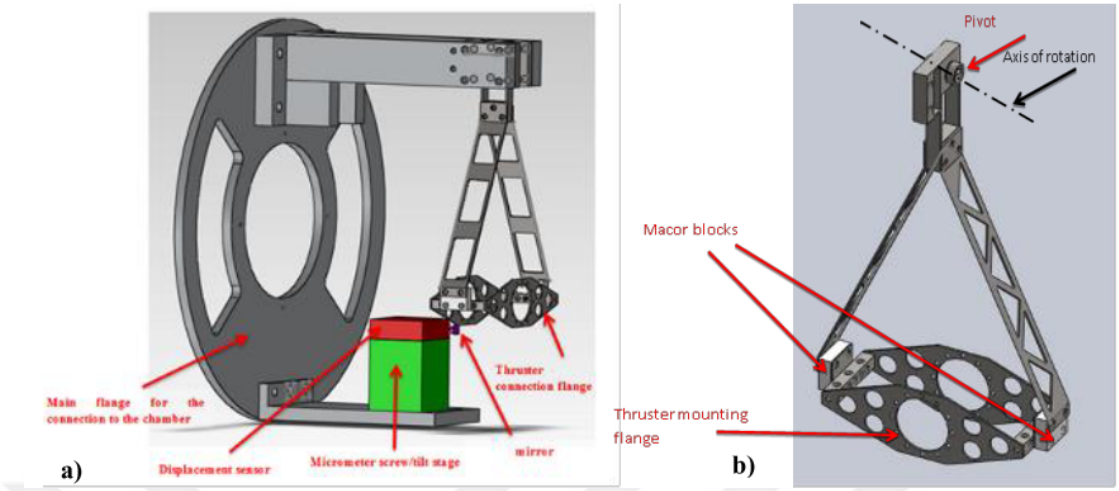

Figure 1.22. Complete thrust stand assembly schematic [17]

The thrust stand consists of a horizontal pendulum structure with the thruster mounted on one end and a counterweight on the other. The pendulum structure is symmetrical with respect to the pivot arm rotation axis, therefore gravity effects are eliminated. Pendulum is connected to the support structure through stainless steel flexural pivots, which constrain the arm so that the arm has only one degree of freedom. Pivots have very low friction and virtually no hysteresis. The displacement of the pendulum is measured with fibre optic linear displacement sensors.

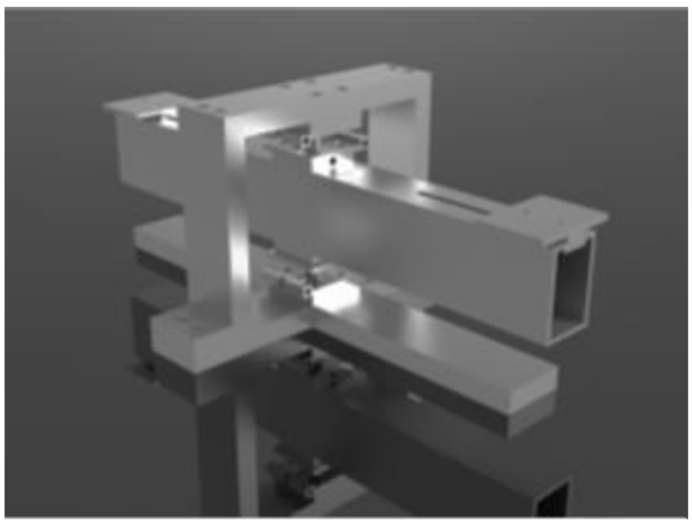

Figure 1.23. Design of the torsional thrust balance [18]

1.6.9. FOTEC μN Thrust Stand

A torsional μN thrust stand is developed by FOTEC (Forschungs- und Technologietransfer GmbH) and used at ESTEC (European Space Research and Technology Centre) to characterize FEEP and μPPT propulsion systems (Figures 1.24-1.25). Thrust stand measurement range is up to 6 mN with a total uncertainty of 7%.

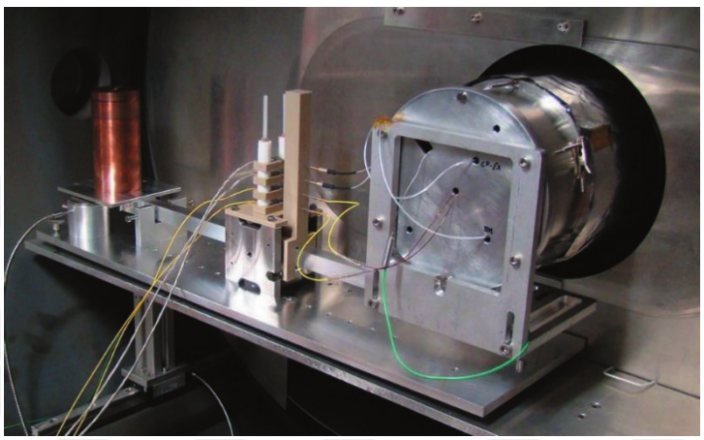

Figure 1.24. FOTEC μN Torsion thrust balance [19]

Calibration is performed with an electrostatic comb, which consists of several flat overlapped electrodes. When voltage is applied between these electrodes an attractive force is generated. Higher forces can be generated by using more electrodes. The distance between the electrodes needs to be small in order to generate a reasonable force. The thrust stand can be operated in free mode and null displacement mode. In free mode no actuator force is applied. In null displacement mode, the pendulum is kept at stationary position with the actuator. In null displacement mode any external influence can be neglected.

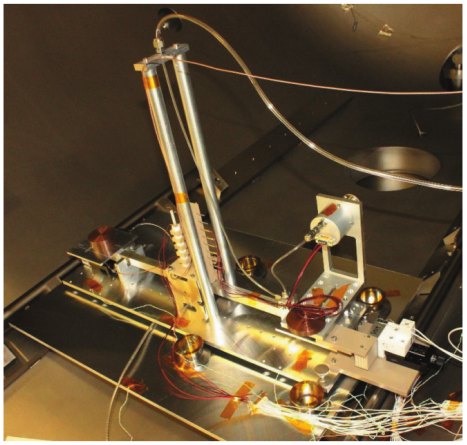

Figure 1.25. Test setup of FOTEC thrust balance at ESTEC [19]

1.6.10. ARC Seibersdorf Research GmbH Thrust Stand

A torsional pendulum thrust stand is developed at ARC-SR, in order to measure the thrust of In-FEEP (Indium Field Emission Electric Propulsion) thruster [20]. The thrust stand consists of a horizontal pendulum arm, which is a hollow rectangular aluminium profile (Figure 1.26). Pendulum arm is attached to the support structure with flexural pivots.

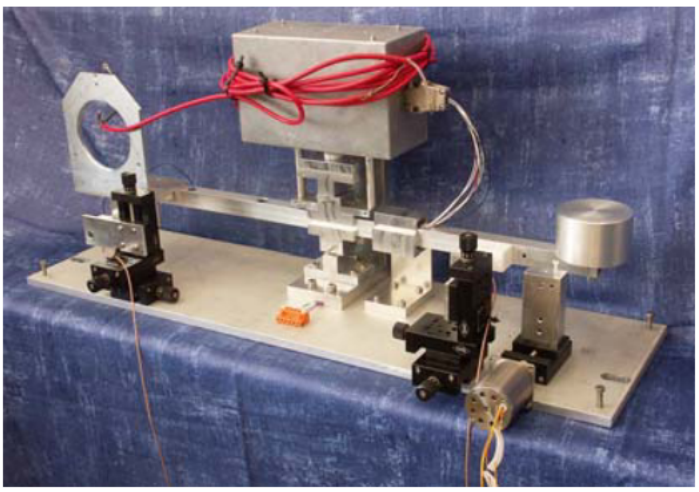

Figure 1.26. ARC-SR μN thrust balance [20]

An infrared displacement sensor is utilized for displacement measurements of the pendulum arm. The infrared sensor provides a near side and a far side measurement. Near side measurements provide higher sensitivity, while the far side measurements provide a wider range. The sensor is mounted on a linear stage, and can be positioned according to the drifts in the position of the pendulum arm. Electrostatic comb actuators are used for calibration.

1.6.11. University of Tokyo Thrust Stand for Low Impulse Measurement

The thrust stand that is developed at the University of Tokyo utilizes a torsional pendulum configuration [21]. Thrust is mounted on one side of the pendulum arm, while the pendulum is balanced with a counterweight (Figure 1.27). Pendulum arm is supported with flexural pivots. The thrust has a natural frequency of 0.2-0.25 Hz. An LVDT sensor is used as the displacement sensor. An impact pendulum is used for calibration. The impact force of the impact pendulum is measured with a load cell. Thus, pulsed microthrusters can be tested on the thrust stand. As damper, an Eddy current magnetic damper is utilized.

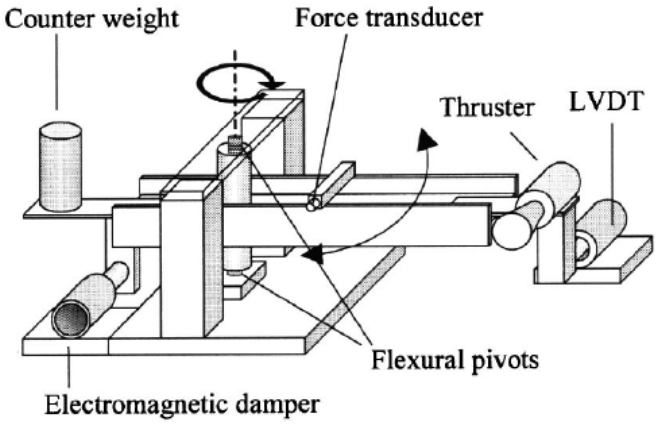

Figure 1.27. Schematic diagram of the thrust stand. [21]

.

1.7. Contribution of this Work

In this thesis, the development process of BUSTLab thrust stand is presented. Thrust stand design, components and operational procedure are introduced in detail. The thrust stand is designed to measure thrust at mili-Newton levels. Measurement range of the thrust stand can be adjusted between a large span according to the thrust level of the thruster. Thrust measurement range of the thrust stand can be changed from 6 mili-Newtons to 300 mili-Newtons. Thrust stand can be calibrated in high vacuum environment inside the vacuum chamber. Displacement measurements are performed with an LVDT displacement sensor, which measures the deflection of the pendulum motion and benefit from the vibration isolation characteristics of the pendulum. With the developed thrust stand, thrust measurements of the electric thrusters that are developed at BUSTLab such as MET and HK40 Hall thruster are conducted. From the thrust measurements, operational characteristics of these thrusters are calculated. It was shown that the theoretical calculations in the previous studies are valid.

Also, in this research a new Hall thruster, which is called UK90 Hall thruster, with higher discharge power than the previous one is developed. An internal cathode is utilized, so that an efficiency increase is obtained. A novel Hall thruster design is developed, so that the internal cathode is utilized at such lower power level than the conventional Hall thrusters with internal cathode configurations. An extensive magnetic analysis and design optimization is performed during the thruster design phase. Effects of the design parameters on the operational characteristics are investigated. Recent design improvements at Hall thruster development at research centers such as MIT and JPL are investigated. Using these studies, a near magnetic shielding is aimed during the magnetic circuit design. Magnetic field strength at the channel exit is measured with a Gaussmeter. Also, thermal analysis of the Hall thruster is conducted. During the thermal analysis process, heat flux from the plasma in the discharge channel to the channel walls and anode is calculated. By using the thermal analysis, a novel passive cooling design is developed to protect the magnetic parts from high temperature.

Besides Hall thruster development, numerical analyses are performed for the hollow cathode that is used with the Hall thruster. Thermal characteristics of the hollow cathode is investigated with these numerical analyses. According to these thermal analyses, heater design is optimized for better thermal insulation. Also, electrical potential distribution within the cathode is investigated. During the research, dozens of hollow cathode tests are performed and more than a dozen new hollow cathodes are produced with several design iterations.

BURFIT-80 ion thruster is tested and according to these tests several design improvements are made. With these improvements, a new RF ion thruster is designed, built and tested, and the previously encountered problems such as arcing problems with electrical connections of the grids are solved. In this study, the detailed design of the BURFIT-80 ion thruster is presented. The ion thruster utilizes an alumina discharge channel. Plasma is generated with a copper RF antenna that is wrapped around the discharge channel. Two grids are used to accelerate ions to high exhaust velocities. The electrical connections and insulation design are presented in this study.

In Chapter 2, development process of the thrust stand is presented. Several design criteria and thrust stand characteristics are discussed. Then, numerical and analytical analysis of the thrust stand is conducted. Components and subsystems are investigated. Calibration procedure is explained. In Chapter 3, development process of the Hall thruster is investigated. It was shown that the internal cathode configuration increases the efficiency. Design parameters are optimized by using the scaling laws and the thrusters in the literature. Magnetic topology of the thruster is analyzed and magnetic shielding concept is investigated. Also, numerical analysis for hollow cathode is performed.

In Chapter 4, experiments and results are discussed. HK40 Hall thruster and MET are tested and operational characteristics and investigated. In Chapter 5, the conclusion of the research and future work are discussed.

2. DEVELOPMENT OF THRUST STAND

2.1. Design Constraints and Requirements

Electric propulsion systems that will be tested are designed to operate at high vacuum environment, therefore tests will be conducted inside BUSTLab vacuum chamber, which is 1.5 m in diameter and 2.7 m in length [44]. The thrust stand is designed to be operated in this vacuum chamber. As the thrust measurements are affected from facility effects, these effects should be minimized with a proper thrust stand design. Chamber walls may have an effect on the thruster because of the interference with the plasma ejected from the thruster, therefore during measurements the thruster should be positioned far from the chamber walls and near to the middle of the vacuum chamber. Dimensions of the thrust stand are chosen according to the dimensions of the vacuum chamber. Thrusters will be operated in high vacuum with a pressure level around 5×10^{-5} torr. In order to keep high vacuum and clean environment in the vacuum chamber, vacuum safe components are used in the thrust stand, thus outgassing is prevented. Also, any gas traps in the thrust stand should be avoided with vent holes.

The thrusters, which will be used in the measurements, produce thrusts in a varied range. Hall thrusters and ion thrusters produce thrusts up to 80 mN, however microwave electrothermal thruster produces thrust force up to 300 mN. Therefore, measurement range of the thrust stand should cover all of this range. Also optimum measurement range should be adjustable according to the thruster that will be tested. Sensitivity of the thrust stand is aimed to be at micro-Newton levels. Thrust stand should support the weight of the thruster. Any failure may damage the thrust stand as well as thrusters. As the measured forces are very low, external effects have a significant impact in the measurement. These effects are the vibrations caused by the cyropumps and the thermal effects. Vibrations should be filtered to obtain a clean measurement. During the operation, electronic parts of the thrust stand and the thruster will generate heat. This heat may cause errors in measurement and has to be controlled.

Also, the thrust stand should be protected from the plasma in the vacuum chamber. RF ion thruster and microwave electrothermal thruster may emit electromagnetic waves and may interfere with the sensor signals, therefore the thrust stand and signal cables should be insulated to avoid interference.

2.2. Thrust Stand Characteristics

Thrust stand has inherent characteristics, which affect its operation. These characteristics such as natural frequency, stiffness and settling time are optimized during the design process and also measured during calibration process before each measurement sequence.

2.2.1. Natural Frequency

As the thrust stand is based on a pendulum configuration, it has a natural frequency. The natural frequency depends on the total stiffness and the moment of inertia of the pendulum structure. Moment of inertia of the pendulum structure depends on the pendulum arm length, cross section, mass and the positions of the thruster and counterweight. Also cables and propellant lines affect the natural frequency. Natural frequency of the thrust stand can be calculated from the peak of the Fourier transform of the acquired displacement signal as shown in Figure 2.1 [18].

Since the natural frequency is measured from the displacement signal, effects of all the possible sources of influence are taken into account. Natural frequency measurement can be applied during the calibration process before the thrust measurements. The error in the natural frequency measurement depends on the signal sampling frequency and the number of acquired samples, thus with a relatively high sampling frequency the error can be reduced to negligible levels.

Natural frequency of the thrust stand determines the transmissibility of the system, which is defined as the ratio of the amplitude of the vibrations of the pendulum assembly to the amplitude of the vibrations of the vacuum chamber.

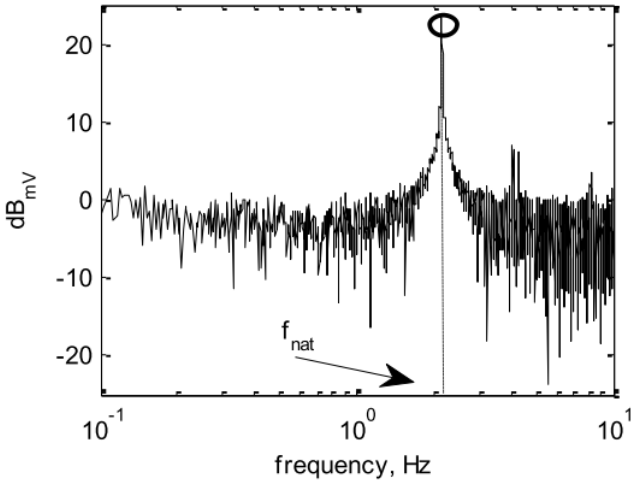

Figure 2.1. Example of Fourier Transform used to evaluate the natural frequency [18]

The vibrations at the vacuum chamber at higher frequencies are not transmitted to the pendulum assembly which has a lower natural frequency. Therefore, designing the thrust stand with a low natural frequency is crucial for thrust measurements. Also the value of the natural frequency is important for resonance protection.

2.2.2. Stiffness

Stiffness of the thrust stand is determined by the bending stiffness values of the flexural strips. Also cables and pipes increase the stiffness of the system. Because of the pipes and cables and also thermal effects, stiffness may change at different tests. Therefore, calibration is a necessity before each test. The stiffness of the thrust stand can be calculated by comparing the applied force and the measured deflection. Force actuators are used in order to apply a known force on the pendulum during the calibration. The value of stiffness is important as it determines the sensitivity and the measurement range. At high stiffness values, the deflection is smaller, therefore the measurement range increases. However, noise becomes more significant and measurement resolution decreases. At lower stiffness values, the deflection increases. Significance of noise decreases, however deflections may be too large for measurements [11]. Determination of the stiffness of the strips is crucial for the thrust stand design.

2.2.3. Settling Time

As the tests are conducted in high vacuum environment and movement of the pendulum is achieved with the flexural strips, thrust stand operates virtually without any friction forces. Frictionless nature of the thrust stand may lead to undamped oscillations, therefore a damping force is essential to the system. According to the applied damping force, the system may be under-damped, over-damped or critically damped, which cause a lag in the measurements due to the oscillations. In order to obtain a desired settling time, the damping force should be adjusted. Settling time is defined as the time between the instant that the force is applied to the system and the instant that the amplitude of the pendulum oscillations drop under a certain value around the steady state. Settling time of the thrust stand is measured and adjusted during the calibration process.

2.3. Thrust Stand Design

Considering the weights of the thruster systems and the size of the vacuum chamber, inverted pendulum configuration is chosen for the BUSTLab thrust stand. Inverted pendulum configuration decreases the effects of the external perturbations such as the vibrations in the vacuum chamber, due to the inherent low natural frequency characteristic of the inverted pendulum configuration [11]. Also, inverted pendulum configuration provides a compact structure, which is suitable to the vacuum chamber dimensions. In the thrust stand design, a double armed pendulum is used, thus the change in the thrust vector during the operation is avoided [45]. Two parallel plates are used as pendulum arms, rather than four separate arms, thus instabilities in the structure is further avoided (Figure 2.2). Vertical pendulum arms support two horizontal platforms. Thruster is placed on the upper platform, and counterweights are placed on the bottom platform. Counterweights balance the weight of the thruster, so that the effect of the thruster weight on the measurements is avoided. Also, position of the thruster on the upper platform and thruster dimensions have no effect on measurements in this configuration.

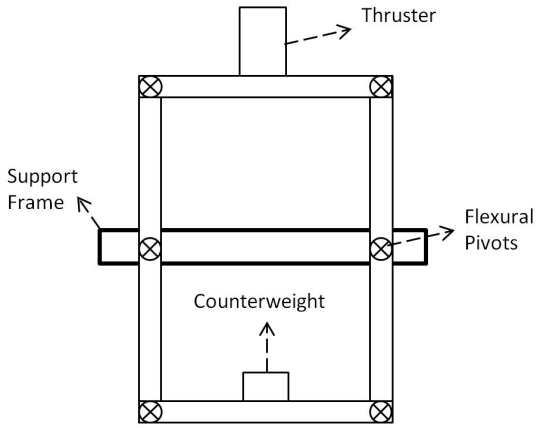

Figure 2.2. Counterbalanced Inverted Double Pendulum Concept

In the thrust stand design 12 joints are used at total. Joint selection and design is crucial for thrust stand operation. As the joints should not outgas in high vacuum environment, joints should not have oil as lubricant. In order to increase the sensitivity, friction in the joints should be small as well. In initial design iterations torsional pivot bearings are utilized as the joint elements. These pivots are shown in Figure 2.3. These pivots have highly accurate stiffness values and provide one degree-of-freedom movement to the pendulum mechanism, and enables frictionless movement. However, they require precise manufacturing of the pendulum structure. Any misalignment may prevent assembly and damage the pivots. Therefore, an alternative joint design that requires less precision is used. In this design, pendulum components are attached with thin stainless steel strips. These flexural strips provide frictionless movement at single axis and do not outgas. Also, dimensions of the strips can be changed, thus stiffness, natural frequency and load capacity of the thrust stand can be adjusted to the desired level [46, 47].

The 3D drawings of the thrust stand are made using Siemens NX. A 3D CAD drawing of the thrust stand is shown in Figure 2.4. In the drawing the pendulum structure and the outer frame is shown. The HK40 Hall thruster is placed on top of the upper plate.



Figure 2.3. Torsional Pivot Bearings

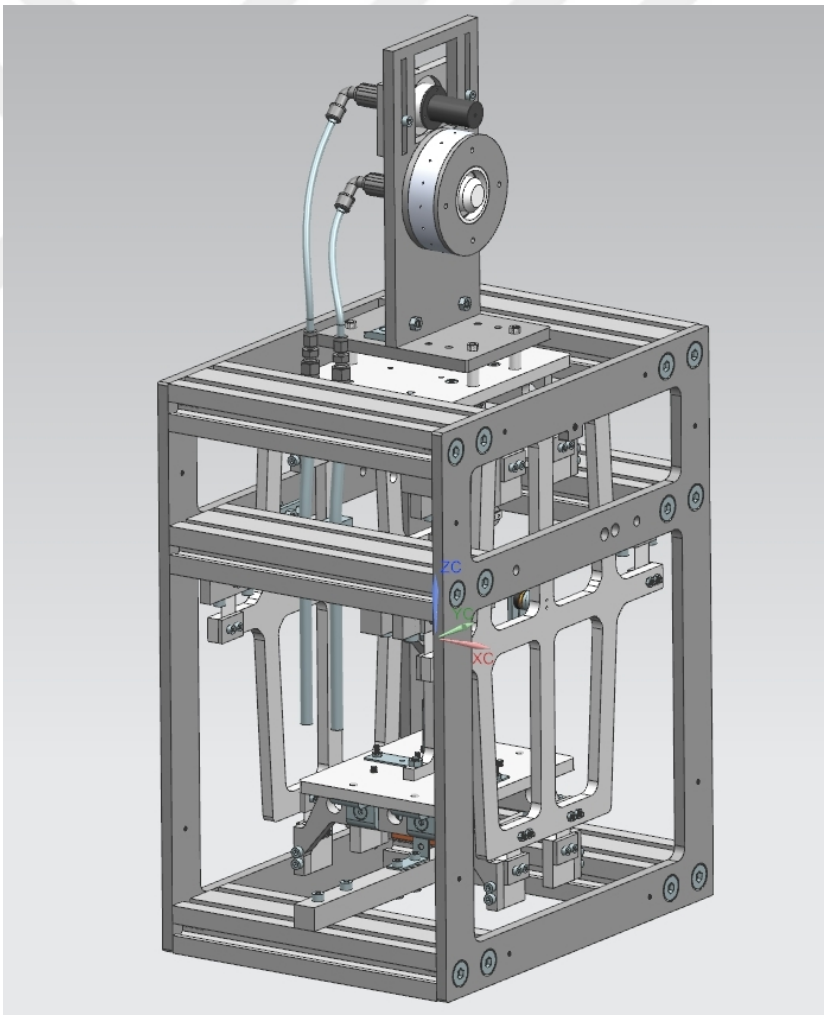

Figure 2.4. 3D drawing of Thrust Stand with HK40 Hall Thruster

2.4. Modelling and Analysis of Thrust Stand

Thrust stand design includes many design variables, such as pendulum arm length and flexural stiffness. These variables should be optimized for high sensitivity at the desired measurement range. In order to optimize the thrust stand components, each component of the thrust stand is analysed. As will be shown in the following sections, flexural stiffness, which is the bending stiffness of the thin strips, is the primary design variable that determines the measurement range and sensitivity. Therefore flexural stiffness of the thin strips is analysed analytically and then numerically. Strength of these strips is also an important parameter. Therefore strength analyses are conducted. Another important design parameter is the pendulum arm length. In order to determine proper size, a comprehensive analysis for thrust stand response is conducted. According to these analyses, appropriate sensors and actuators are determined. Design parameters are then optimized for these equipments.

2.4.1. General Model of Thrust Stand

Modelling process has begun with the generation of a dynamic model of the thrust stand. In this model, all parts of the thrust stand and also facility effects are investigated. Free body diagrams of the components of the pendulum structure are generated. These parts consist of two horizontal plates and two vertical side pendulum arms. Horizontal plates consist of the upper plate, which carries the thruster, and the bottom plate, which carries the counterweight. Two side plates connect the horizontal plates and are connected to an outer carrier frame by flexural joints. The plates are assumed to be rigid bodies, as their stiffness is much higher than flexural pivots. In order to represent the vibrations in the vacuum tank, base excitations in horizontal and vertical directions are added to the model. At the end of the modelling, similar solutions are found with previous works on this topic [45], however in this work much more detailed analyses are conducted. During the analysis it was seen that the position of the thruster does not affect the measurement.

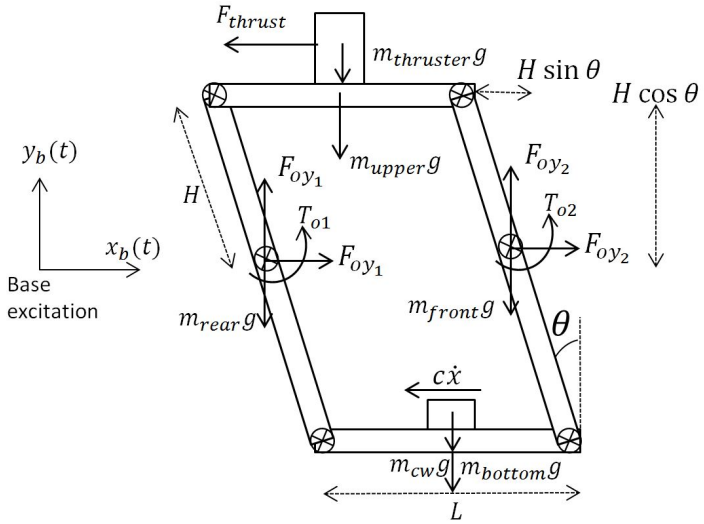

Figure 2.5. Free Body Diagram of Thrust Stand

In Figure 2.5, F_{thrust} is the thrust generated by the thruster, F_{oy}, F_{ox} and T_o are respectively the horizontal and vertical forces and moment applied by the flexural pivots, which connects the pendulum to the support frame. Weights of all plates are included in the analysis. H is the half length of the side plates and L is the length of the horizontal plates. θ is deflection angle. c is damping constant. Base excitation is applied to the pivots, which connects the pendulum to the support frame. Base excitation is modelled as:

$$x_b(t) = A_x sin(w_b t) \tag{2.1}$$

$$y_b(t) = A_y sin(w_b t) \tag{2.2}$$

where, A is the amplitude and w_b is the frequency of the vibration. In the following diagrams, each part is modelled separately.

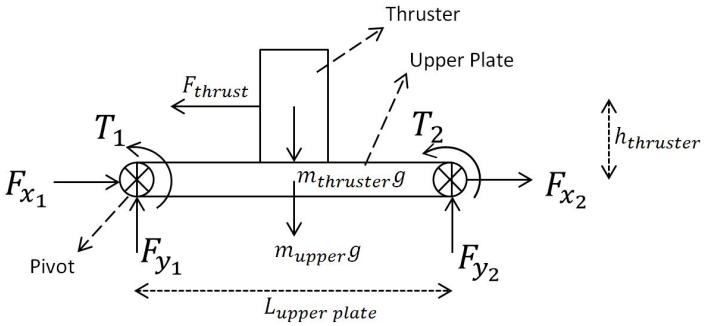

Figure 2.6. Free Body Diagram of Upper Plate

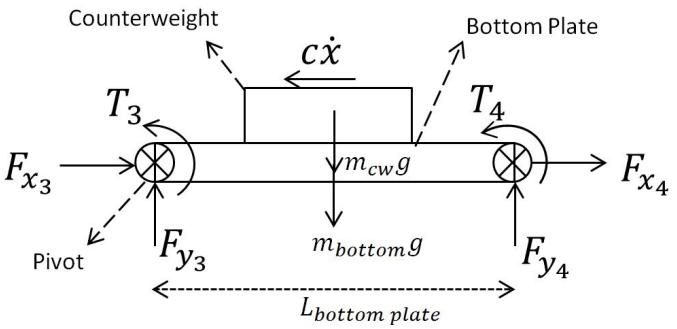

Figure 2.7. Free Body Diagram of Bottom Plate

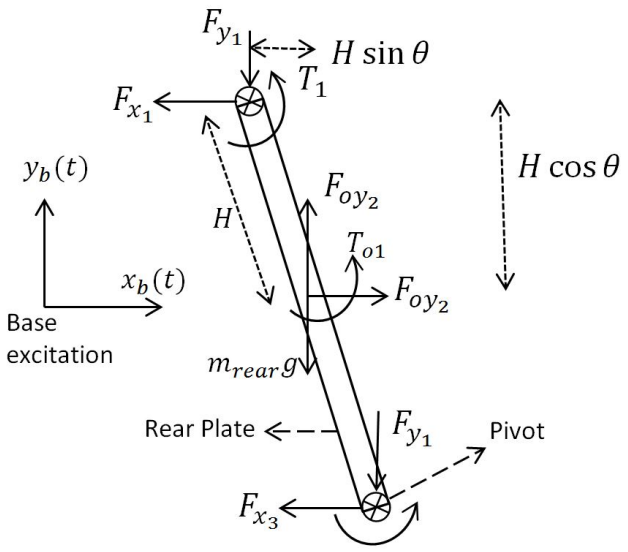

Figure 2.8. Free Body Diagram of Rear Plate (Front Plate is also similar)

In Figures 2.6-2.8, F_x, F_y and T are the forces in x- and y-axis and moments between the plates respectively. $h_{thruster}$ is the distance between the thrust vector and center of gravity of the upper plate. From these diagrams 15 equations are obtained; 5 in x-axis, 5 in y-axis and 5 moment equations. In order to find the dynamic response of the thrust stand, these equations are solved. In order to have all support forces and excitations, total moment equation is generated with respect to the middle point of bottom plate:

$$\begin{aligned} F_{thruster}\,[2Hcos(\theta) + h_{thruster}] + (m_{rear} - m_{front})\frac{gL}{2} + M_{dif}gHsin(\theta) \\ -(F_{oy1} - F_{oy2})L - 2(F_{ox1} + F_{ox2})Hcos(\theta) = J_T\ddot{\theta} + 4k\theta \end{aligned} \tag{2.3}$$

where, k is the bending stiffness of the flexural strips, J_T is the moment of inertia of the thrust stand with respect to the reference point. M_{dif} is the mass difference between the upper and lower parts of the thrust stand:

$$M_{dif} = m_{thruster} + m_{upper} - m_{cw} - m_{bottom} \tag{2.4}$$

Linear acceleration of the upper and bottom plates are evaluated as:

$$\ddot{x}_{upper} = \ddot{x}_b - H\ddot{\theta}cos(\theta) + H\dot{\theta}^2sin(\theta) \tag{2.5}$$

$$\ddot{y}_{upper} = \ddot{y}_b - H\ddot{\theta}sin(\theta) - H\dot{\theta}^2cos(\theta) \tag{2.6}$$

$$\ddot{x}_{bottom} = \ddot{x}_b + H\ddot{\theta}cos(\theta) - H\dot{\theta}^2sin(\theta) \tag{2.7}$$

$$\ddot{y}_{bottom} = \ddot{y}_b + H\ddot{\theta}sin(\theta) + H\dot{\theta}^2cos(\theta) \tag{2.8}$$

Horizontal and vertical support forces at the joints are further calculated from the equations obtained from the free body diagrams and the equations 2.5, 2.6, 2.7 and 2.8.

$$F_{oy1} - F_{oy2} = \frac{m_{rear} - m_{front}}{2}(g + \ddot{y_b}) + \frac{Fh}{L} - \frac{\ddot{\theta}}{L}(J_{upper} + J_{bottom}) + \frac{8k\theta}{L} \tag{2.9}$$

$$F_{ox1} + F_{ox2} = \frac{F}{2} + \frac{\ddot{x_b} M_{total}}{2} - \frac{m_{dif}}{2}\left[H\ddot{\theta}cos(\theta) + H(\dot{\theta}^2 sin(\theta)\right] + \frac{cH\dot{\theta}cos(\theta)}{2} \tag{2.10}$$

where, J_{upper} and J_{bottom} are moments of inertia of the upper and bottom plates, respectively. M_{total} is total mass of the pendulum structure:

$$M_{total} = m_{thruster} + m_{upper} + m_{cw} + m_{bottom} + m_{front} + m_{rear} \tag{2.11}$$

Equations 2.9 and 2.10 are then substituted into equation 2.3:

$$\begin{aligned} &F_{thruster} H cos(\theta) - (m_{rear} - m_{front})\frac{\ddot{y_b} L}{2} \\ &+M_{dif}\Big(gHsin(\theta) + H^2 cos(\theta)\left[\ddot{\theta}cos(\theta) + \dot{\theta}^2 sin(\theta)\right]\Big) \\ &-M_{total}\ddot{x_b} H cos(\theta) = 12k\theta + \ddot{\theta}(J_T - J_{upper} - J_{bottom}) + \dot{\theta}cH^2\left(cos(\theta)\right)^2 \end{aligned} \tag{2.12}$$

From equation 2.12, steady state value of the system can be obtained by eliminating all time depending terms:

$$F_{thruster}Hcos(\theta) + m_{dif}gHsin(\theta) = 12k\theta \tag{2.13}$$

If equation 2.13 is solved steady state response of the thrust stand is obtained:

$$\theta = \frac{F_{thruster}H}{12k - M_{dif}gH} \tag{2.14}$$

In order to obtain the transient response of the thrust stand, equation 2.12 is further developed, by adding base excitation equations. The acceleration terms ($\ddot{x_b}$ and $\ddot{y_b}$) in the equation 2.12 can be obtained by differentiating equations 2.1 and 2.2:

$$\ddot{x}_b(t) = -A_x w_b^2 sin(w_b t) \tag{2.15}$$

$$\ddot{y}_b(t) = -A_y w_b^2 sin(w_b t) \tag{2.16}$$

By substituting equations 2.15 and 2.16 into equation 2.12 the transient response of the thrust stand is obtained:

$$\ddot{\theta}(t) = \Bigg\{ F_{thruster} H cos(\theta) + M_{dif} \left[gHsin(\theta) + H^2 \dot{\theta}^2 cos(\theta) sin(\theta) \right] + \frac{L(m_{rear} - m_{front})}{2} A_y w_b^2 sin(w_b t) + M_{total} H cos(\theta) A_x w_b^2 sin(w_b t) - 12k\theta - \dot{\theta} c H^2 \left(cos(\theta)\right)^2 \Bigg\} \frac{1}{J + M_{dif} H^2 \left(cos(\theta)\right)^2} \tag{2.17}$$

where,

$$J = J_T - J_{upper} - J_{bottom} \tag{2.18}$$

2.4.2. Numerical Solution of the Thrust Stand Response

Equation 2.17 is solved numerically using MATLAB. The differential equation solver function that is used is ode45, which utilizes explicit Runge-Kutta method. The solution is then interpolated with a certain sampling frequency, which resembles the sampling frequency of the sensor that will be used in the thrust stand. Obtained solution has two arrays of data; angular displacement and velocity of the pendulum. Linear displacement at the position of the displacement sensor is calculated from the angular displacement of the pendulum (Figure 2.9). In order to increase sensitivity, the displacement sensor is positioned next to the bottom plate, where the linear displacement is highest. However in further designs the displacement sensor is positioned between the upper and bottom plates rather than between the bottom plate and outer frame. The linear displacement at the position of the sensor is proportional with the output of the sensor.

$$measured_displacement = Hsin(\theta) \tag{2.19}$$

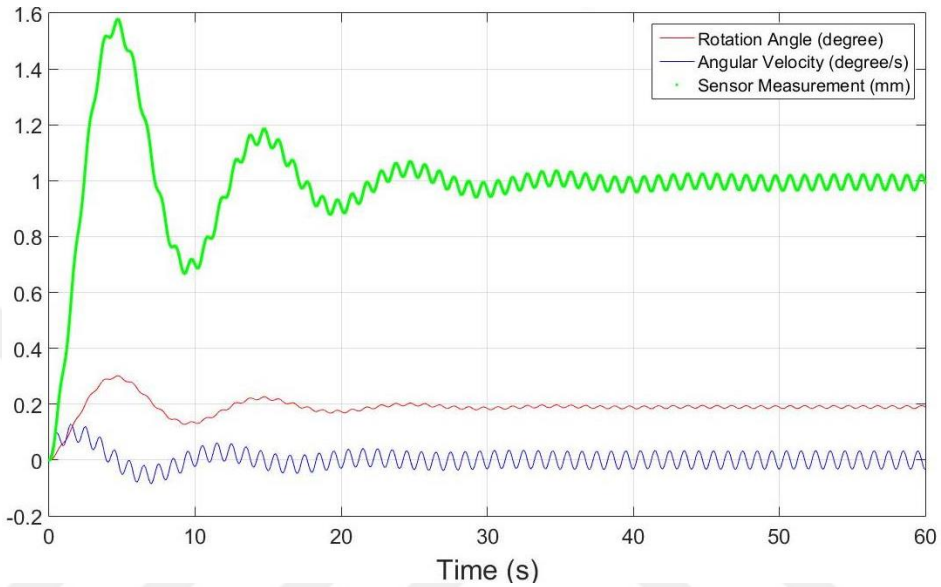

Figure 2.9. Thrust Balance Response with 10 mN Thrust and Base Excitation with Frequency of 1 Hz

The vibrations in the output signal is analyzed by applying Fast Fourier Transform, thus natural frequency of the thrust stand and amplitudes of vibrations at each frequency are obtained. In the analysis, amplitude and frequency of base excitation is given as input, therefore transmissibility properties of the thrust balance can be calculated for each frequency. Transmissibility is the ratio of amplitudes of the vibrations in the measurement to the base excitation. Also phase difference between the response of the thrust stand and base excitation is calculated. At the end, settling time and steady state measurement of the thrust stand is calculated. Settling time is determined as the time required for the measurement output to reach and stay within 2% of the steady state value.

With the data acquired from the numerical simulations, the thrust stand is optimized for desired measurement range and sensitivity. Optimization is applied by simulating the response of the thrust stand for different design variables.

First design variable is the height of the thrust stand. According to equation 2.14, output measurement is proportional to the height of the thrust balance, therefore the thrust stand is designed to be as large as it is possible within the limits. These limits are due to the interference of the thruster plume with the vacuum chamber walls, so that the thruster can be positioned at the middle of the vacuum chamber.

Second design variable is the bending stiffness of the flexural joints. The response of the thrust stand is simulated for different stiffness values (Figure 2.10). The response of the thrust balance is inversely proportional to the joint stiffness, as found in equation 2.14. Also thrust stand response curves with respect to thrust for different stiffness values are calculated (Figure 2.11). The output measurement is linearly proportional to the thrust.

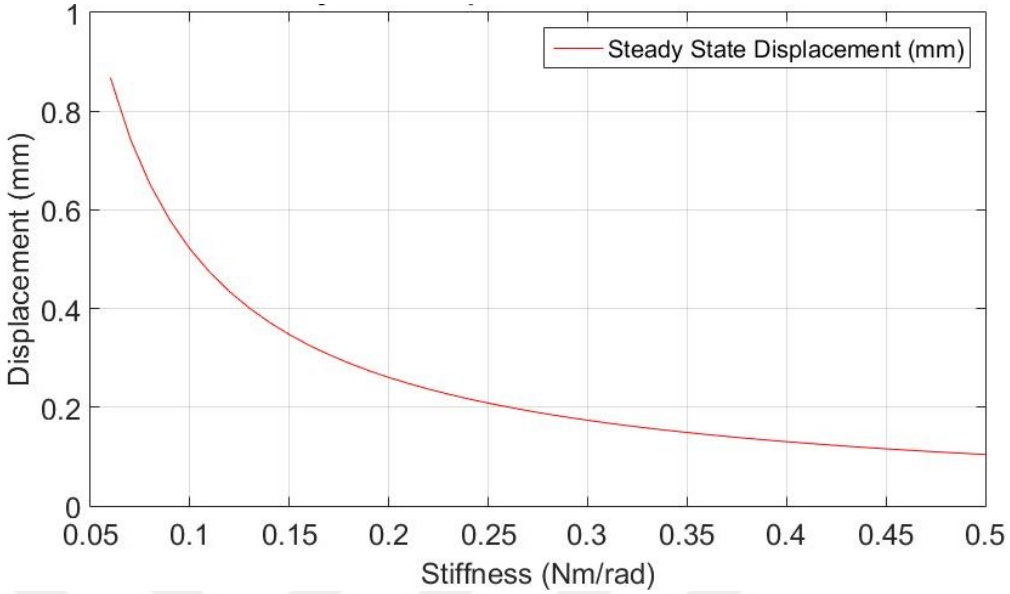

Figure 2.10. Thrust Stand Response vs. Stiffness at 10 mN Thrust

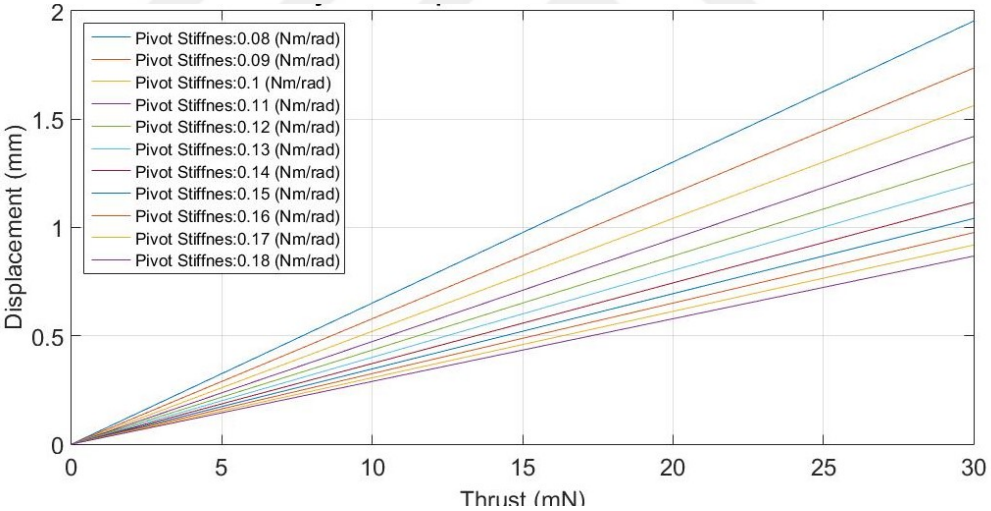

Figure 2.11. Thrust Stand Response vs. Thrust and Stiffness

As can be seen in equation 2.14, thrust stand response also depends on the mass asymmetries in the thrust stand. During tests, the counterweight may not be perfectly adjusted and the center of gravity may not be along the pivots, therefore the measurements will be effected. Effect of the mass asymmetry is simulated in Figure 2.12. In this figure mass difference is defined as the difference between the mass of the upper part and the mass of the lower part of the inverted pendulum, as it is in equation 2.4. If the upper part of the pendulum is heavier than the lower part, angular displacement increases. Above a certain mass difference, the thrust balance loses its balance and the system is broken. Also this limit is dependent on the stiffness of the pivots. Increasing the mass of the counterweight, stabilizes the system, however it reduces sensitivity. Measurement and sensitivity of the thrust stand can be adjusted by changing the counterweights.

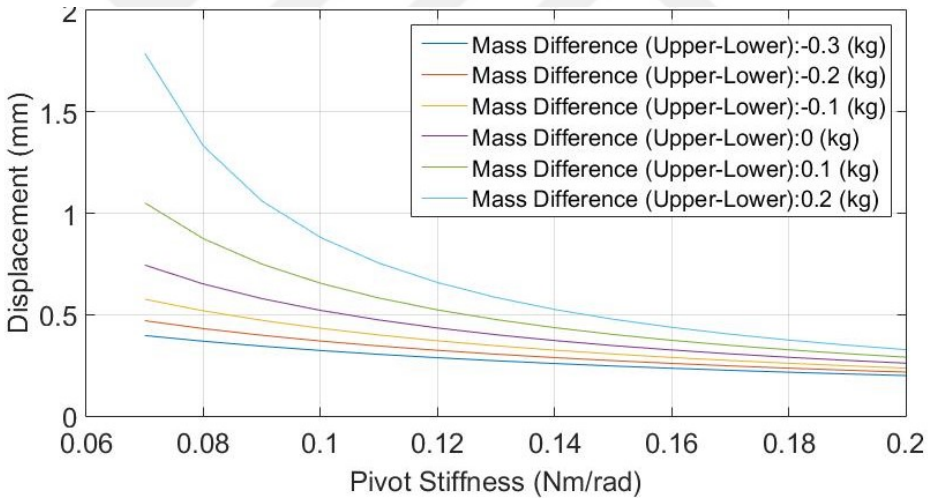

Figure 2.12. Thrust Stand Response vs. Mass Difference and Stiffness

As the flexural pivots are highly frictionless, the system has to be damped. An eddy current damping system is utilized. In this section, eddy current damping system is modeled and its effect is simulated. Eddy current damping force is modelled as:

$$F_{eddy} = -c_{eddy}\dot{x} \tag{2.20}$$

where, c_{eddy} is damping constant and $\dot{x}$ is the velocity of the bottom plate.

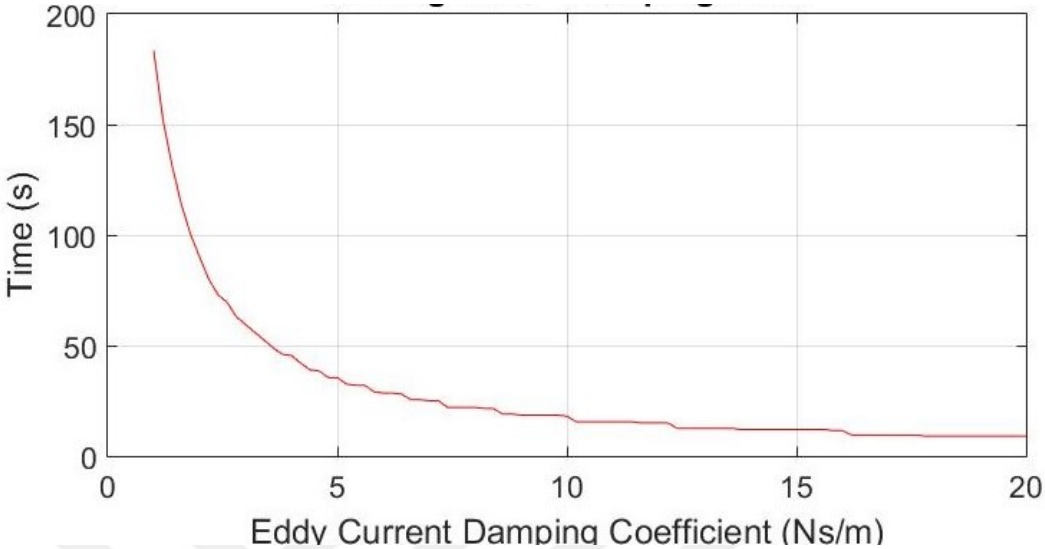

Figure 2.13. Settling Time vs. Damping Constant

As the damper is positioned on the bottom plate, equation 2.20 becomes:

$$F_{eddy} = -c_{eddy} H \dot{\theta} cos(\theta) \tag{2.21}$$

Damping constant determines the settling time and overshoot value of the transient response. Increasing damping constant decreases settling time (Figure 2.13) and enables faster measurements, also it reduces overshoot ratio, therefore high values of damping constant prevent dangerous deflections outside the measurement range (Figure 2.14). Overshoot rate is the rate of the maximum deflection to the steady state deflection.

Natural frequency of the thrust stand is important for vibration reduction. Possible resonances with the vacuum tank reduce sensitivity and may cause damage in the thrust stand. Natural frequency of the thrust stand is influenced by the stiffness value of the joints and mass asymmetries in the system. It was found that natural frequency of the system is very low and vibrations in the vacuum tank will not cause resonance, especially cryopumps, which operate at 1 Hz. Also a lighter counterweight reduces the

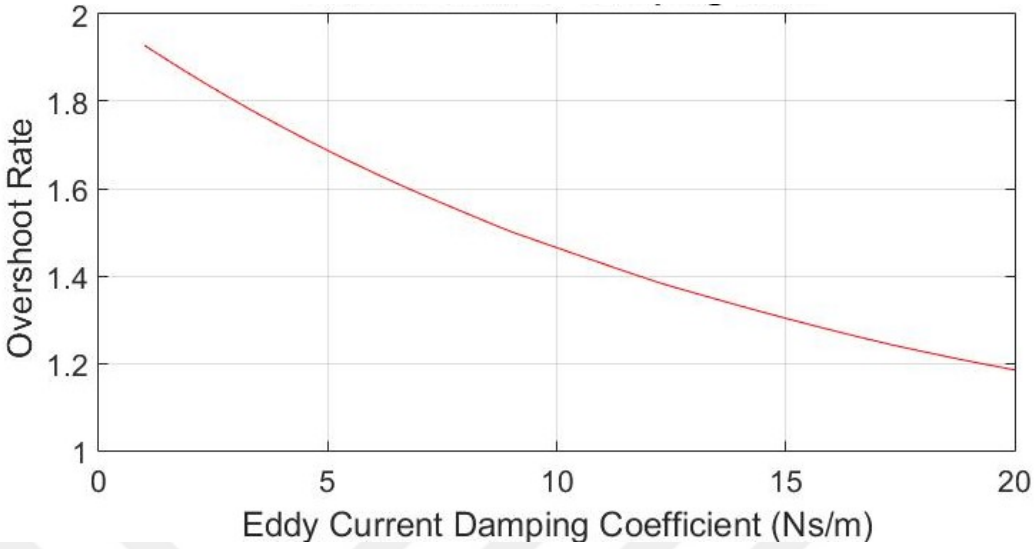

Figure 2.14. Overshoot Rate vs. Damping Constant

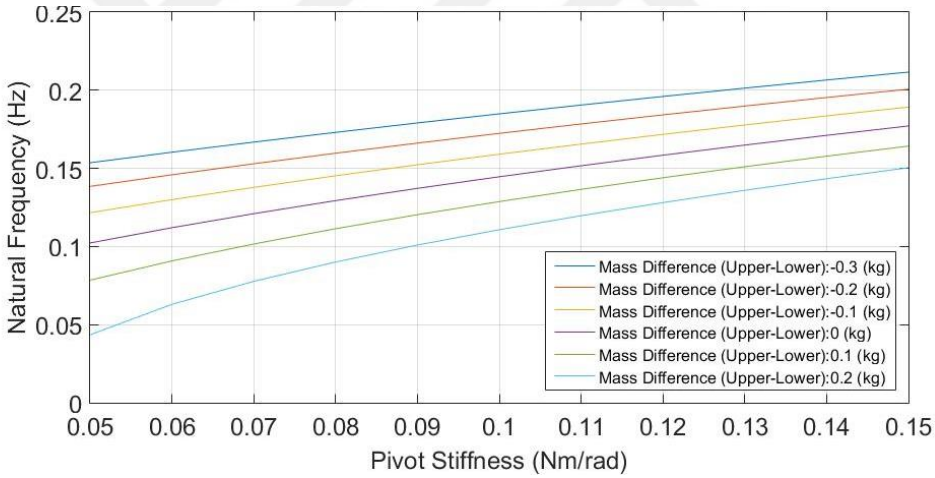

Figure 2.15. Natural Frequency of the Thrust Stand vs. Pivot Stiffness

natural frequency, therefore it may reduce vibrations in the system (Figure 2.15).

Transmissibility characteristic of the thrust stand is simulated. Transmissibility of the thrust stand is defined as the ratio of the amplitudes of base excitation and vibrations in the pendulum. Transmissibility is affected from the damping constant and mass asymmetries. In Figure 2.16, transmissibility for different frequencies are measured. As expected transmissibility reaches its peak at natural frequency of the pendulum. However dominant vibrations in the vacuum tank expected to have much

higher frequencies, therefore these vibrations will be damped by the system. Also phase difference for these vibrations will be nearly 180°, because of higher frequencies than natural frequency. Higher damping constants prevent resonance around natural frequency.

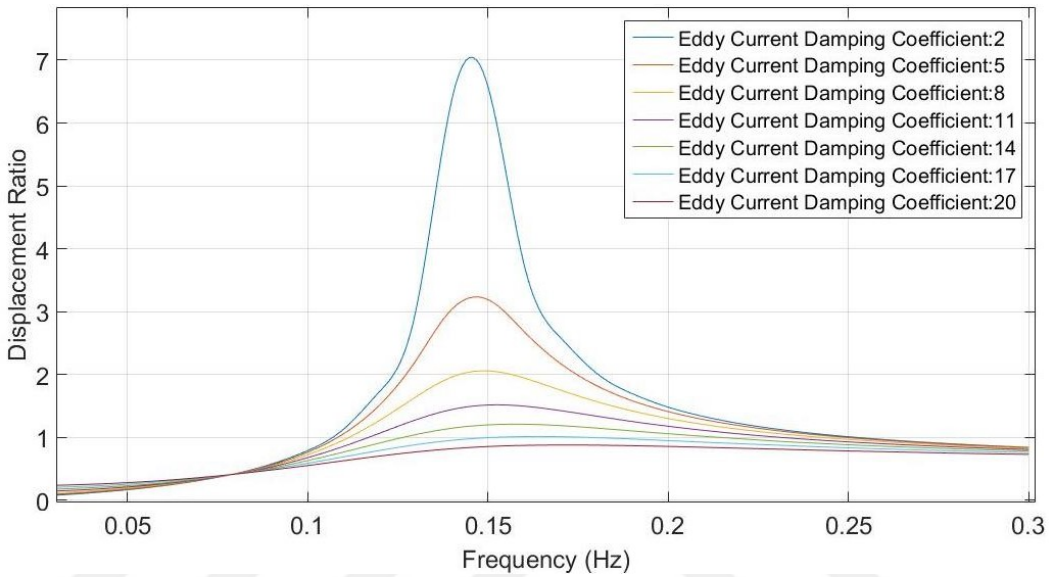

Figure 2.16. Transmissibility of the Thrust Stand

Mass asymmetries in the thrust stand affect the transmissibility. Vertical mass difference, which is the difference between upper and lower parts, changes natural frequency, therefore affects transmissibility. Vertical mass difference does not have a significant effect at higher frequencies (Figure 2.17).

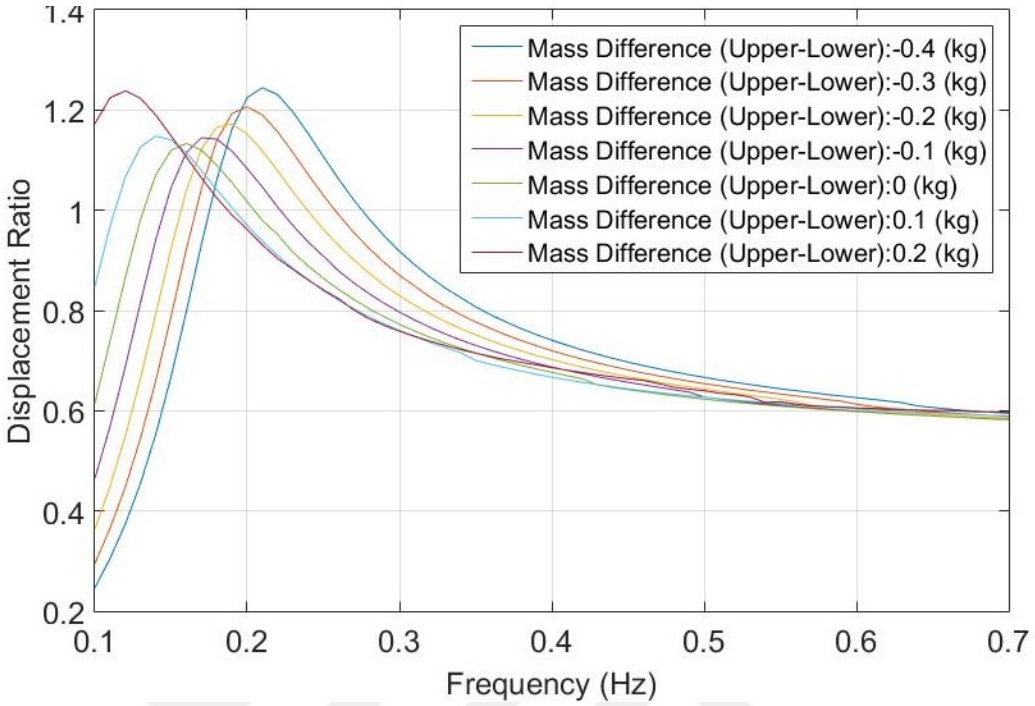

Figure 2.17. Transmissibility vs. Vertical Mass Difference

2.4.3. Analytical Solution of the Thrust Stand Response

Analytic solution of the transient response equation of the thrust stand is obtained by eliminating base excitation, damping and negligible terms. Small angle approximation is used to simplify the equation:

$$sin(\theta) \approx \theta \tag{2.22}$$

$$cos(\theta) \approx 1 \tag{2.23}$$

Thus equation 2.17 reduces to:

$$\ddot{\theta}(t) = \left[F_{thruster}H + M_{dif}gH\theta - 12k\theta\right]\frac{1}{J + M_{dif}H^2} \tag{2.24}$$

Laplace Transformation is applied to equation 2.24 with zero initial conditions:

$$\Theta(s) = \frac{F_{thruster}H}{s}\frac{1}{s^2(J + M_{dif}H^2) + 12k - M_{dif}gH} \tag{2.25}$$

After applying inverse Laplace Transform, analytic transient response solution is obtained:

$$\theta(t) = \frac{F_{thruster}H}{12k - M_{dif}gH}\left[1 - cos\left(t\sqrt{\frac{12k - M_{dif}gH}{J + M_{dif}H^2}}\right)\right] \tag{2.26}$$

It can be seen that the coefficient of equation 2.26 is same as that of equation 2.14, which corresponds to the steady state value. Natural frequency of the thrust stand can be obtained from this equation:

$$w_n = \sqrt{\frac{12k - M_{dif}gH}{J + M_{dif}H^2}} \tag{2.27}$$

If the thrust stand is perfectly balanced ($M_{dif} = 0$), then natural frequency and steady state response reduce to:

$$\theta = \frac{F_{thruster} H}{12k} \tag{2.28}$$

$$w_n = \sqrt{\frac{12k}{J}} \tag{2.29}$$

In equation 2.26, the term in the square root in the cosine, determines the stability of the system. If this terms is negative, then a complex number forms in the cosine, which transforms it to hyperbolic cosine. In this case deflection of the system increases with time and system will be broken. Therefore maximum allowed mass difference between the upper and lower parts are given as:

$$M_{dif} < \frac{12k}{gH} \tag{2.30}$$

2.4.4. Analytical Model of Thin Flexures

Torsional pivot bearings are considered in the initial design steps, however the pivots are then changed with thin flexural strips. Design parameters of these strips are determined through analytical and numerical analyses. In analytical analysis, bending stiffness and bending response of the thin metal strips are calculated. Bending is caused by the applied thrust force. Both ends of the strips are attached to neighbouring pendulum parts, therefore these edges are constrained. As the angle of horizontal platforms and outer frame parts are fixed, end edges of the strips, which are attached to these parts have fixed displacement angle, which is zero. Other edges of the strips have a displacement angle that is equal to the angle of the pendulum arm.

Because of the geometric constraints, all strips have same deformation shape, which means that they are affected by the same force and moment. Therefore all strips can be represented as a single strip connecting the pendulum arm to the fixed base as shown in Figure 2.18.

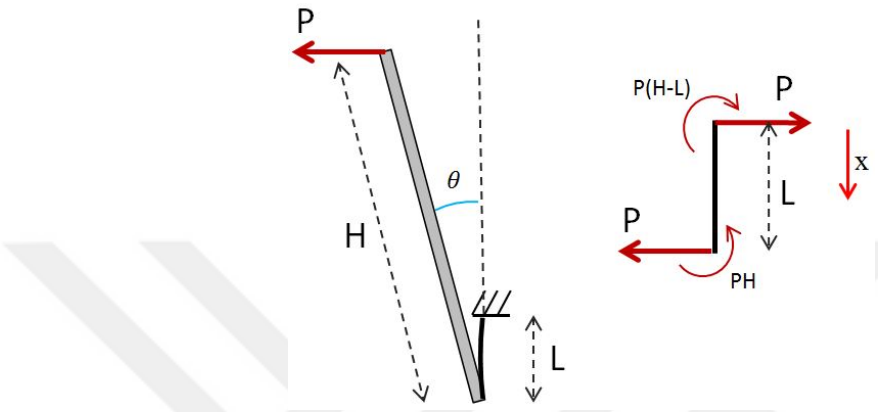

Figure 2.18. Simplification of the pendulum structure as one strip and a pendulum arm (left), free body diagram of the strip (right)

In Figure 2.18, P represents the applied thrust by the thruster, H is the pendulum arm length, L is the length of the strip and θ is the deformation angle. Bending deformation diagrams for shear force and moment are shown in Figure 2.19. Here shear force and moment are applied to the strip together.

Euler-Bernoulli beam equation is used for the analysis:

$$\frac{d^2}{dx^2}\left(EI\frac{d^2w}{dx^2}\right) = q \tag{2.31}$$

where, E is the Modulus of Elasticity, I is the area moment of inertia, w is deformation and q is distributed load. Strips are considered uniform and homogeneous. After integrations of Equation 2.31 shear force and moment equations for bending are obtained:

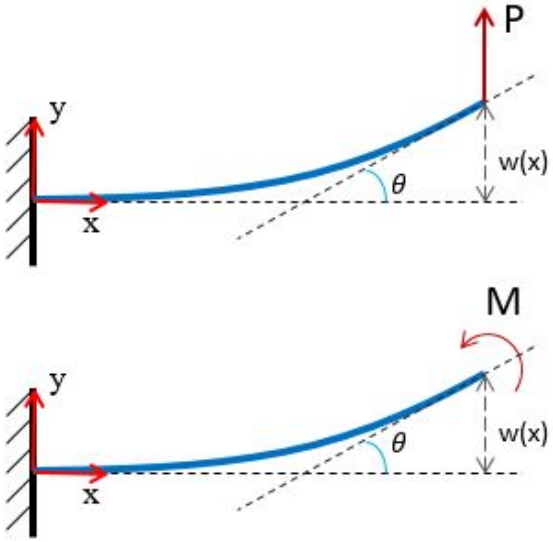

Figure 2.19. Bending diagrams of flexural elements

$$EI\frac{d^3w}{dx^3} = V \tag{2.32}$$

$$EI\frac{d^2w}{dx^2} = Vx + c_1 \tag{2.33}$$

where V is shear force, which is equal to P thrust force. As moment at $x = 0$ is equal to the moment at fixed based, which is $P(H - L)$, constant c_1 is equal to $P(H - L)$. After integrating Equation 2.33 and applying fixed base boundary condition, angular displacement equation is obtained:

$$EI\frac{dw}{dx} = \frac{Px^2}{2} + P(H - L)x \tag{2.34}$$

where dw/dx is the slope of the strip and is equal to $tan(\theta)$. As the deflection of the pendulum is very small, small angle approximation, $tan(\theta) \approx \theta$ is valid. Hence total deflection angle at edge of the strip $x = L$ becomes:

$$EI\theta = \frac{PL^2}{2} + P(H - L)L \tag{2.35}$$

$$\frac{EI}{L}\theta = PH - \frac{PL}{2} \tag{2.36}$$

where EI/L is the total bending stiffness k_t of the strips. Hence,

$$k_t\theta_{max} = PH - \frac{PL}{2} \tag{2.37}$$

Area moment of inertia of each strip is $I_s = wt^3/12$. Where w is the width and t is the thickness of the strips. There are 12 strips in the thrust stand. Therefore equation 2.37 becomes:

$$\theta\frac{Ewt^3}{L} = PH - \frac{PL}{2} \tag{2.38}$$

where Ewt^3/L is the total stiffness of the pendulum mechanism. Equation 2.38 can be summarized as:

$$k_t\theta = M \tag{2.39}$$

where M is average of the applied moment along the length of the strip.

2.4.5. Numerical Model of Thrust Stand with Flexures

Numerical analyses are conducted by using the structural mechanics module of COMSOL Multiphysics. Pendulum arms and horizontal plates have much higher rigidity than flexible thin strips, therefore these plates are modelled with solid mechanics physics of structural mechanics module. The thin strips are modelled with shell physics. In shell module of COMSOL, the thin strips are evaluated as 2D domains, so that number of nodes and computational time is decreased. Computational grid is shown in Figure 2.20.

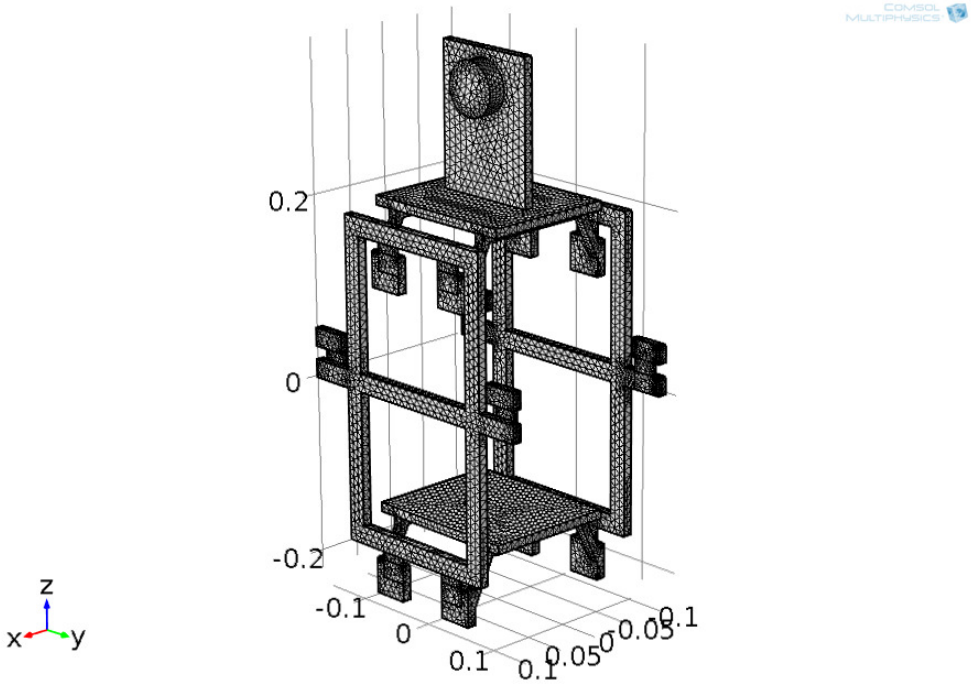

Figure 2.20. Finite element modelling of thrust stand

In the analysis, the pendulum mechanism is attached to four constrained rigid parts, which represent the outer support structure. Rest of the pendulum is free to move. Thrust is applied through the thruster as shown in Figure 2.21. The pendulum has a single degree of freedom. Close views of the bending of the thin strips are shown in Figure 2.22. Bending stress within the flexures are much lower than the yield stress of the flexures. Thrust vector does not change during operation, also position and dimensions of the thruster does not affect the results. Pendulum displacement changes linearly with the applied thrust as shown in Figure 2.23a. Thin flexures with different thickness values are investigated as shown in Figure 2.23b. According to the analysis and considering the displacement sensor that is utilized, flexure thickness of 0.1 mm is chosen. Flexure width and length is determined according to the analysis and design considerations. During the analysis, displacement between the upper and bottom platforms are calculated, as the displacement sensor will be placed between these two horizontal platforms.

Transient analysis is conducted for the natural frequency investigation. Natural frequency of the thrust stand at the optimized flexural parameters is around 0.25 Hz as shown in Figure 2.24. As the natural frequency of the thrust stand is much lower than the dominant frequency of the vibrations in the vacuum chamber, a mechanically filtered displacement measurement can be achieved. Also, any resonance with the external vibrations is avoided.

2.4.6. Strength Analysis of Flexures

As seen in finite element analysis, bending stress that is caused by the applied thrust is at negligible levels. Axial load on the flexures is the main factor that determines the load capacity of the thrust stand. Flexures are made of 304 grade stainless steel, which has yield stress around 200 MPa. In the optimization process the dimensions of the flexures are determined as 0.1 mm thickness and 20 mm width. Tensile stress in the flexures can be calculated with the equation $\sigma = F/A$. According to these formula, maximum load per flexure without yielding is 400 N.

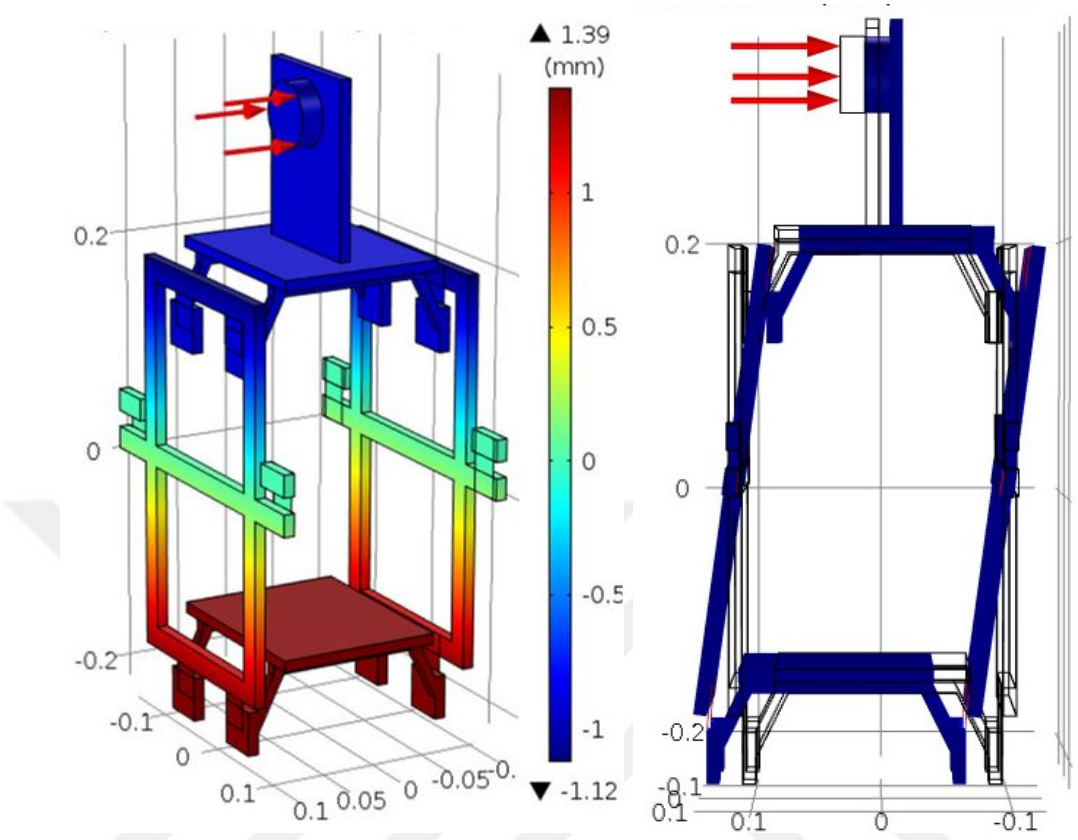

Figure 2.21. Finite element solutions of thrust stand with 0.1 mm flexure thickness for 20 mN thrust, a) Contour plot of displacement of pendulum structure, b) Side view of pendulum deflection

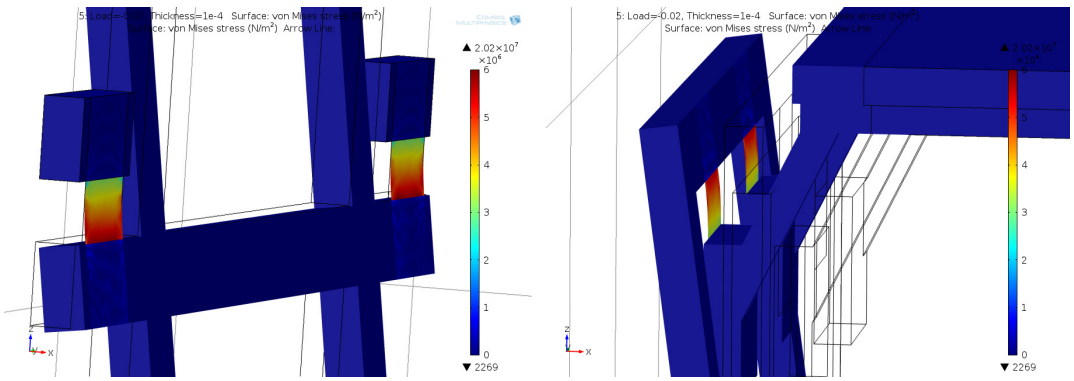

Figure 2.22. Bending of the flexural strips, von Mises stress within the flexures are shown for applied thrust of 20 mN

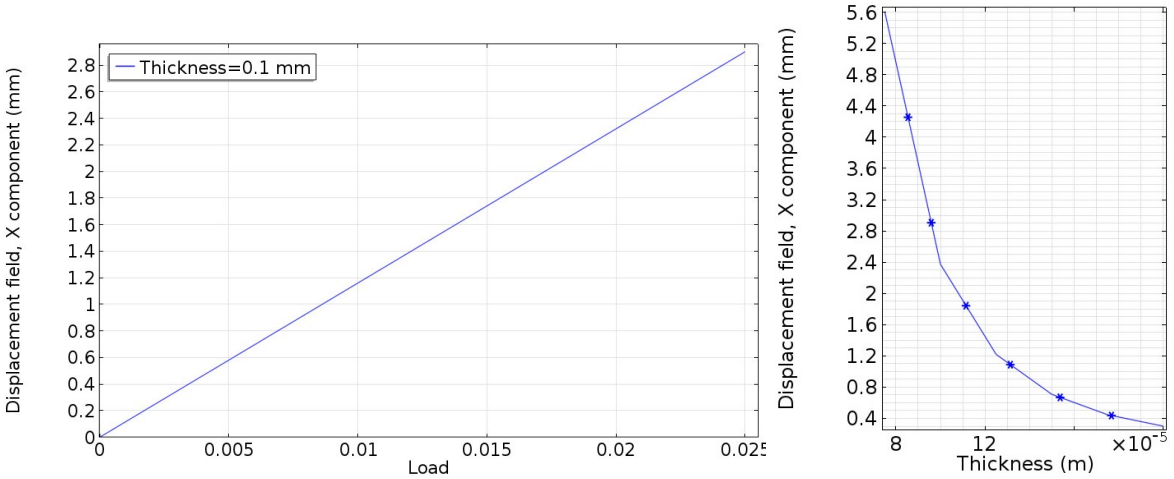

Figure 2.23. Displacement for 0.1 mm flexure thickness a) at different thrust levels, b) at different flexure thickness values

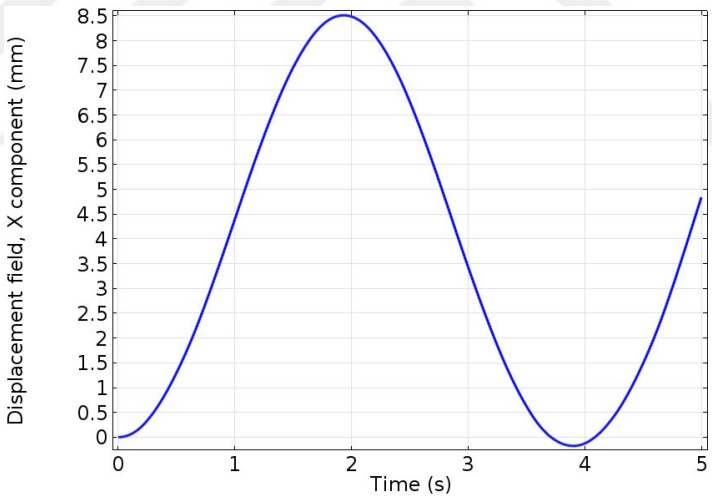

Figure 2.24. Transient displacement of thrust stand with 0.1 mm flexure thickness for 20 mN thrust

As the pendulum is attached to the support frame through four parallel flexures, maximum capacity of the thrust stand is 160 kg. During measurements the thruster mass has to be balanced with counterweights, therefore maximum thruster mass that can be supported is 80 kg. The heaviest thruster that is developed at BUSTLab is the MET, which is around 10 kg. Therefore, a minimum safety factor of 8 is achieved.

2.5. Components of the Thrust Stand

2.5.1. Flexural Strips

Pendulum components are attached to each other through flexural thin strips. In total 12 flexures are used. Flexures are made of 304 grade stainless steel with dimensions of 0.1 mm thickness, 20 mm width and 50 mm length. The sections that bend between the holder parts are 30 mm in length. Flexures at different thickness values such as 0.2 mm and 0.25 mm are also manufactured. By changing the flexures, the measurement range of the thrust stand can be changed. With thicker flexures, thrusts at Newton levels can be measured. Flexures are manufactured from thin plates with water jet cutting. High pressure water jet cutting helps avoiding any deformation during manufacturing. After cutting process, a Dremel grinder tool is used for deburring, so that a clean finish is obtained. Each flexure is compressed between two parts at both ends as shown in Figure 2.25. Friction between the surfaces hold the flexure between the plates and avoids excessive stress around the screw holes. Flexures provide highly frictionless motion and have negligible hysteresis.

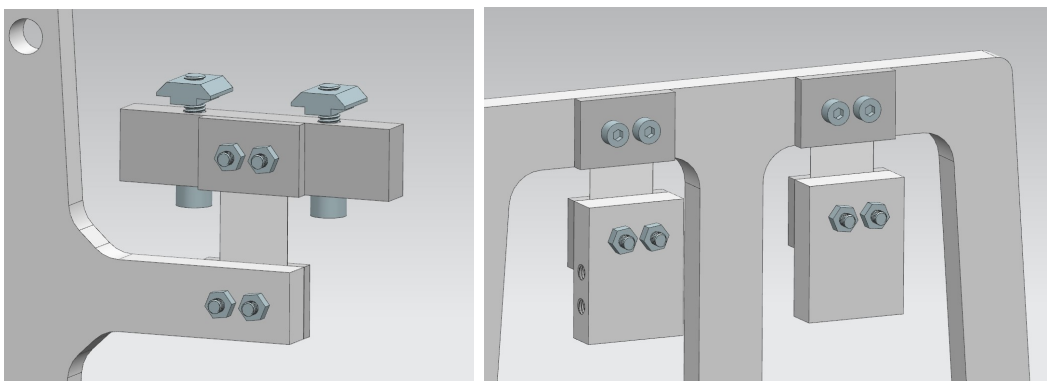

Figure 2.25. 3D drawing of flexural strips a) Between the pendulum and support frame, b) Between the pendulum and upper platform

2.5.2. Sensors

2.5.2.1. Displacement Sensor. Motion of the pendulum is measured through a displacement sensor. The displacement sensor is utilized both at calibration and measurement process. Selection of the displacement sensor is critical for thrust measurements. There are several criteria for the required sensor. The sensor has to be suitable for high vacuum operation. Outgassing from the sensor should be at low levels, so that pressure inside the vacuum chamber can be kept at high vacuum conditions. As the measured thrusts is very low, any external contact may harm the measurements, therefore contactless measurement is preferred.

As displacement sensor, LVDT (Linear Variable Differential Transformer) sensor is selected to be used in the thrust stand. LVDT sensors consist of three coils that are wrapped around a tube. A ferromagnetic core part, which is attached to the displaced object, is placed inside the tube. An alternating current is supplied to the center coil, and a voltage is induced in other two secondary coils. This voltage is proportional to the absolute position of the core part [48]. LVDT provides contactless thrust measurement at high sensitivity with a relatively low price. The sensor that is used is DC-SE 100 of Measurement Specialties (Figure 2.26). It has a measurement range of 2.54 mm with a sensitivity of 1.97 V/mm. The output signal is between 0 and 5 V, which is suitable for many control devices.



Figure 2.26. LVDT displacement sensor

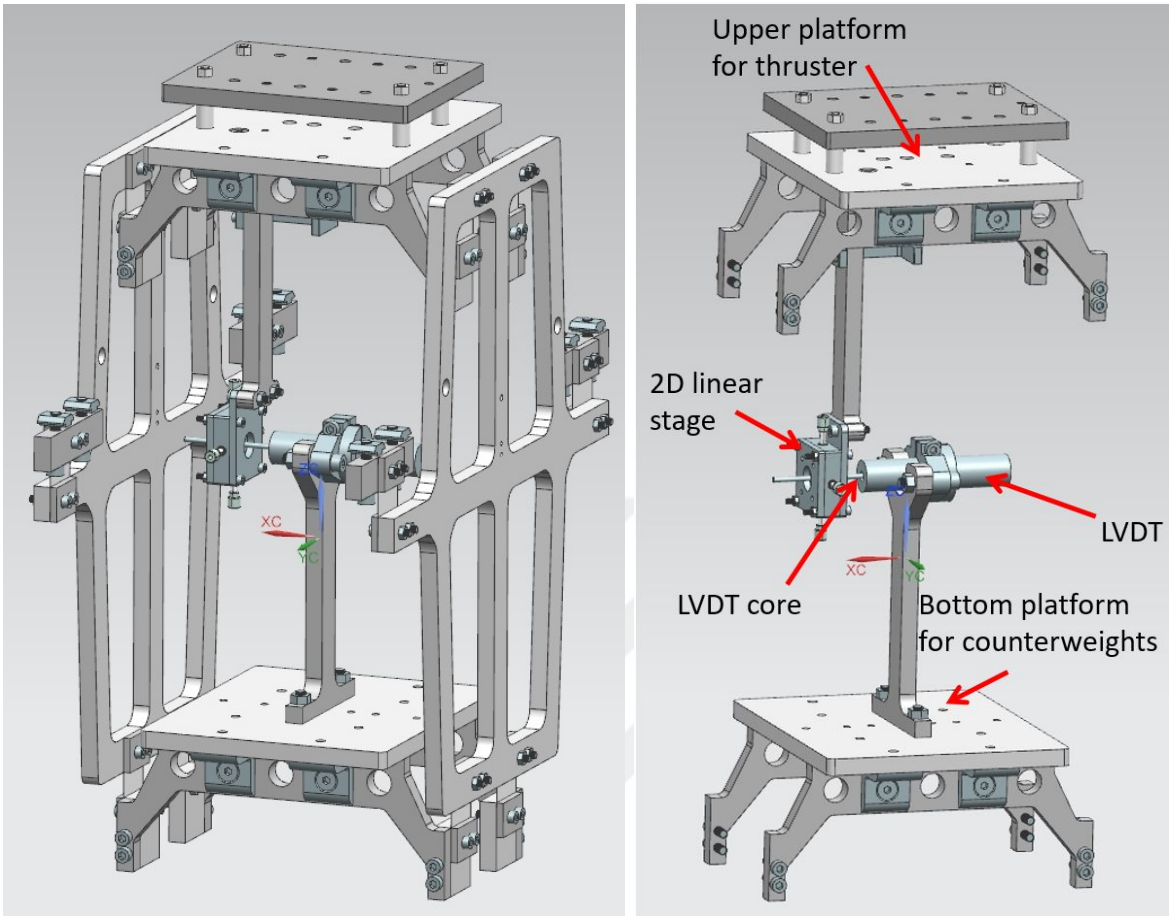

Figure 2.27. 3D drawing of the displacement sensor assembly

The LVDT consist of a sensor and a core part. The sensor measures the displacement of the core part. Sensor part is attached to the upper platform through a vertical bar, while the core part is attached to the bottom platform as shown in Figures 2.27 and 2.28. Since the natural frequency of the pendulum mechanism is very low, external vibrations in the vacuum chamber are mechanically damped within the system. LVDT measures the displacement between the upper and bottom parts of the pendulum, so that a mechanically filtered output signal can be obtained.

Position of the core part can be adjusted with a 2D linear stage. The stage is built from three square plates. Thinner side plates capsulate a small square part that is placed inside the hollow middle plate. The square plate has a tapped hole for a screw that holds the core part, thus position of the core inside the sensor can be adjusted.

Four fine adjustment screws are inserted to the middle hollow plate of the stage. Position of the core part can be adjusted in three axis with high sensitivity. Linear stage parts are manufactured with water jet cutting from aluminium and then machined.

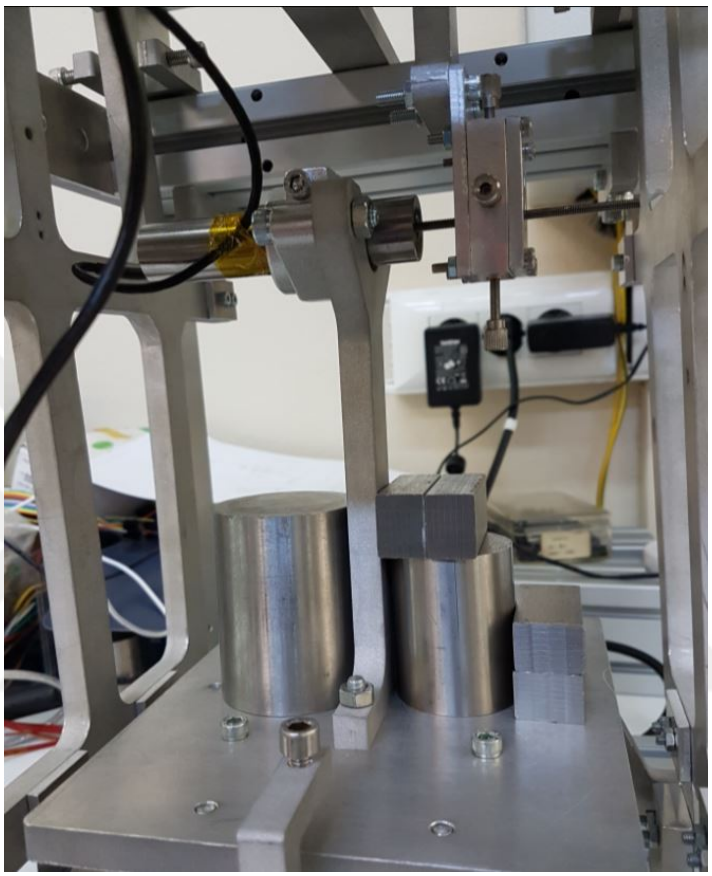

Figure 2.28. Displacement sensor assembly and counterweights

2.5.2.2. Thermocouples. Thermal drifts within the system is the main cause of the measurement errors. The thrusters, cathodes, sensors and actuators generate heat during the operation. Thermal control of the thrust stand is significant for measurement accuracy. Therefore, temperature at various important points are measured with thermocouples. J and K type thermocouples are used for thrust stand. Measured points are the sensors, upper platform, thruster carrier plate, and power cables for the thrusters. LVDT and load cell is sensitive for temperature variations. Also, they may be damaged from high temperature. During the tests it was seen that temperature of sensors do not change significantly. They consume low power and also during the assembly process they are mounted on conductive support parts to increase conductive heat transfer.

2.5.3. Calibration System

Calibration is the most important step of thrust measurements. As the measurements are affected from the experimental conditions, most accurate calibrations can be performed just before the thrust measurements at the same conditions. Therefore, a calibration mechanism that can be utilized at high vacuum conditions with remote control is needed. Response of the system to the applied thrust is measured with the calibration. A dummy thrust is applied to the pendulum structure with an actuator and the thrust stand response to the thrust is measured. During the design and manufacturing process, two different calibration designs are proposed and tested. In both designs a load cell is used for the calibration. Load cells utilize strain gauges and converts the applied mechanical force to electrical signals. By reading these signals,the applied force is calculated. The load cell that is utilized in the thrust stand is GS0-10 load cell (Figure 2.29) of Transducer Techniques, which has a sensitivity of 50 mV/mN and can measure forces up to 100 mN. Load cell is calibrated separately before the tests by applying known forces with calibration weights.



Figure 2.29. Load cell that is used in calibration

In the first calibration system design, a voice coil is utilized as the actuator. The voice coil consists of a permanent magnet and a copper wire solenoid. When a current is applied to the solenoid a magnetic field is generated, which pushes or pulls the permanent magnet that is placed inside the solenoid. Voice coils can generate forces without any contact. In the thrust stand, voice coil of Moticont with the model number of LVCM-010-013-01 is used. Sensitivity of the voice coil is 290 mN/A. It can generate forces up to 280 mN. Generated force is linearly dependent on the applied current. Voice coil is mounted between the upper and bottom platforms of the thrust stand. Coil part is attached to the bottom platform, while magnet part is attached to the upper platform through the load cell via an aluminium part between the load cell and voice coil as shown in Figure 2.30.



Figure 2.30. Initial calibration mechanism design with load cell and voice coil, and LVDT assembly

During the calibration, currents at different levels are applied to the coil. Generated force is measured with the load cell, while the pendulum deflection is measured with LVDT.

Stiffness of the system can be found from the ratio of the deflection and applied force. Voice coil can be controlled remotely, so that in-situ calibration in high vacuum can be performed. However, connecting the voice coil and load cell proved to be difficult, and precise alignment could not be achieved. Also, as the voice coil is mounted on the load cell, its weight causes some measurement errors at the load cell and causes undesired vibrations.

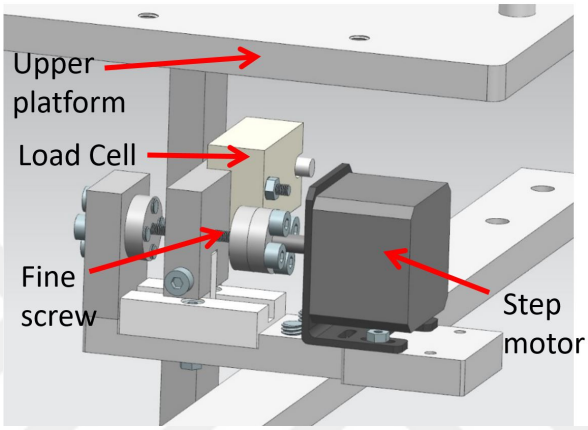

Figure 2.31. 3D drawing of the calibration mechanism with load cell and linear stage

In the second calibration system design, a linear motorized stage is utilized as actuator. A linear stage that fits into the required dimensions is designed and manufactured as shown in Figure 2.31. It is actuated with a step motor with a resolution of 1.8 degree/step. Step motor is attached to a fine adjustment screw via a coupling part. Thorlabs M6 fine adjustment screw with 0.25 thread length is used. The screw is inserted into a threaded bushing part, which is fixed to a platform with vacuum grade epoxy. Load cell is mounted on the platform, which can move on a Teflon rail. When the step motor is actuated, the platform slides along the rail. A linear sensitivity of 1.25 μm/step is achievable. Without considering the external perturbations, a resolution of 20 μN can be achieved for a thrust measurement range such as 20 mN, which will be used during low thrust measurements. With a linear stage, a more rigid calibration system is obtained. Calibration system is mounted on an aluminium bar on the upper side of the thrust stand as shown in Figure 2.32. Load cell is pushed towards the vertical bar that is attached to the top platform and holds the core part of LVDT. When actuated, the load cell applies a dummy thrust to the vertical bar. Applied force

is measured with the load cell, while deflection is measured with the LVDT.

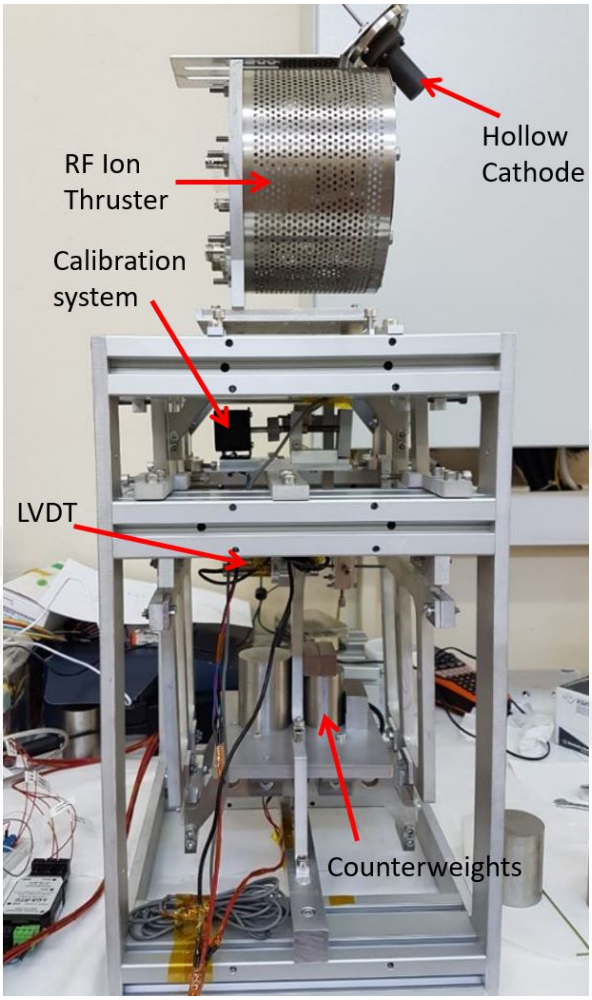

Figure 2.32. Side view of thrust stand with RF Ion Thruster

2.5.4. Damping System

Flexural strips provide highly frictionless motion to the pendulum mechanism, so that the motion of the pendulum is not damped for a long time. Also, undesired oscillations may be caused by the external perturbations. These vibrations should be damped with a damper mechanism. As the damper mechanism, an eddy current damping system is used. It consists of a copper plate, which is attached to the bottom platform, and two electromagnets, which are placed at each side of the copper plate as shown in Figure 2.33. Electromagnets are mounted on aluminium brackets that are attached to an aluminium profile, which is mounted on the support frame.

A copper plate is also attached to the platform via four bracket. Brackets and copper plate are manufactured with water jet cutting with high precision. When a current is applied to the electromagnets, a magnetic field is generated between the electromagnets. As the copper plate moves with the pendulum, an eddy current is induced within the plate and a damping force is generated [49]. Damping ratio can be adjusted by applying different currents to the electromagnets.

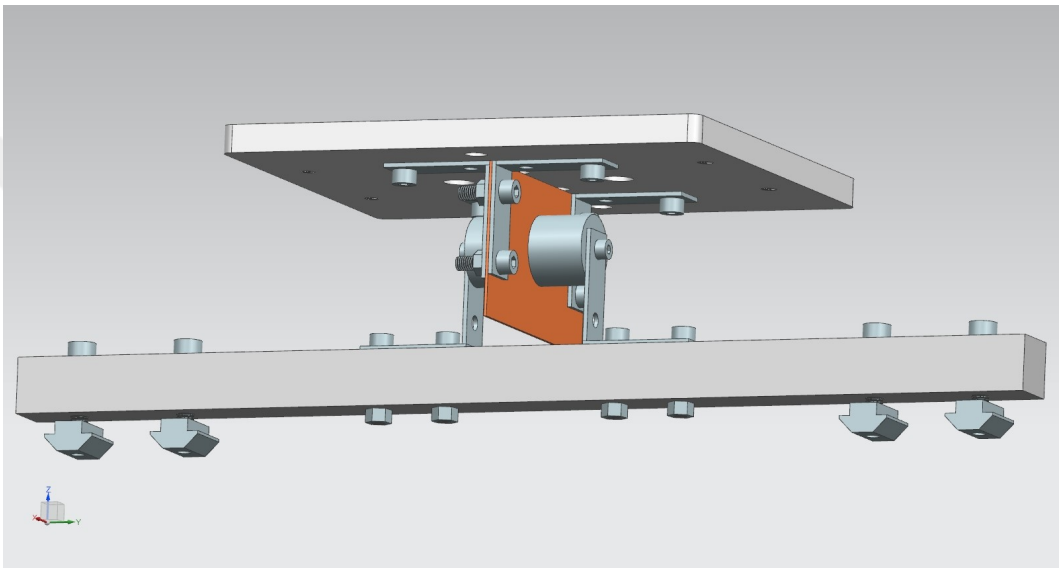

Figure 2.33. Eddy current damping system: Electromagnets and copper plate that is attached to the bottom plate

2.5.5. Counterweights

In order to balance the weight of the thruster, counterweights are mounted on the bottom plate. Stainless steel cylinders and bars at different masses are used as counterweights as shown in Figure 2.28. Counterweight mass is adjusted at calibration process. A higher counterweight mass increases the stability of the system and decreases sensitivity, and a lower counterweight mass increases sensitivity. However, counterweight mass should be higher than a certain limit to avoid tipping over. Thrust measurements are conducted with a slightly unbalanced configuration to achieve higher sensitivity.

2.5.6. Control System

Thrust stand controlled via Arduino Mega micro controller, which provides a low cost and moderate resolution control. The control hardware is placed outside the vacuum chamber and connected to the thrust stand via a vacuum feed-through (Figure 2.34). Control hardware schematic is shown in Figure 2.35. An Adafruit motor shield is attached to the Arduino board. Two linear stages, one for calibration and one for thrust stand positioning, are controlled via the motor driver shield. As the input pins of the Arduino supports voltage inputs between 0 and 5 volts, all the sensor outputs are designed to be in this range. Signal output of the LVDT sensor is connected to an analog input port of the Arduino. Load cell is connected to the amplifier. Signal output port of the amplifier is connected to an analog input port of Arduino. Analog input pins of Arduino board, and outputs can be read in 10 bits, which provide a resolution of 1024 steps.

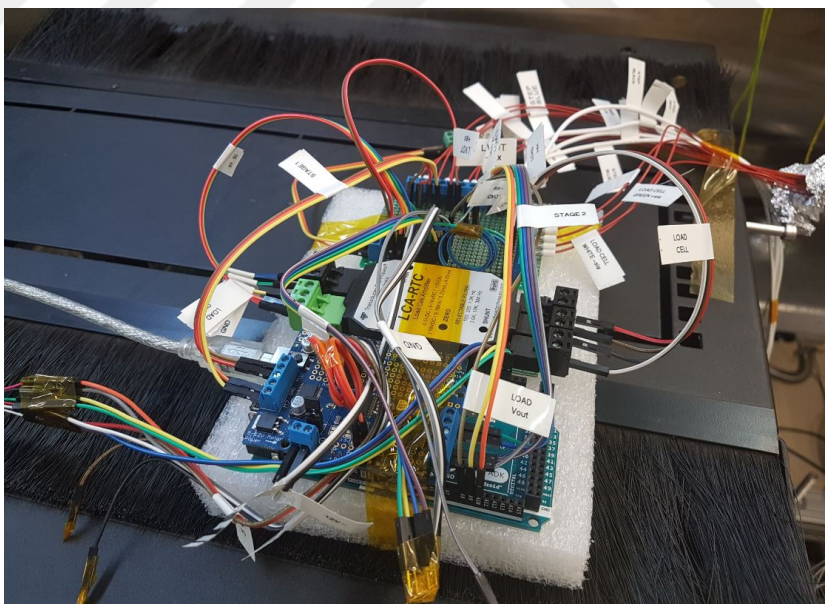

Figure 2.34. Control hardware

Energy is supplied to the system through a 12 V DC adaptor. Load cell amplifier, LVDT and motor driver is connected to the power supply. Arduino board is powered through the driver shield. All components are grounded to the vacuum chamber. Arduino board is connected to a computer through a USB cable.

When operated, calibration and thrust measurement processes are monitored from the computer. All cables are insulated with aluminium foils for electromagnetic interference protection.

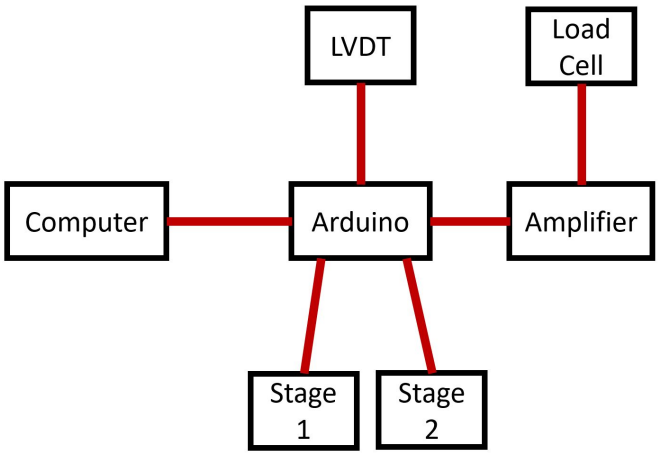

Figure 2.35. Control system schematic

2.5.7. Cabling and Piping

Power cables and propellant lines of the thruster introduce additional stiffness and hysteresis to the system. Therefore, cabling and piping should be achieved in a configuration that minimizes these effects. Pipes and cables of the thruster are hanged down in a waterfall configuration from an aluminium bar that is attached to the ceiling of the vacuum chamber (Figure 2.36). Pipes are connected to the thruster through a 90 ° turn, thus they do not apply a force to the thruster in the thrust direction.

2.5.8. Main Linear Stage

The effect of the cables and pipes are minimized with the waterfall configuration as explained in section 2.5.7, however their effect could not be totally prevented. Therefore, a small force that is applied to the pendulum in the direction of the thrust vector remains. This force causes drifts at null position of the pendulum. This drift is compensated using a linear stage. The thrust stand is mounted on a linear stage as shown in Figure 2.37.

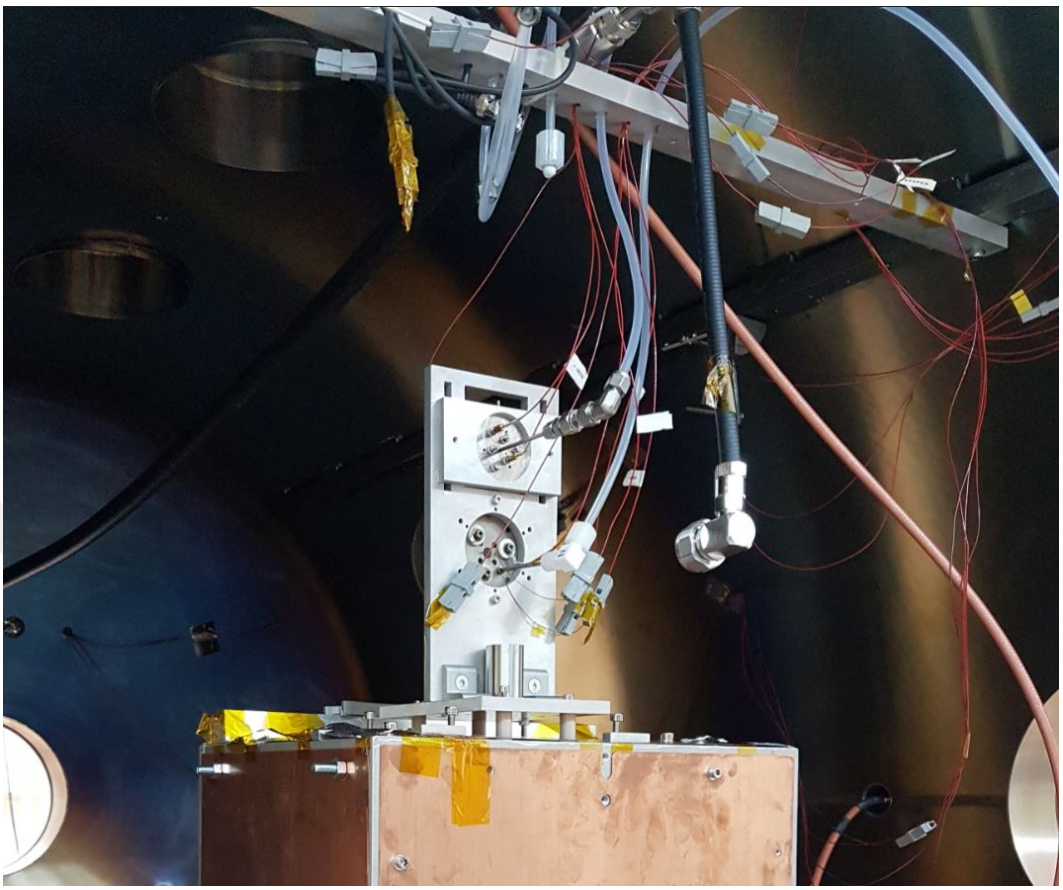

Figure 2.36. Waterfall cabling and piping configuration

Before the calibration process, thrust stand is moved according to the drift of the pendulum. Drift of the pendulum is measured with the LVDT. If cables pull the pendulum forwards, LVDT signal drops to zero and thrust stand has to be moved forward, so that the pull in the cables are compensated and LVDT signal increase just above the zero position. If cables push the pendulum backwards, then thrust stand is also moved backwards and the push in the cables is compensated. Position of the thrust stand has to be adjusted at each measurement and calibration sequence. Linear stage is driven with a step motor, which is controlled with the Arduino. Very sensitive position adjustment in high vacuum environment can be performed.

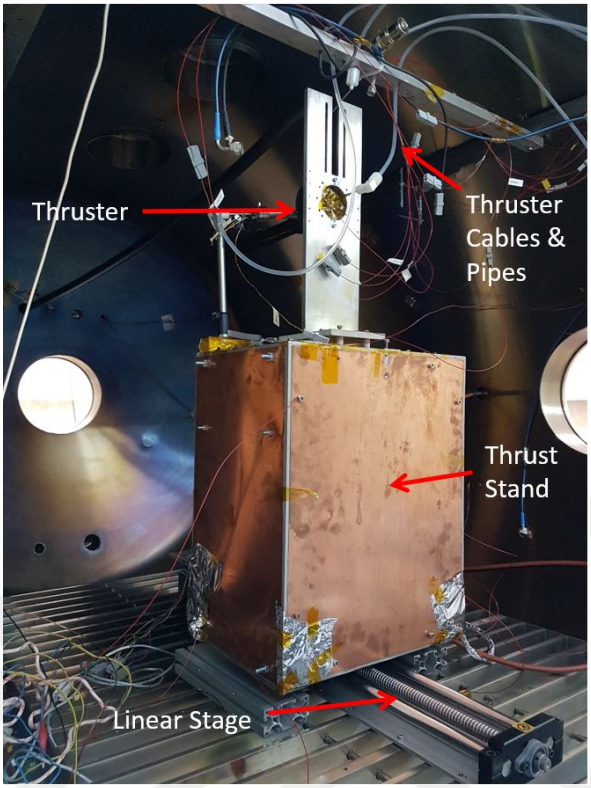

Figure 2.37. Thrust stand mounted on the linear stage

2.6. Thermal Analysis and Thermal System Design of Thrust Stand

Temperature changes may affect the measurement accuracy of the thrust stand, as temperature changes affect the stiffness of the fleuxures and temperature gradients may cause misalignments. Therefore, thrust stand has to be kept at constant temperature during the operation. Main heat source during the operation is the thruster. Since the thrusters are operated in high vacuum environment, convective heat transfer is negligible. Thus, heat generated by the thrusters have to be removed with radiative and conductive heat transfers. Conductive heat transfer to the thrust stand should be minimized for accurate measurements. In order to reduce conductive heat transfer, thrusters are mounted on PEEK (Polyether ether ketone) separator parts as shown in Figure 2.38 . PEEK has very low thermal conductivity and decreases heat flux to the thrust stand dramatically. Also, by separating from the thrust stand, thruster body can be kept at a floating electrical potential.

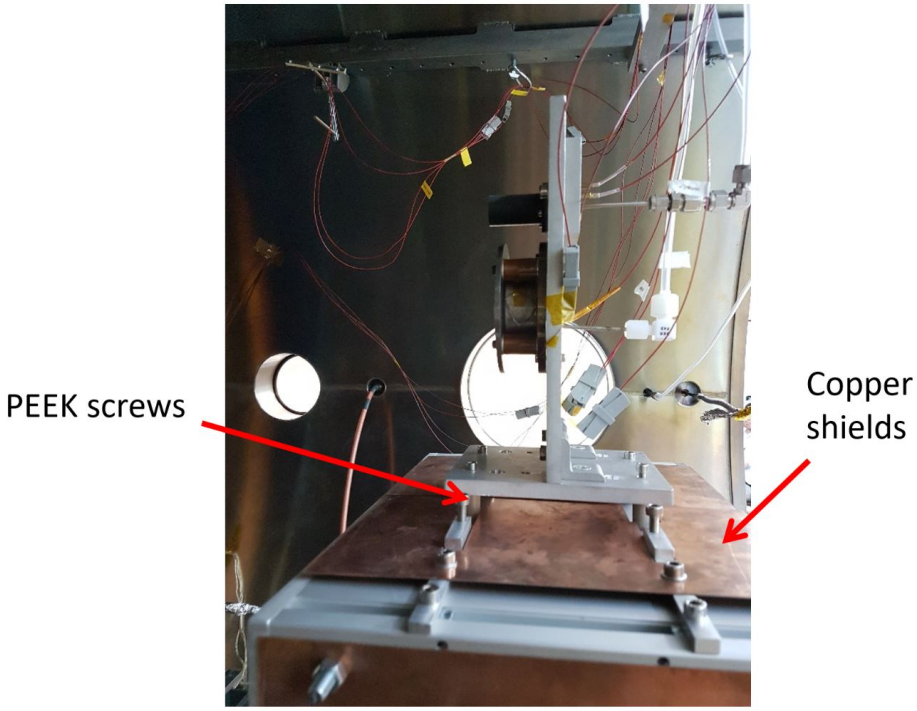

Figure 2.38. Thermal insulation of thrust stand

Heat transfer analysis is conducted using COMSOL Multiphysics according to the maximum heat generation, which occurs during the Hall thruster operation and cathode heating process. Heat transfer analysis is conducted for different thermal designs. Effects of radiation shields are investigated (Figure 2.39), and it was seen that PEEK separators can provide excellent thermal insulation and any radiation shields are not necessary. According to the thermal analysis, thrust stand can be kept at low temperatures during thruster operation. Also, during the tests, temperature measurements are conducted with thermocouples at various locations such as sensors and flexures. It was seen that heat flux to the thrust stand is at negligible rates.

During the tests the plasma inside the vacuum chamber may harm the electronic equipment of the thrust stand. Also, electromagnetic waves such as radiowaves and microwaves may interfere with the sensor signals. Therefore, thrust stand is covered with copper plates as shown in Figures 2.37-2.39. In order to allow venting in the vacuum, a perforated plate is used at the bottom of the thrust stand. Sensor cables are insulated from the plasma and electromagnetic interference with aluminium foils.

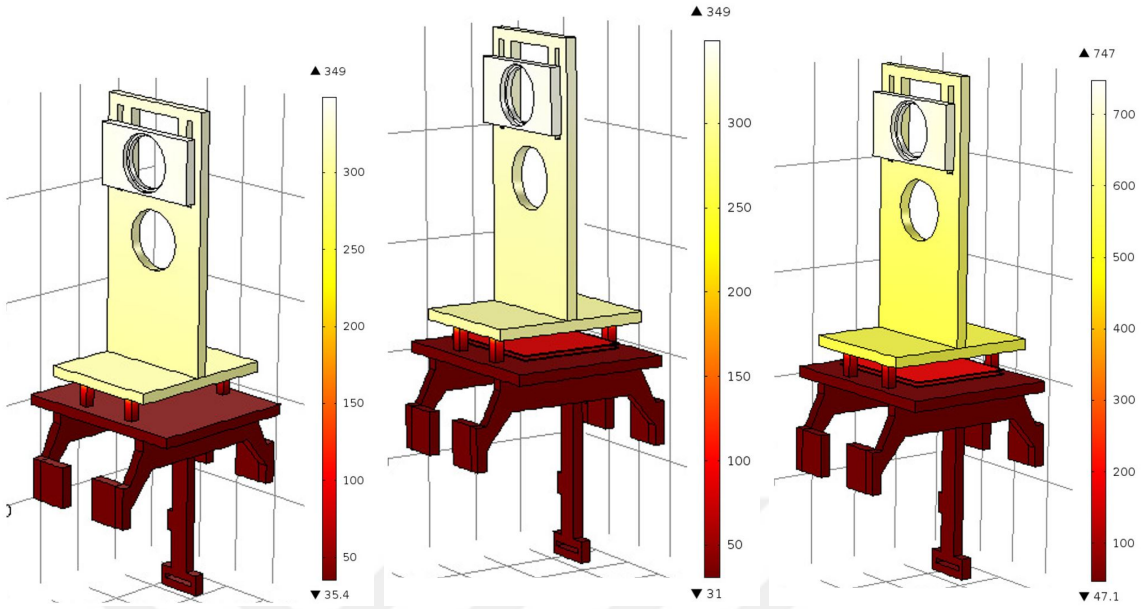

Figure 2.39. Thermal analysis of thrust stand: a) 40 W cathode power, b) 40 W cathode power with radiation shield, c) 200 W cathode power

2.7. Thrust Stand Operational Procedures

2.7.1. Thrust Stand Setup

Pendulum components and the plates that are used in the outer frame are manufactured from Aluminium 5083 alloy plates with water jet cutting. Drilling and surface finishing operations are performed through machining operations. All parts are cleaned with acetone and then isopropyl alcohol. In Figure 2.40, all components are shown in vacuum chamber before assembly.

Aluminium sigma profiles are used in the frame of the thrust stand. Vent holes are drilled to the profile parts. Six profiles are assembled with two aluminium plates as shown in Figure 2.41. Thus, a rigid support structure is achieved. After the frame structure is completed, pendulum arms and horizontal platforms are attached through thin stainless steel strips.

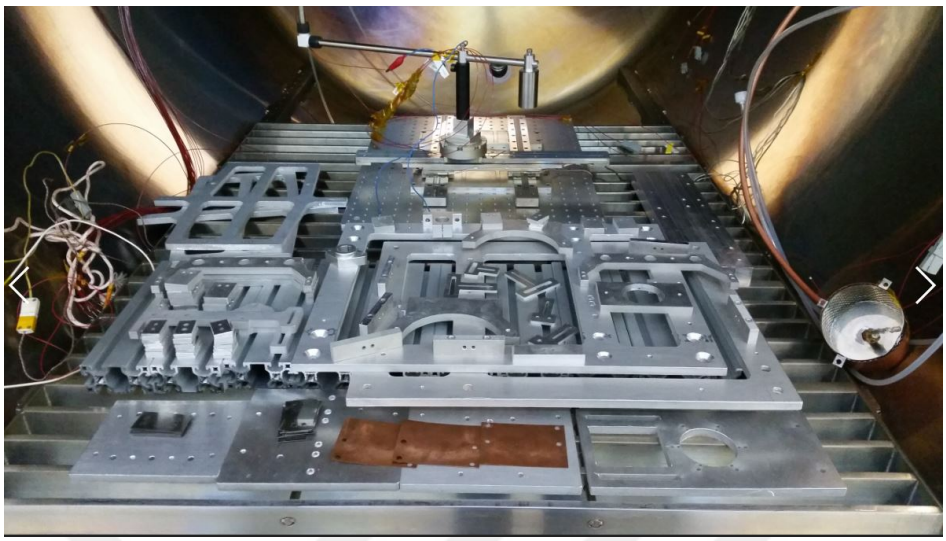

Figure 2.40. Thrust stand components in vacuum chamber

2.7.2. Safety Locks

In order to measure low thrust levels of the thrusters, connections with very low stiffness are used. Therefore, safety and locking mechanisms are needed when the thrust stand is not operational. Four locking parts are attached to the top face of the frame that anchor the upper platform with bolts. Four locking parts are attached to the middle profiles that can anchor the pendulum arms. The parts also act as stoppers to avoid excessive motion of pendulum arms. Also, two locking parts are attached to the bottom platform. Locking parts can be seen in Figure 2.42.

2.7.3. Counterweight Adjustment

After the pendulum structure is assembled, LVDT sensor, calibration and damping mechanisms are mounted to the thrust stand. The thruster that is to be tested is mounted on the upper platform, while counterweights are placed on the bottom platform. Stainless steel blocks are used as counterweights. Counterweight mass is adjusted according to necessary measurement range. Measurement sensitivity can be increased by decreasing the counterweight mass and destabilising the system. Several calibration sequences may be needed for fine adjustment of the counterweight mass.

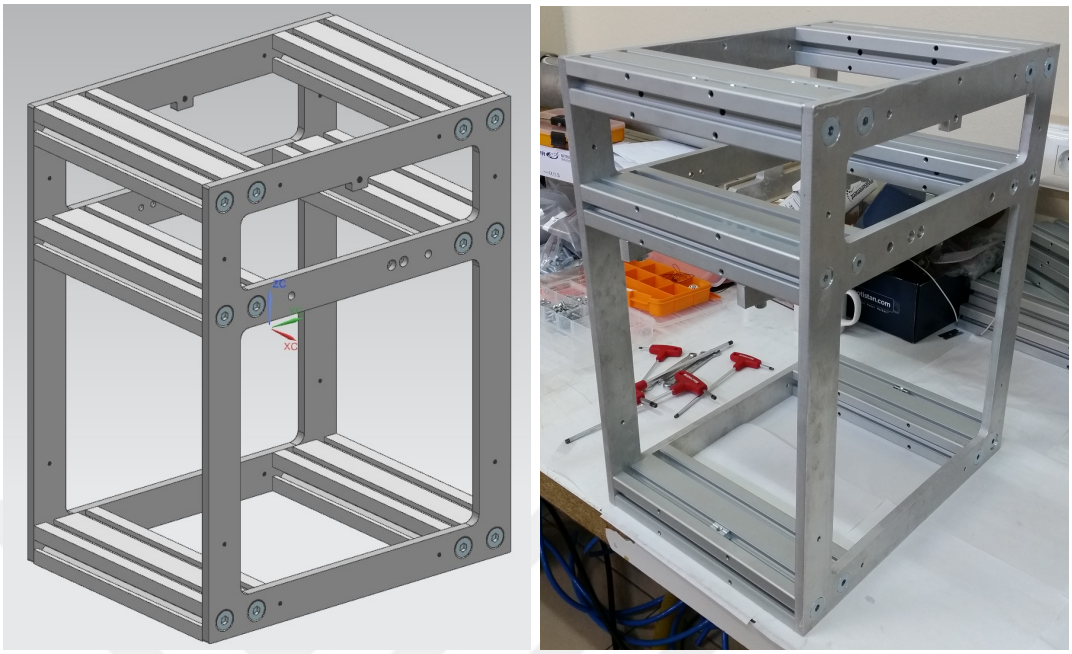

Figure 2.41. Thrust stand outer frame

2.7.4. Thrust Stand Positioning with Linear Stage

At the beginning of each calibration sequence position of the thrust stand has to be adjusted by using the linear stage that is placed under the thrust stand. LVDT feedback is used during the positioning. Thrust stand is shifted forward or backwards until all the external perturbations caused from the cables and pipes are eliminated. When the vibrations in the pendulum is damped and a clear and steady LVDT signal is achieved, calibration sequence is initiated.

2.7.5. Calibration of Thrust Stand

In situ calibration can be performed in high vacuum. Calibration algorithm is shown in Figure 2.43. Calibration begins with shifting the load cell with the linear stage towards the pendulum arm until a force is measured at the load cell. Then, the load cell is shifted slightly to apply a dummy thrust to the pendulum. Applied force is measured with the load cell, while pendulum displacement is measured with LVDT.

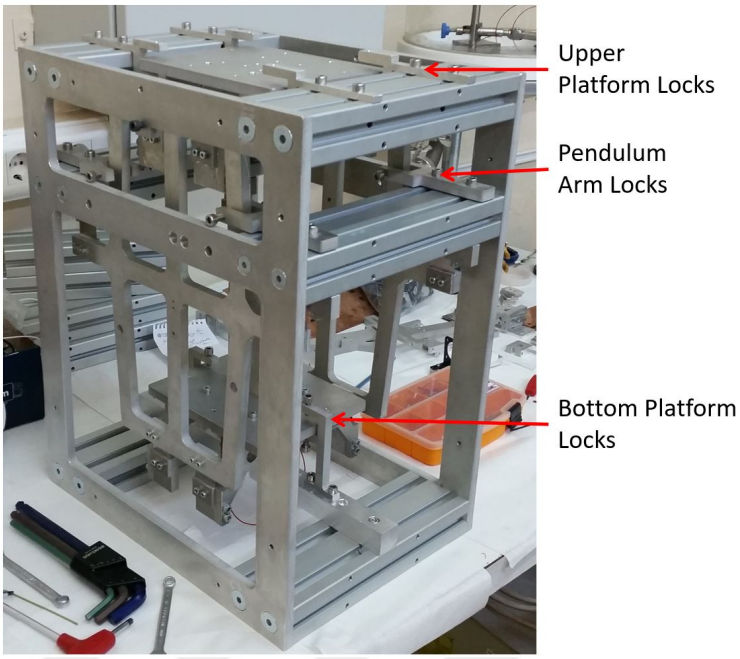

Figure 2.42. Safety locks

This process is repeated at least ten times. Each measurement is conducted after the vibrations are damped out. After the measurements are completed, load cell is moved to the initial idle position and stiffness is calculated by fitting the displacement and force measurements. Calibration is repeated several times before thrust measurements. During the thrust measurements, thrust is calculated from the LVDT signal by using the stiffness value that is obtained during calibration.

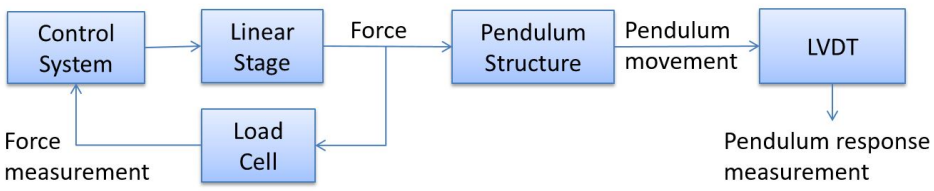

Figure 2.43. Calibration Algorithm

2.8. Uncertainty Analysis

Accuracy of the calibration process determines the accuracy of the thrust measurements. However, there are uncertainties within the calibration due to the external perturbations and resolution of the equipment. The level of uncertainty can be obtained from the linear regression analysis of the calibration data. During the calibration several calibration points are achieved by measuring the displacement for the applied force. Stiffness of the thrust stand is the slope of the linear fit of these calibration points. Slope of the linear fit can be calculated with following equation:

$$k = \frac{\sum_{i=1}^{n}(x_i - \bar{x}_i)(x_i - \bar{y}_i)}{\sum_{i=1}^{n}(x_i - \bar{x}_i)^2} \tag{2.40}$$

where, k is the stiffness of the thrust stand, n is the number of calibration points, x_i is the displacement value that is measured with the LVDT, $\bar{x}_i$ is mean value of displacement measurements, $\bar{y}_i$ is mean value of measured force values. During the linear regression analysis, standard deviation of the measurements are also calculated. An example calibration data is shown in Figure 2.44. Measured force and displacement values are shown with circles. Linear fit of the calibration is shown with the continuous line. Also, 95% prediction interval, which corresponds to 2 sigma standard deviation is shown with the dashed line. In this calibration example, 95% prediction interval corresponds to ± 2.32 mN uncertainty within thrust measurements. The coefficient of determination (R^2) of linear regression analysis can be calculated with the formula:

$$R^2 = \frac{\sum_{i=1}^{n}(y_i - \hat{y}_i)^2}{\sum_{i=1}^{n}(y_i - \bar{y}_i)^2} \tag{2.41}$$

where, R^2 is the coefficient of determination, which shows the goodness of the fit, and $\hat{y}_i$ is the force value calculated from the linear fit at the measured displacement. The linear fit at Figure 2.44 has R^2 value of 0.99731, which is an indicator of a good linear fit with a relatively small uncertainty.

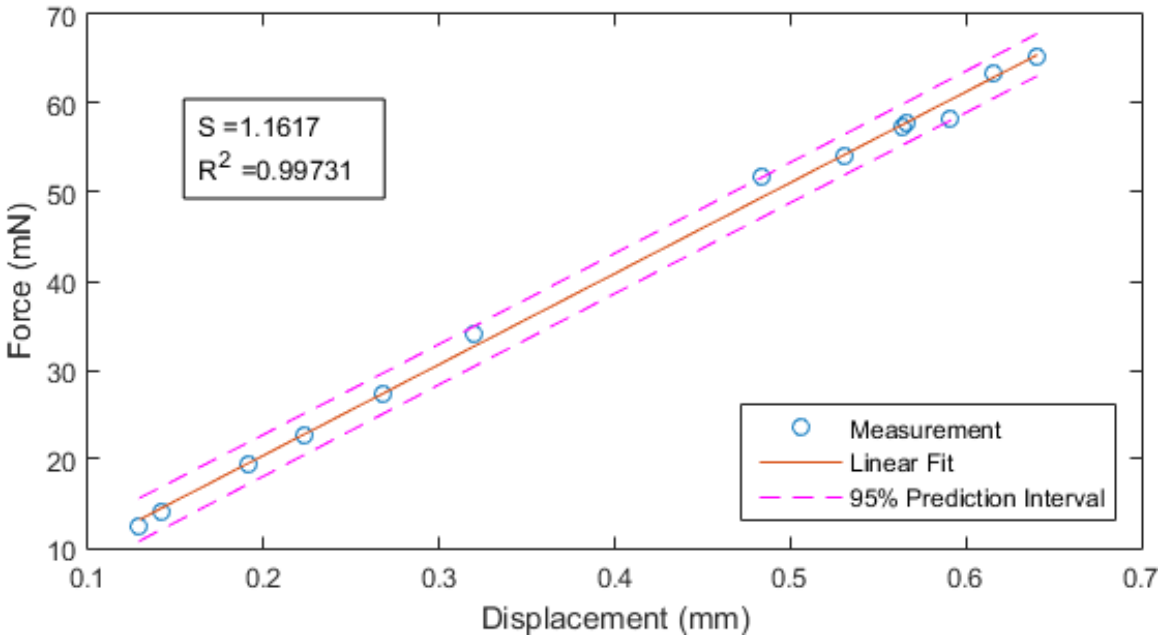

Figure 2.44. Calibration data with linear fit and 95% prediction interval

3. DEVELOPMENT OF UK90 HALL THRUSTER

With the experience gained from the HK40 Hall thruster, which is an SPT type low power Hall thruster developed at BUSTLab, a new and higher power Hall thruster is developed. New Hall thruster, which is called UK90 Hall thruster, has a power level similar to SPT-100, thus is suitable for station keeping maneuvers for satellites such as GEO communication satellites. UK90 Hall thruster utilizes the hollow cathode that is developed at BUSTLab. Highly compact size of the hollow cathode enables internal placement of the cathode at the thruster center axis as shown in Figure 3.1. Effects of the internal cathode placement will be investigated in section 3.1. Magnetic topology of the thruster is highly important for its operational characteristics. An extensive magnetic analysis is conducted. The thruster utilizes a single inner coil, which covers the internal cathode, and four outer coils. Thermal control of the thruster is also highly important. Thermal analyses for cathode and thruster are conducted.

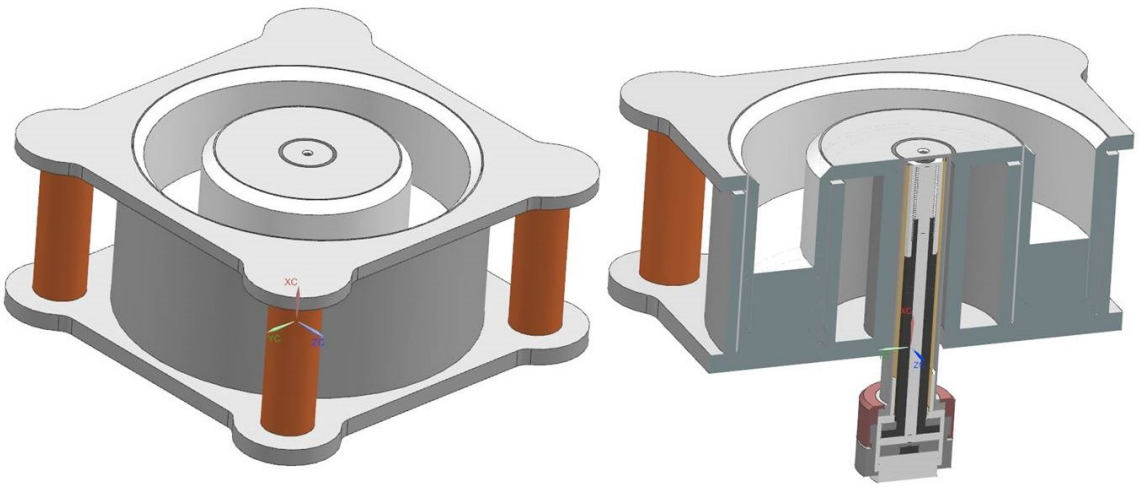

Figure 3.1. 3D drawing of Hall thruster with internal hollow cathode configuration

3.1. Internal Cathode Configuration

Hall thrusters utilize cathodes for the ionization of the neutral gas, and also for the neutralization of ion plume. Cathode coupling voltage is one of the major characteristics of the Hall thrusters, which is the potential difference between the cathode ground potential and beam plasma potential, and defines the voltage that extracts the electrons from the cathode to the anode [22, 50]. Cathode coupling voltage is shown as V_c in Figure 3.2. A lower cathode coupling potential decreases the power that is used to extract electrons from the cathode, thus increases efficiency. Cathode position is one the major factors that affects the cathode coupling voltage [51]. Cathodes can be placed internally within the center core or externally outside the outer pole. In smaller Hall thrusters, external cathodes are obligatory because of the sizing limitations. However, in larger Hall thrusters internal cathodes are more desirable [1, 52]. According to the studies that investigated the effect of the cathode position, better results are achieved with internal cathode configuration.

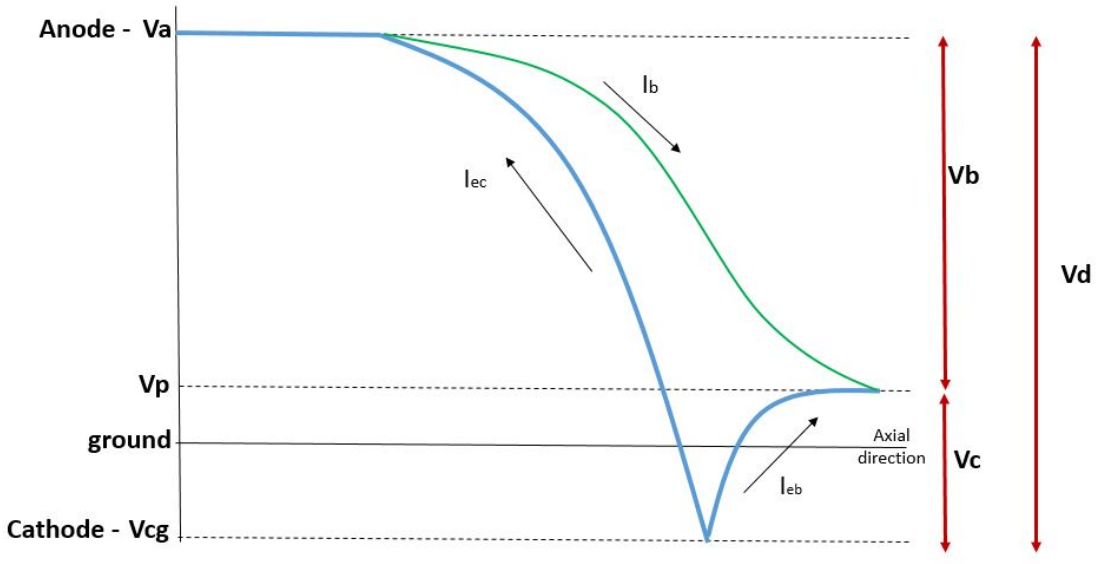

Figure 3.2. Hall thruster voltage schematic [22]

Hall thrusters have axisymmetrical designs, however external cathodes introduce asymmetries and affect the plume [53]. With internal cathodes, ion and electron densities are evenly distributed in the discharge channel and plume regions. Cathode plume is compressed and axially elongated by the magnetic field at the center axis of the thruster. Thus, thruster plume becomes more axisymmetric, which reduces asymmetric erosion of discharge channel and may increase thruster lifetime. Also, increased symmetry increases the alignment of the thrust vector with thruster axis and contribute to the spacecraft integration.

In the studies conducted at JPL [54, 55] and Busek [56], BHT-8000, which is a 8 kW Hall thruster was investigated. The beam divergence decreases with internal cathode configuration. The studies of Sommerville *et al.* [57, 58] and Hofer *et al.* [54] have suggested that utilization of an external cathode magnifies the radial electric fields, especially when the cathode is placed outside of the separatrix. Magnified radial fields increase beam divergence and cause losses in efficiency and thrust.

According to the studies that are conducted by Tillet *et al.* on the BPT-4000 Hall thruster, higher thrust yields can be achieved with an axially aligned cathode, when placed closest to the discharge channel [59]. Also, EMI (electromagnetic interference) is reduced with the close positioned cathode [60]. Cathode coupling voltage is also decreased.

In the study of Diamant *et al.* on the BHT-1500 Hall thruster, it was observed that internal cathodes couple more efficiently with the plume [61]. So that, energy required to extract electrons from the cathode decreases, thus lower electron temperatures are obtained. With the decreased electron temperatures a decrease in plasma potential is observed, while electron density, thrust, I_{sp} and efficiency increase. BHT-1500 Hall thruster is operated at 300 V and 400 V at 1.5 kW power level for internal and external cathode configurations. Utilization of an internal cathode caused an increase of 5% in thrust, 6% in I_{sp} and 6% in efficiency.

Jameson *et al.* investigated the effect of the cathode configuration on a Hall thruster that is operated at 3 kW and 6 kW power levels [50, 62]. For both power levels an increment of about 2-3 % is achieved at efficiency and thrust.

A primary internal cathode is used in the UK90 Hall thruster design. With the internal cathode design, an increased efficiency, thrust, I_{sp} and a reduced beam divergence are aimed [63]. Also, an external cathode is added to the design as a redundancy. A photo of the developed hollow cathode is shown in Figure 3.3.

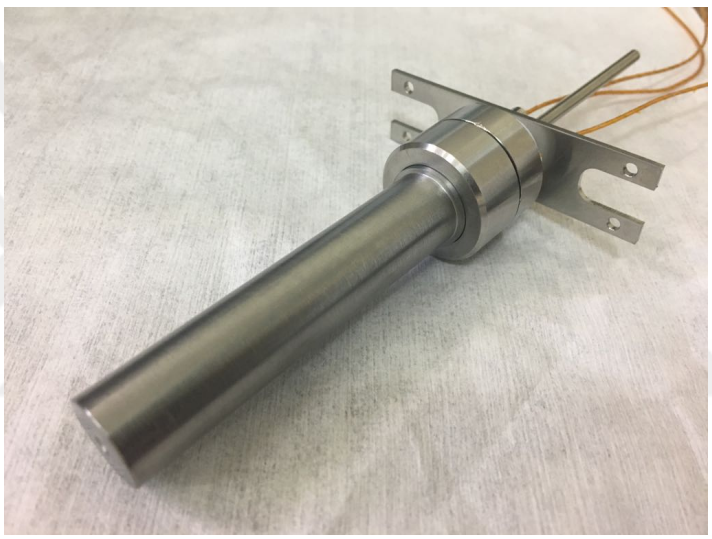

Figure 3.3. BUSTLab hollow cathode

3.2. Scaling of Hall Thruster

The UK90 Hall thruster design is developed according to several design constraints. These constraints include the dimensions of the internal hollow cathode and available discharge channel and magnetic circuit materials. The design parameters are determined according to these constraints. Main design parameters are: D channel outer diameter, w channel width and L channel length. Considering the design constraints, suitable power level of the Hall thruster is determined to be about 1.5 kW. Also, optimum operating discharge is determined to be about 300 V, and discharge current is about 5 A.

Design parameters are determined by using the scaling laws in the literature. Currently there are no complete analytical and numerical solutions for the Hall thruster performance, therefore empirical data are used in thruster designs [64]. The scaling laws are obtained from experimental results of SPT thrusters [6, 65, 66]

$$P_d \propto T \propto I_d \propto \dot{m} \propto D^2$$
$$w \propto D$$

where, P_d is discharge power, T is thrust, I_d is discharge current, $\dot{m}$ is mass flow rate and D is channel outer diameter. As channel width is linearly proportional to the channel diameter; power, thrust, discharge current and mass flow rate are linearly dependent on the channel exit area. Various thrusters are investigated to determine the design parameters of the new thruster. Parameters of the investigated thrusters are shown in Table 3.2.

Table 3.1. Operational parameters and dimensions of various Hall thrusters [26–32]

Parameters	SPT-20	HET-100	HK40	SPT-30	SPT-50	BHT-1000	SPT-100	UK90	Alta	SPT-140	P5	T-220	457M
Channel OD (D) (mm)	20	29	41	30	50	80	100	90	120	140	173	220	457
Channel Width (w) (mm)	5	5,5	6,2	6	11	12	11	16	20	20	25	32	128
Channel Length (L) (mm)	32	14,5	9,1	11	25	15	22	17	17	22	38	49	83
Br,max (G)	290	N/A	420	N/A	170	460	200	200	N/A	N/A	350	200	215
Vd (V)	200	300	260	250	350	450	300	300	340	400	500	495	500
Power (W)	100	174	250	258	250	1000	1350	1500	1930	5000	5000	10000	50000
w/L	0,16	0,38	0,68	0,55	0,44	0,80	0,50	0,94	1,18	0,91	0,66	0,65	1,54
w/D	0,25	0,19	0,15	0,20	0,22	0,15	0,11	0,18	0,17	0,14	0,14	0,15	0,28
ṁ (mg/s)	N/A	0,5	1	0.98	N/A	2,51	5,3	6,7	6,6	13,2	10,2	20,3	86,4
T (mN)	4	6,8	11	13,2	N/A	55	90	93	121	263	238	511	2314
Isp (s)	1400	1386	1772	1234	N/A	2051	1734	1405	1713	1929	2215	2389	2512
ηa	0,38	0,27	0,28	0,31	N/A	0,56	0,5	0,43	0,53	0,5	0,53	0,6	0,57

Channel dimensions are one of the most important parameters for operational characteristics of thruster. Ionization and acceleration occur close to the channel exit. Since the electrons are magnetized and trapped in the radial magnetic field as shown in Figure 3.4, channel length should be larger than the ionization mean free path to

achieve high mass utilization. Radial magnetic field near the anode should be very low to demagnetize the plasma near anode. By demagnetizing the plasma near the anode, the discharge voltage can be kept along the channel up to ionization region, thus voltage utilization is increased. Also, achieving a low electron temperature near the anode reduces heat flux to the anode and increases efficiency. A larger channel is required to obtain demagnetized plasma near anode. Usually, the propellant is injected into the channel through the anode, therefore channel length should be sufficient to obtain a regular propellant flow at the ionization and acceleration regions. Thus, asymmetries at thrust vector and mass utilization losses are decreased.

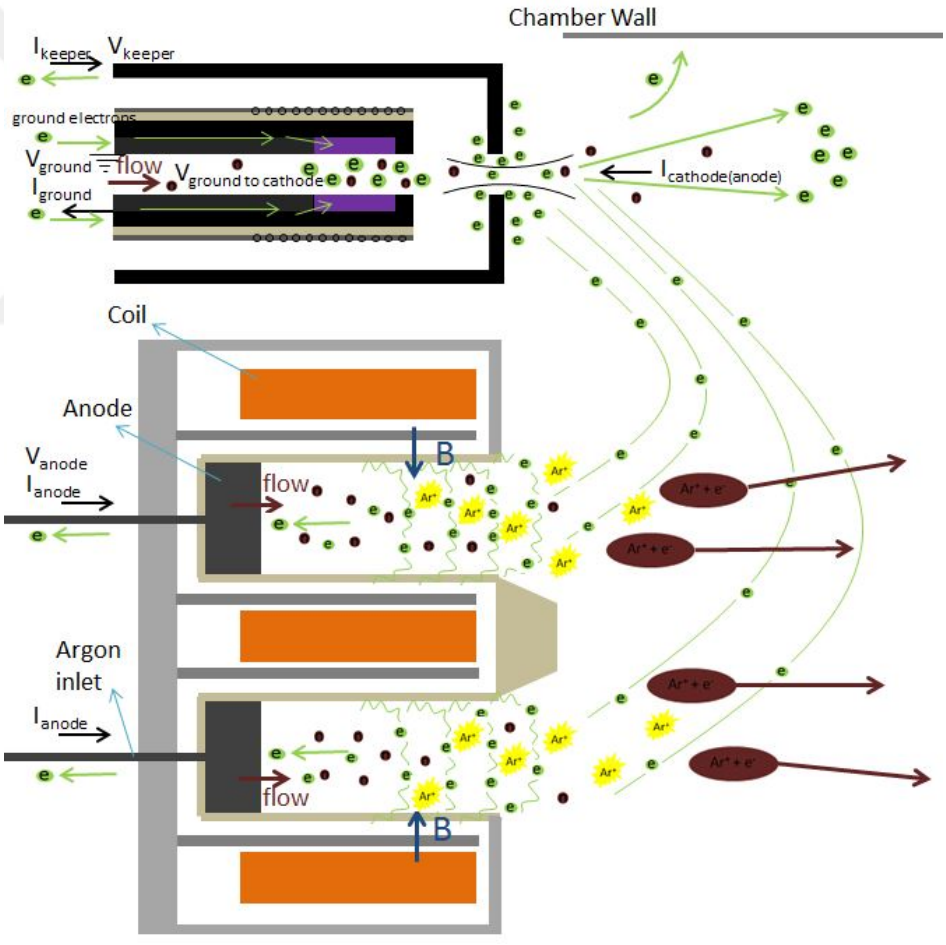

Figure 3.4. Hall thruster operation schematic [22]

Electrons are magnetized in the channel, while ions should not be magnetized, but accelerated and expelled from the channel, therefore Larmor radius of ions should be much larger than the channel length. This criterion can be easily satisfied, as the Larmor radius of the ions has very high values. However, increased channel length also increases the heat losses to the channel walls and causes efficiency losses. An optimum length should be obtained for optimum operation.

Radial dimensions are also critical for Hall thruster operation. Channel width should be significantly larger than the Larmor radius of the magnetized electrons. Also, as the channel width increases the surface to volume ratio of the plasma decreases, thus ion and electron fluxes to the channel walls are decreased. However, as the channel width increases, neutral and electron densities in the channel decrease, which reduces mass utilization of the propellant. Therefore, channel width and diameter are dependent on the power level of the thruster. According to the scaling laws, the dimensions of the Hall thruster is determined to be 90 mm for channel outer diameter, 16 mm for channel width and 17 mm for channel length. Operational parameters are determined with further scaling equations.

3.3. Theoretical Operational Characteristics

Thrust of the Hall thruster can be found as:

$$\mathbf{T} = \dot{m}_i \mathbf{v} \tag{3.1}$$

where, $\mathbf{T}$ is the thrust vector, $\dot{m}_i$ is ion mass flow rate and $\mathbf{v}$ is the average ion exhaust velocity. Total ionization of the propellant is assumed, thus anode mass flow rate is:

$$\dot{m}_a = \frac{I_d M_a}{e} \tag{3.2}$$

where, $\dot{m}_a$ is anode mass flow, I_d is discharge current, M_a is atomic mass of the propellant and e is elementary charge. Not all of the generated ions contribute to the beam and a portion of them collide with the channel walls. Therefore, ion mass flow is

$$\dot{m}_i = \frac{I_d M_a}{e}\eta_j \tag{3.3}$$

$$\eta_j = \frac{\dot{m}_i}{\dot{m}_a} = \frac{I_b}{I_d} \tag{3.4}$$

where $\dot{m}_i$ is ion beam mass flow, η_j is current efficiency, I_b is beam current. Ion velocity (v) can be found from the electrostatic acceleration. For simplicity doubly ionized particles are neglected here.

$$\frac{M_a v^2}{2} = eV_b\eta_{loss}\eta_\phi \tag{3.5}$$

$$\eta_v = \frac{V_b}{V_d} \tag{3.6}$$

$$v = \sqrt{\left(\frac{2eV_d\eta_{loss}\eta_\phi\eta_v}{M_a}\right)} \tag{3.7}$$

V_b is the beam acceleration voltage, V_d is the discharge voltage, η_v is the voltage utilization efficiency, η_{loss} is the total heat losses to the walls and anode, η_ϕ is the beam divergence loss [67]. By substituting Equation 3.3 and Equation 3.7 into Equation 3.1, thrust is found:

$$T = I_d \eta_j \sqrt{\frac{2 V_d M_a \eta_{loss} \eta_\phi \eta_v}{e}} \tag{3.8}$$

$$\eta_a = \eta_{loss} \eta_\phi \eta_v {\eta_j}^2 \tag{3.9}$$

$$T = I_d \sqrt{\frac{2 V_d M_a \eta_a}{e}} \tag{3.10}$$

$$\eta_a = \frac{T^2}{2 \dot{m}_a P_d} \tag{3.11}$$

where, η_a is the anode efficiency, which is the efficiency of the thruster without considering the cathode and magnet power. Specific impulse of the thruster is:

$$I_{sp} = \frac{T}{\dot{m} g} \tag{3.12}$$

$$I_{sp} = \frac{1}{g_0} \sqrt{\frac{2 V_d e \eta_a}{M_a}} \tag{3.13}$$

where, g_0 is the Earth's gravitational acceleration. It can be seen that specific impulse of the Hall thrusters increase with lighter propellants such as argon, however thrust increases with heavier propellants such as xenon. Total efficiency of the thruster can be found by adding the cathode and magnet effects [68]

$$\eta_T = \eta_a \eta_o \eta_c \tag{3.14}$$

$$\eta_0 = \frac{P_d}{P_T} \tag{3.15}$$

$$\eta_c = \frac{\dot{m}_a}{\dot{m}_T} \tag{3.16}$$

where, η_T is the total efficiency of the thruster, η_o is electrical utilization efficiency, which is the ratio of the discharge power to total power that includes keeper and magnet powers. η_c is the ratio of the anode mass flow to the total mass flow, which includes anode and cathode mass flows. Also, when Equation 3.10 and Equation 3.13 are combined, the trade off between thrust and I_{sp} at same power level can be seen:

$$TI_{sp} = \frac{2P_d\eta_a}{g_0} \tag{3.17}$$

Energy loss term η_{loss} in Equation 3.5 represents the amount of the energy that is lost due to the power deposited to the channel walls and anode, also ionization power usage [69]. Radiation losses are negligible.

$$\eta_{loss} = 1 - \eta_w - \eta_a - \eta_i \tag{3.18}$$

$$P_d = P_b + P_w + P_a + P_i \tag{3.19}$$

where, η_w, η_a and η_i are power fraction lost to walls, anode and ionization respectively, while P_w, P_a and P_i are the power loss to the walls, to the anode and ionization power respectively. P_b is the beam kinetic energy, which is:

$$P_b = V_b I_b = \frac{T^2}{2\dot{m}_a} \tag{3.20}$$

Ion flow to the channel walls is assumed to be about 10% of the beam current ($I_w = 0.1I_b$) [6, 70]. Also beam current can be found from Equation 3.4. Current efficiency value of SPT-100 is utilized, which is 0.81 [67]. As the discharge current of UK90 is 5 A, beam current is 4 A, while the wall current is 0.4 A.

Ionization cost can be defined as:

$$P_i = V_i \frac{I_b}{e} \tag{3.21}$$

where, V_i is the ionization energy of the propellant, which is 12.1 eV for xenon and 15.7 eV for argon. When xenon is utilized the ionization cost becomes 48 W, and with argon 63 W.

Heat loss to the anode can be found by using the formula [71]

$$P_a \approx 2T_{eV} I_d \tag{3.22}$$

Electron temperature (T_{eV}) at the anode wall is assumed to be about 5 eV [72]. So that anode heat flux is about 50 W.

Main heat loss mechanism is the ion and electron flux to the channel walls. Derivations of Goebel [6] is used for the wall heat flux calculations:

$$P_w = 45.8 I_w T_{eV} + 2.6 I_w T_{eV} \tag{3.23}$$

where, I_w is the ion flux to the walls, which is described previously as 10% of beam current. First term is the electron flux, and second term is the ion flux, which is an order of magnitude less than the electron flux. Electron temperature along the wall is assumed to be 25 eV [6]. With 5 A discharge current, ion heat flux is 26 W and electron heat flux is 458 W. Total heat flux to the channel walls is about 484 W.

Total heat loss to walls, anode and ionization cost are about 600 W, thus loss efficiency term η_{loss} is about 0.6. Efficiency terms of SPT-100 is used for anode efficiency calculation [67]. By adding divergence (0.95) , voltage efficiency (0.95) and mass utilization efficiency (0.81), the anode efficiency becomes 0.43. Thrust can be calculated by Equation 3.10 with 300 V discharge voltage and 5 A discharge current. For xenon propellant, calculated thrust is 93 mN with 1405 s I_{sp}. For argon propellant, calculated thrust is 51 mN with 2542 s I_{sp}. Cathode mass flow during operation will be around 0.1 of anode mass flow rate, therefore cathode efficiency (η_c) becomes 0.91. Electrical efficiency (η_0) is assumed to be 0.93. By using Equation 3.14, total efficiency of the Hall thruster is 0.36.

3.4. Magnetic Topology of Hall Thruster

Magnetic topology of the Hall thruster is crucial for its performance. A focusing symmetrical magnetic lens topology is desired at the channel exit [73,74]. According to the scaling laws, magnetic field strength at the channel exit is inversely proportional to the channel length and channel width. Thus, the magnetic flux density at the centerline of the channel exit is determined to be at least 200 G. Electrons are magnetized and trapped within the channel with the applied radial magnetic field. Larmor radius of the electrons can be found by using thermal velocity of electrons [6]:

$$r_e = \frac{v_{th}}{\omega_c} = \frac{m}{eB}\sqrt{\frac{8kT_e}{\pi m}} = \frac{1}{B}\sqrt{\frac{8m}{\pi e}T_{eV}} \tag{3.24}$$

where, r_e is the Larmor radius of the electrons, v_{th} is the electron thermal velocity and ω_c is the cyclotron frequency, m is electron mass, e is elementary charge, B is magnetic flux density, k is Boltzmann constant, T_e is electron temperature in Kelvin, and T_{eV} is electron temperature in eV.

According to Equation 3.24, the electron Larmor radius at an electron temperature of 25 eV [6], which is typical for Hall thrusters, and the determined radial magnetic field strength of 200 G is 0.8 mm. Larmor radius value is less than 10% of the channel width and length, which is required for optimum operation and ionization [72].

Several design criteria are considered during magnetic topology design, such as magnetic shielding, the magnetic field strength at the anode and magnetic saturation of magnetic circuit parts.

Channel walls of SPT type Hall thrusters are made of ceramic materials, such as BN (boron nitride) and alumina, which have low sputtering yields. As the wall material is not conductive, ion and electron currents to the walls should be equal, therefore large sheath potentials form at the ceramic walls. Sheath formation generates a radial electric field and accelerate ions to the walls. Ion bombardment to the channel walls causes erosion, which is the main life time limiting factor of Hall thrusters. Also, near the channel exit region, electrons spiral along the radial magnetic field lines and high energy electrons that can pass through the sheath potential bombard the channel walls [23]. As shown in Equation 3.23, the main efficiency loss factor of Hall thrusters is the high energy electron flux to the channel walls.

In order to reduce channel wall erosion and heat flux to the channel walls, magnetic shielding method is proposed by JPL after the investigations of BPT-4000 Hall thruster that is developed by Aerojet [75]. BPT-4000 Hall thruster has been operated for 10000 hours with very low erosion rates [76]. Magnetic shielding approach is then used at H6MS and HERMeS (Hall Effect Rocket with Magnetic Shielding) Hall thrusters that are developed at JPL and NASA Glenn Research Center [77–80].

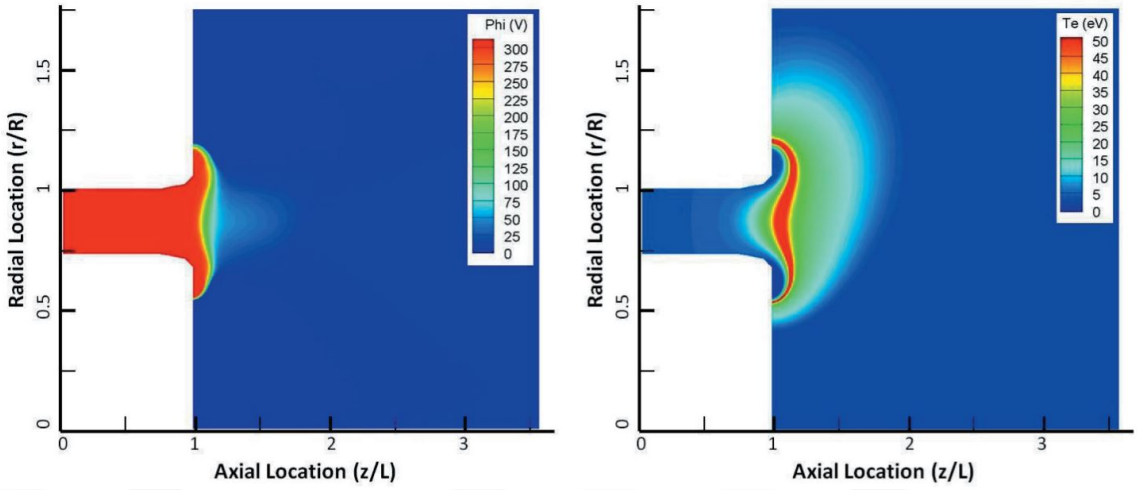

Figure 3.5. Numerical simulation results of a magnetically shielded thruster: Plasma potential is on the left and electron temperature is on the right [23]

In magnetic shielding design, the magnetic field lines do not intersect with channel walls, instead they are parallel to the channel walls. Magnetic field lines in the channel are isothermal, therefore electron temperature along a magnetic field line is homogeneous. The field lines that penetrate into the channel capture the cold electrons, which have temperature of about 5 eV, near the anode region. Cold electrons move along the field lines and are transported near to the channel walls (Figure 3.5). Sheath potential at the channel walls decreases because of the cold electrons, so that ion acceleration through the sheath potential to the walls and channel erosion are reduced. Also, as magnetic field lines do not intersect with the walls, high energy electrons do not flow into the walls and better confinement is achieved. Increased confinement of electrons within channel decreases power loss and increases efficiency and I_{sp} [23, 72, 81].

During the magnetic topology design of UK90 Hall thruster, a near magnetic shielding approach is aimed. Magnetic field lines that are parallel to the channel walls along most of the channel are used. As previously explained, a demagnetized plasma is desired to avoid voltage drop near the anode region and achieve high voltage utilization. Also, as shown in Equation 3.22, heat flux to the anode is proportional to electron temperature near the anode region. Therefore, weak magnetic field ($<$ 10

G) is preferred near anode. In some thrusters, trim coils that are placed behind the anode or near the outer pole are used to fine tune the magnetic topology and cancel out the radial magnetic field near the anode [29]. Also, additional ring magnets that are placed around the channel can be used to generate cusp fields around the channel walls [66].

With the second generation of SPT thrusters that are developed at Fakel in 1990s, magnetic shields have been started to be used in magnetic circuit of Hall thrusters. Magnetic shields are placed inside and outside of the channel walls, so that they pull the magnetic field lines from the channel region and screen the anode from the magnetic field. A small gap is left between the shields and pole parts, so that the magnetic field cusps can be formed around the shields and magnetic lens topology is compressed into a more concave structure. Increased concavity of the magnetic lens increases ion focusing to the channel centerline and decreases plume divergence [74].

As magnetic circuit material, Hiperco 50 is utilized. Hiperco is a cobalt-iron alloy and provides very high magnetic permeability and high magnetic saturation (2.4 T). High Curie temperature ($940°C$) enables safe operation at higher temperatures. Besides Hiperco, 1018 grade steel is also utilized in initial thruster prototypes.

3.5. Magnetic Modelling of Hall Thruster

In order to optimize the magnetic topology in the Hall thruster according to the design goals, a parametric analysis is conducted numerically. A 3D computational domain (Figure 3.6) and magnetic field module of COMSOL are used. As the magnetic field in the magnetic core materials reaches high values, magnetic saturation may occur in the material. Therefore, a non-linear magnetic model is utilized by using B-H curve for the magnetic circuit materials.

Preliminary magnetic circuit design is determined through several design iterations. After the determination of initial design, final design parameters were determined through optimization. Several effective design parameters are investigated during the

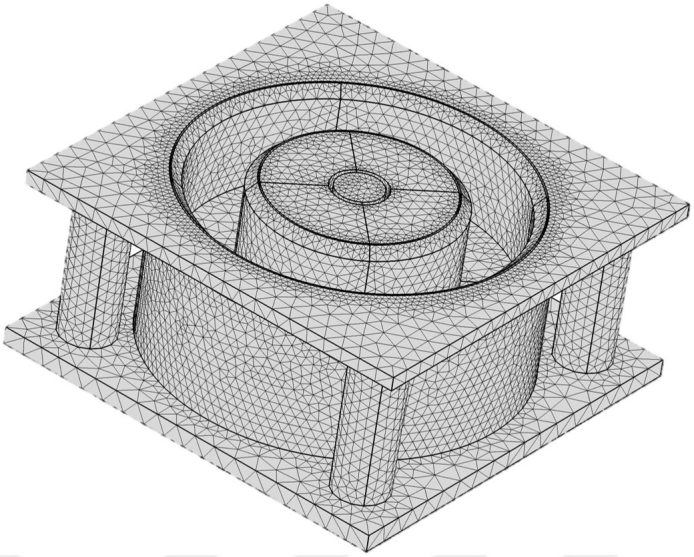

Figure 3.6. 3D mesh grid of Hall thruster

optimization. These parameters are magnetic pole thickness, magnetic shield thickness, gap between the shields and discharge channel walls, gap between the shields and magnetic poles as shown in Figure 3.7. Also the effect of the channel width is investigated. Three different parameters are shown for each case. All magnetic field strength values are in Gauss in the figures. Boron nitride discharge channel is designed with a chamfer at the channel exit in initial designs, so that the perpendicular crossing between the magnetic field lines and channel walls is reduced.

The channel width values are varied as 12, 16 and 20 mm as shown in Figure 3.8. As the gap between the magnetic poles increases, the magnetic field strength in the channel exit decreases, therefore necessary coil current increases. However, larger anode gap enlarges the magnetic cusps between the poles and shield parts. These magnetic cusps confine the magnetic lens structure within the channel exit better, so that magnetic field lines intersect with BN channel walls less. This magnetic topology with magnetic cusps prevents high electron temperature near the channel walls and decreases the ion loss to the channel walls, therefore provides magnetically shielded walls [72]. As the ion loss to the walls decreases, less power loss is observed to the channel walls as heat and also channel wall erosion decrease.

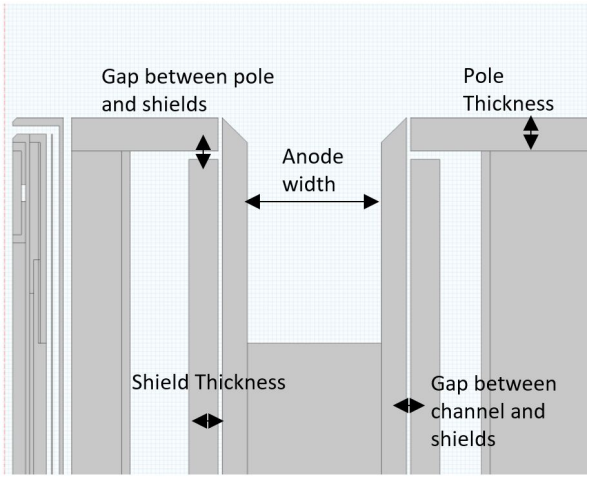

Figure 3.7. Thruster magnetic model design parameters

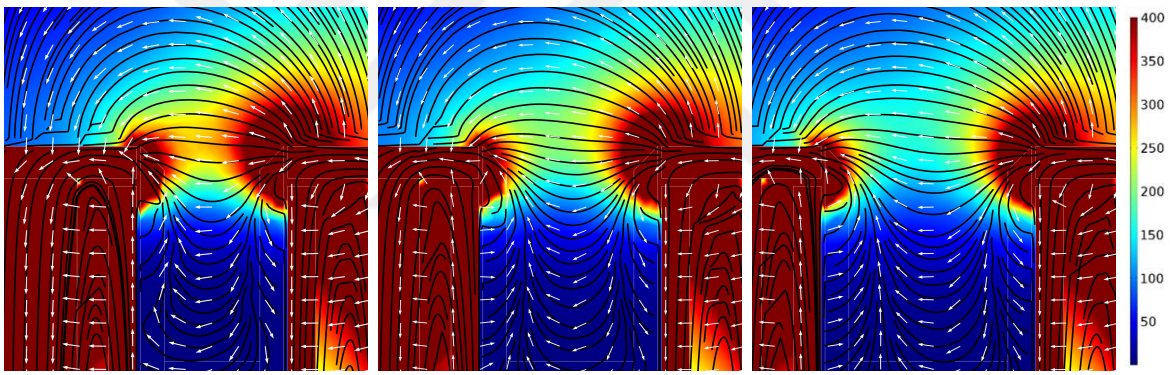

Figure 3.8. Parametric sweep channel width, a) 12 mm, b) 16 mm, c) 20 mm

In Figure 3.9, the analyses of the effect of the magnetic pole thickness are shown. The evaluated values are 2, 4 and 6 mm. Thickness of the poles affects the position of the magnetic cusps and the location of the maximum magnetic field. As the thickness increases, the cusps and the position of the point of maximum magnetic field move into the channel, therefore ion and electron losses to the walls increase. The minimum possible thickness value is selected without risking magnetic saturation within the pole parts.

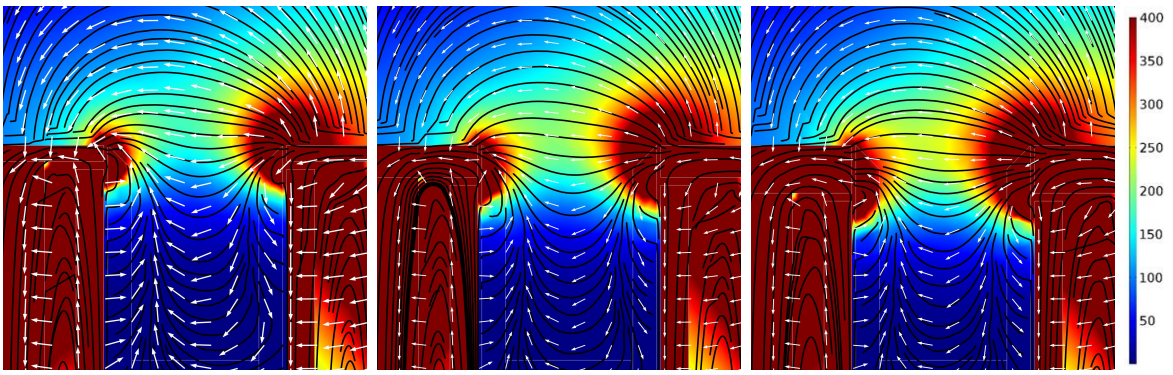

Figure 3.9. Parametric sweep of magnetic pole thickness, a) 2 mm, b) 4 mm, c) 6 mm

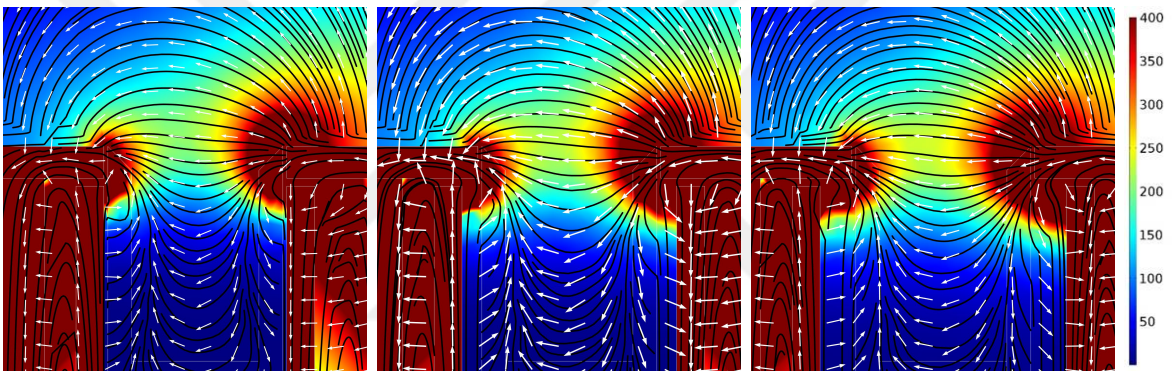

Figure 3.10. Parametric sweep of the gap between magnetic shields and BN channel, a) 0.5 mm, b) 2.5 mm, c) 4.5 mm

The position and the dimension of the magnetic shields are investigated. Thin magnetic shields cause higher magnetic field strength at the anode region (Figure 3.12), which may cause higher electron temperature near the anode region and increases heat loss to the anode. Smaller gap distance between the shields and pole parts keeps the cusp lines closer to the channel exit and decreases the intersection between the magnetic lens lines and channel walls as shown in Figure 3.11. Also, as the gap between the shields and BN channel part decreases, the cusps move into the channel and compress the lens structure (Figure 3.10). The optimized magnetic topology is shown in Figure 3.13 a. The magnetic field strength along the inner and outer sides, and at the middle of the discharge channel is shown in Figure 3.13 b. Maximum magnetic flux density is obtained a few millimeters outside the channel exit, hence the channel walls are

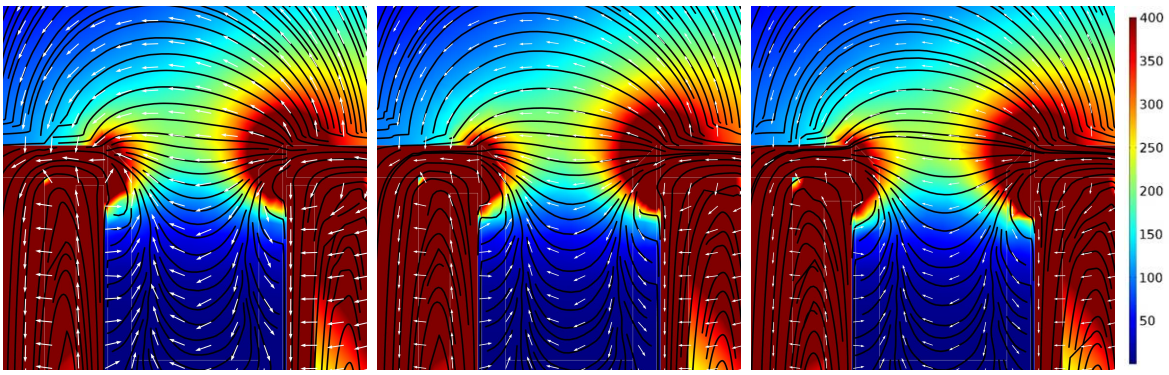

Figure 3.11. Parametric sweep of the gap between magnetic shields and poles, a) 1 mm, b) 2 mm, c) 3 mm

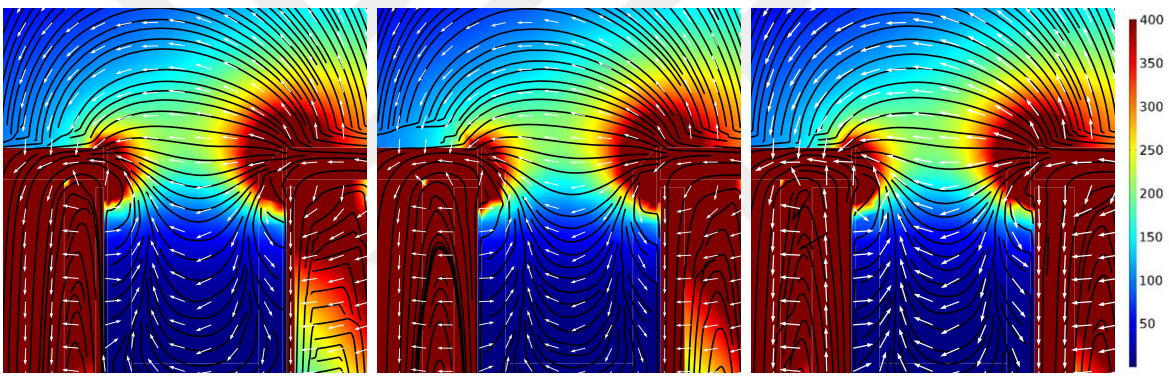

Figure 3.12. Parametric sweep of magnetic shield thickness, a) 1 mm, b) 3 mm, c) 5 mm

protected from the energetic particles and wall erosion is reduced.

3.6. BUSTLab Hollow Cathode

The hollow cathode that is developed at BUSTLab is utilized in UK90 Hall thruster [24, 82]. The hollow cathode generates electrons through thermionic emission process. As emitter material lanthanum hexaboride (LaB_6) is utilized, which has a work function of about 2.67 eV. When heated to high temperatures, LaB_6 emits electrons [83–89]. LaB_6 emitters are resistant to impurities and provide longer lifetime than materials such as barium-oxide impregnated tungsten (BaO-W) [90,91]. Emission

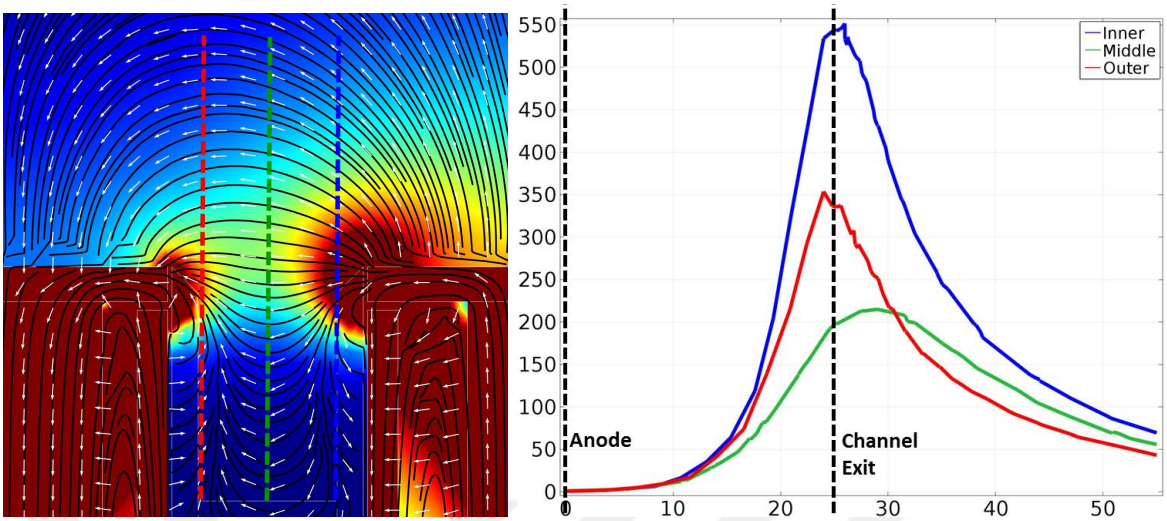

Figure 3.13. a) Optimized magnetic topology in discharge channel, b) Magnetic flux density (G) along the discharge channel in axial direction

current density of an emitter material can be calculated from the Richardson-Dushman equation

$$j = AT_w{}^2 e^{e\frac{e\phi}{kT_w}} \tag{3.25}$$

where, j is the emission current density, T_w is the emitter material wall temperature, ϕ is work function in eV, and k is Boltzmann constant [92]. According to Richardson-Dushman equation, emission current densities for BaO-W and LaB_6 at different temperatures are shown in Figure 3.14.

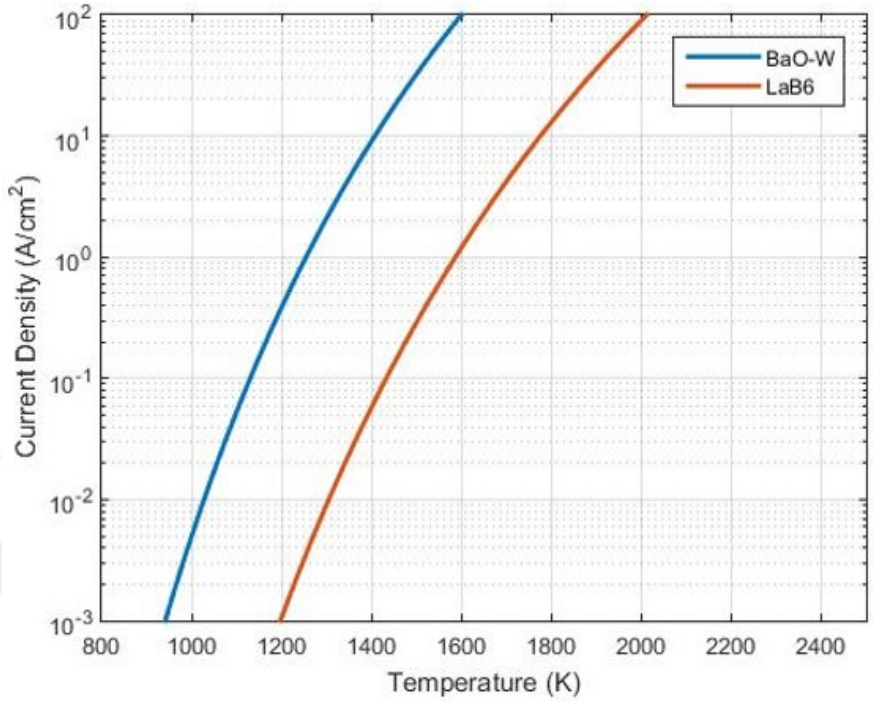

Figure 3.14. Emission current densities of BaO-W and LaB_6 vs. temperature [24]

Required cathode discharge current is about 5 A. Considering the cathode dimensions, the required emission current density is around 15 A/cm2. As seen in the Figure 3.14, required temperature is higher than 1100 °C with BaO-W emitter, however LaB_6 emitters require temperatures higher than 1500 °C. In BUSTLab hollow cathode, a LaB_6 tube with 2 mm inner diameter, 4 mm outer diameter and 10 mm length is used. Emitter tube is placed within a conductive cathode tube as shown in Figure 3.15. Cathode tube is covered with a heater assembly, which consists of insulator ceramic parts and a heater coil. Tantalum wire is used as the heater coil. During the initiation of cathode operation, a current is applied to the heater wire. Above the required temperatures, emitter material emits enough electrons to ionize the neutral gas that flows in the cathode tube, thus a quasi-neutral plasma is generated within the cathode tube. Formation of the plasma generates a sheath at the emitter surface, so that electron emission is enhanced and ions are accelerated towards the emitter surface. Ion collisions with the emitter walls provide a self heating mechanism to the cathode. A positive voltage is applied to the keeper tube that covers the cathode tube.

Electrons are extracted from the plasma to the keeper tube with the applied voltage. Plasma voltage within the cathode tube arranges itself according to the electron flow, thus self heating mechanism is sustained [93].

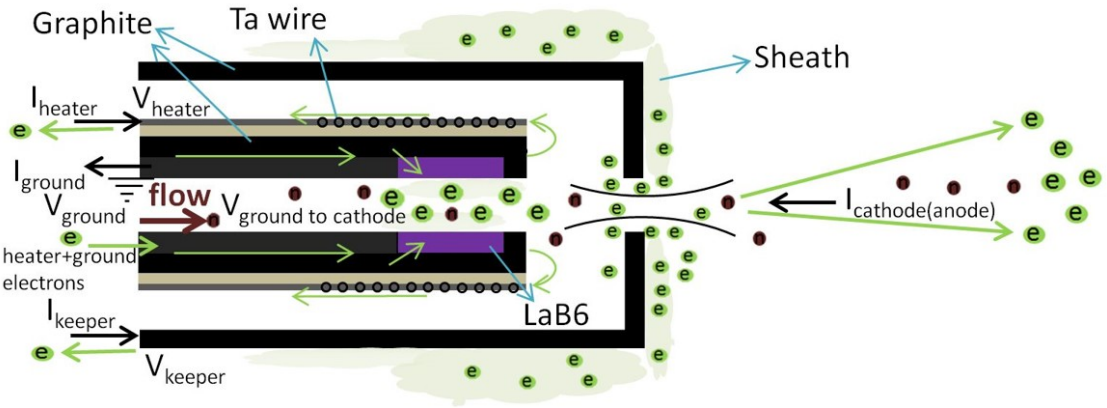

Figure 3.15. A schematic of cathode operation mechanism

Several heater designs are developed and tested at BUSTLab [94]. Numerical analyses of these designs are conducted using COMSOL Multiphysics. As computational domain, 2D axisymmetric domains are used as shown in Figure 3.16.

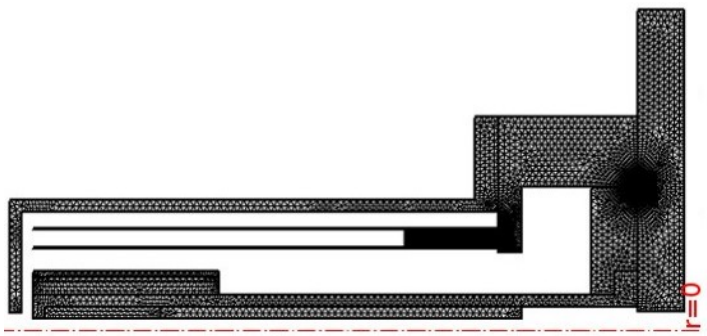

Figure 3.16. Mesh grid of the axisymmetric 2D computational domain of cathode

Temperature and heat flux distributions are investigated by conducting thermal analyses. Necessary heater power inputs are applied at each case, so that inner surface of the emitter material is kept at 1500 °C, which is required for the initiation of the thermionic emission. Thermal conductivity of the cathode components vary with temperature. Surface emissivity and thermal conductivity values of the cathode components are shown in Figure 3.17.

Materials	Emissivity	Thermal Conductivity at 300 K [W/(m K)]	Thermal Conductivity at 1700 K [W/(m K)]
Graphite	0.7	96.25	38.38
Alumina	0.9	36.96	6.53
Tantalum	0.2	57.4	62.97
Molybdenum	0.1	138.32	94.3
Shapal	0.83	94.39	65.08
Macor	0.87	1.44	3.54

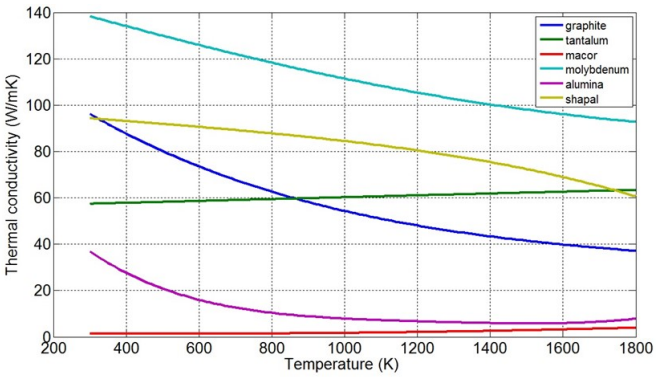

Figure 3.17. Thermal conductivity and surface emissivity of cathode materials [25]

Temperature distributions and heat fluxes within the cathode for different heater designs are shown in Figure 3.18. As the cathode is operated in high vacuum environment, convective heat transfer is negligible. Dominant heat transfer mechanisms are the conductive heat transfer through the cathode tube and radiative heat transfer. Conductive heat transfer is reduced with insulator ceramic parts. Also, radiative heat transfer is reduced with reflective shields.

According to the thermal analysis, the main heat loss mechanism from the hollow cathode is the radiative heat transfer from the keeper surface; therefore radiative shields are essential for hollow cathode operation. In Figure 3.19a, radiosity values of the cathode surfaces for different shield designs are shown. In initial design, two concentric tantalum shields are used. In second design, molybdenum radiative shields are used. As the surface emissivity of molybdenum is lower than tantalum, a better radiative shielding is achieved and the required input power decreases. In both designs a significant percentage of the radiative heat transfer occurs between the upper surface

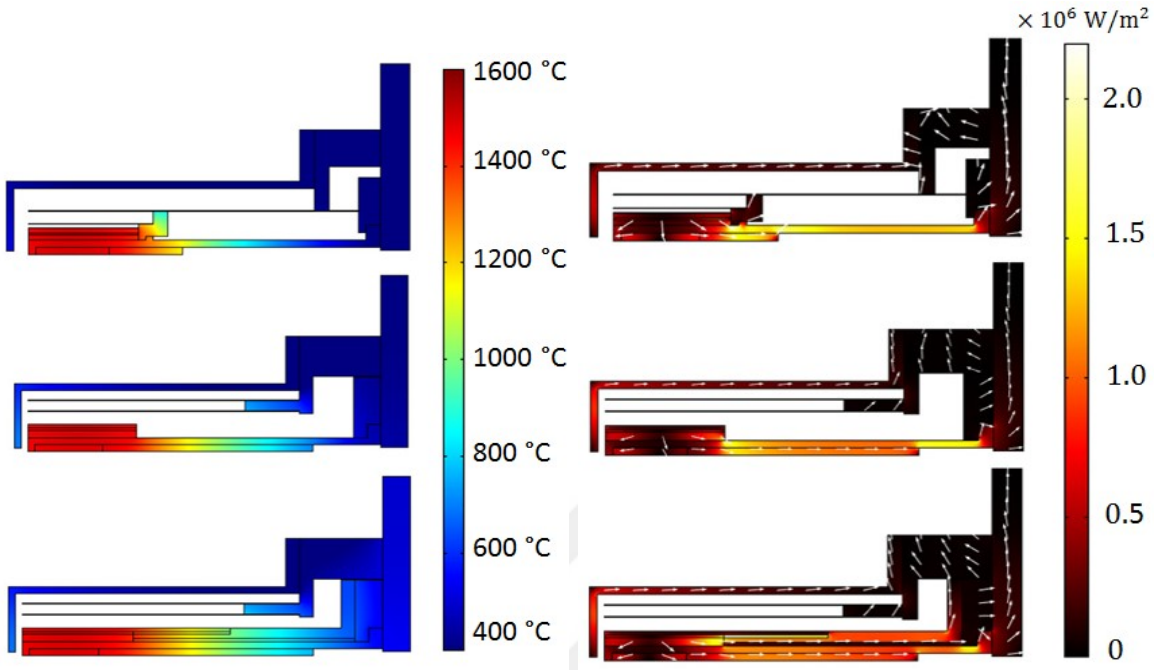

Figure 3.18. a) Temperature distribution in the cathode, b) Heat flux in the cathode

of the ceramic cover of the heater and the inner surface of the keeper. In third design, the ceramic cover part is partially covered with a molybdenum shroud, which further reduces the required heater power. Also, utilization of highly reflective metals such as molybdenum at keeper reduces the radiative heat transfer significantly.

In order to initiate the self-heating mechanism, quasi-neutral plasma has to be generated within the insert region. This plasma is sustained by the electron flow from the emitter surface and the electron extraction from the plasma through the orifice channel. For the electron extraction from the insert plasma, an outer electrical potential has to be applied. Therefore, a voltage that is higher than the plasma voltage is applied to the keeper. The orifice region has to be designed in a way, so that the keeper voltage can reach the insert plasma. In Figure 3.19b, the electrical potential around the orifice region before the plasma initiation is shown. Utilization of chamfers at the orifice edges may increase voltage penetration to the plasma inside the cathode tube.

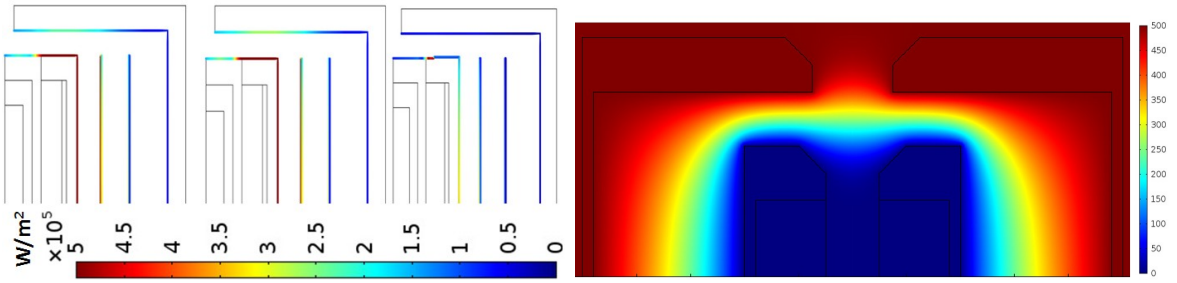

Figure 3.19. a) Radiosity of cathode inner surfaces, b) Electrical potential distribution (V) in the orifice region of the cathode

3.7. Thermal Modelling of Hall Thruster

Thermal management is critical for Hall thruster operation. Permeability of the magnetic parts decreases with increasing temperature. Above the Curie temperature magnetization vanishes. Also, in order to protect insulated wires at the electromagnets, temperatures have to be kept at safe values. There are three main heat sources: internal cathode, magnetic coils and plasma that is generated near the channel exit. This heat has to be extracted from the thruster primarily via radiative heat transfer, so that heat flux to the satellite can also be kept at low values.

Thermal analysis of the Hall thruster is conducted using COMSOL Multiphysics. An axisymmetric computational domain, which is shown in Figure 3.20.

Heat fluxes to the anode and channel walls that are calculated in Section 3.3 are used in thermal analysis. Heat flux to the anode is 50 W, and heat flux to the channel walls is about 484 W. Heat generation within coils is evaluated to be 30 W. Temperature at the inner surface of the emitter material of the cathode is 1500 $°C$. Ambient temperature is at room temperature during the analysis. The only heat loss mechanism from thruster is radiative heat transfer in the analysis.

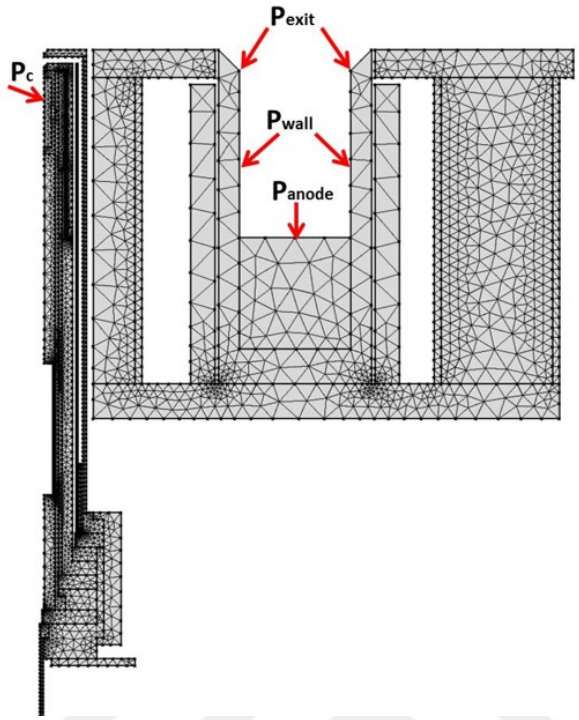

Figure 3.20. Mesh grid of thermal analysis and heat inputs

Several different thermal designs are investigated. Cathode is one of the main heat sources. Internal placement of the cathode may cause overheating of the inner coil assembly. Therefore, an additional molybdenum reflector is placed between inner core and cathode. Reflector is thermally and electrically insulated from the thruster body with ceramic parts. Inner coil is the most sensitive part of the thruster, as it is heated with the cathode and also with the discharge channel. In order to protect the inner coil from possible overheating, a bare copper wire is used at the coil. The wire is wrapped around the grooves of a ceramic cylinder. In order to avoid unwinding of the coil wire, quartz rods are placed between the coil wire and inner shield.

Main heat source of the thruster is the plasma inside the discharge channel. According to the analysis (Figure 3.21), channel temperatures increase to high values during operation. This heat has to be extracted without heating rest of the thruster. Therefore, utilization of a radiator is proposed. In this design channel assembly is thermally insulated from the magnetic circuit assembly. Discharge channel is mounted

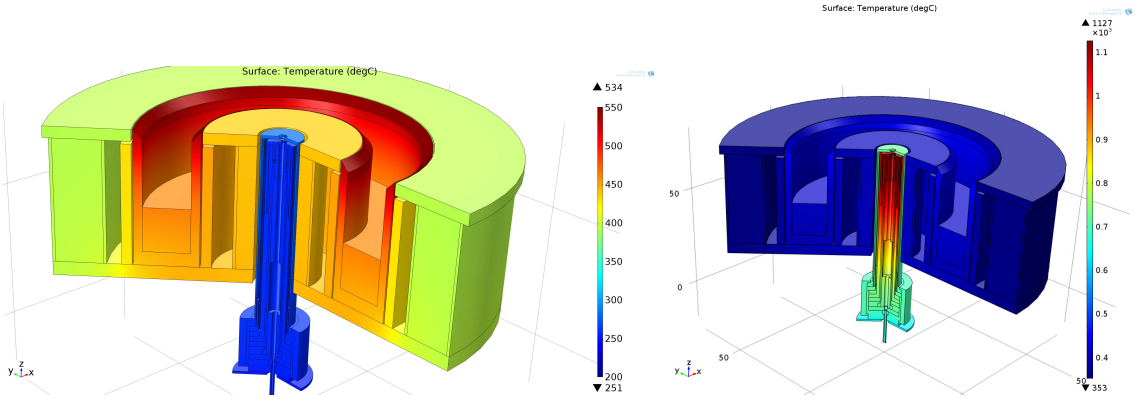

Figure 3.21. Thermal analysis of thruster: a) Without cathode power, b) With cathode power

on a copper heat sink and a copper thermal way is constructed through the holes in the magnetic backplate. A copper radiator, which has an anodized surface to increase surface emissivity, is attached to the copper heat sink assembly (Figure 3.22). The heat that is transmitted to the discharge channel flows through the copper heat sink to the radiator and then radiated away from the thruster (Figure 3.23). This way temperature of the discharge channel can be kept at respectively low levels. According to the magnetic analysis, the holes in the magnetic backplate do not harm the magnetic topology of the thruster. Thickness of the backplate is adjusted to avoid magnetic saturation that may be caused by the reduced section area.

An alternative solution was to use openings on the outer shield. Excessive heat of the discharge channel can be radiated away through these windows. However, it was seen that in the magnetic field analysis, these openings at the outer shield affect the magnetic topology and increase the magnetic field at the anode region. Therefore, no openings are used at the outer shield, however this problem may be avoided with the utilization of trim coils. Utilization of micro heat pipes are also considered and may be used in future designs. In order to increase radiation cooling, outer surfaces of the thruster is coated with boron nitride coating. As boron nitride has higher emissivity than iron parts, thermal management of the thruster is enhanced and lower temperatures can be achieved.

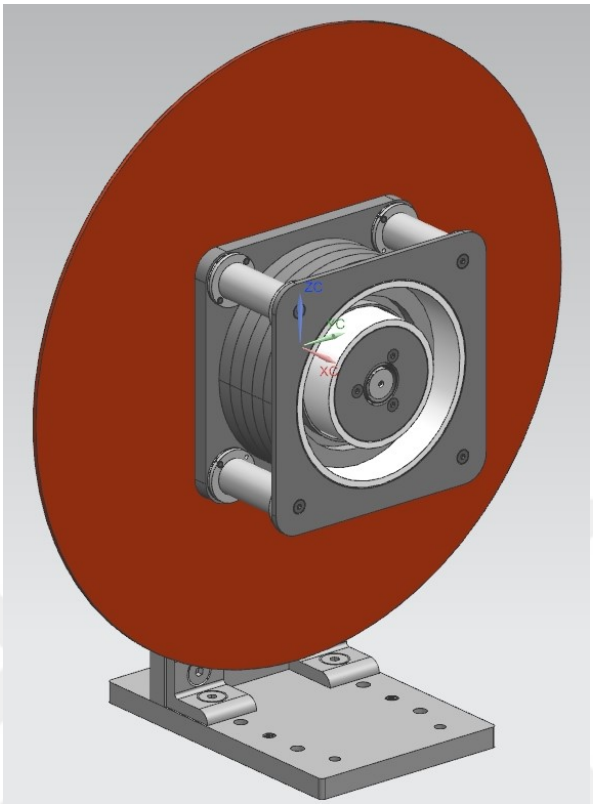

Figure 3.22. 3D drawing of Hall thruster with radiator plate

3.8. UK90 Hall Thruster Design and Manufacture

A modular design is applied for the Hall thruster. The Hall thruster consists of several subassemblies. These subassemblies are magnetic circuit, discharge channel, thermal system and support structure. Complete 3D drawing of the Hall thruster is shown in Figure 3.24.

The magnetic circuit consists of a backplate, one inner and four outer cores for electromagnets, inner and outer shields, and inner and outer pole parts. Magnetic circuit assembly is shown in Figure 3.25. Outer coil wires are wrapped around aluminium spools. These spools are thermally insulated from the backplate and pole parts with ceramic Macor rings at both end. Inner coil structure has been explained in section 3.7, and also is shown in Figure 3.26b. A bare copper wire is wrapped around a ceramic cylinder with grooves. Electrical connections of the wire are provided through

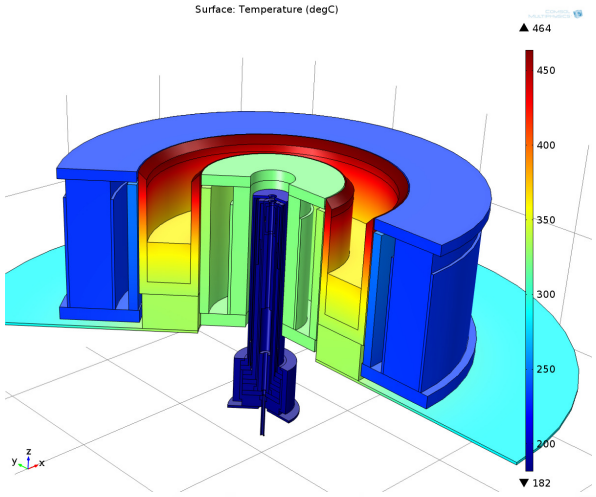

Figure 3.23. Thermal analysis of thruster with radiator

the holes in the backplate. These connections are insulated from the backplate with quartz tubes. Tightness of the coil is provided with alumina tubes that are squeezed between the inner magnetic shied and ceramic cylinder. Thus, a very high temperature resistant electromagnet is obtained in a very small gap.

Discharge channel is designed as a monolithic boron nitride part. Anode is placed inside the boron nitride channel. Two ring shaped parts are welded together with laser welding to build the anode, so that a hollow gas distributor channel is obtained. Propellant is injected into the channel in radial direction through small injection holes on the anode, thus higher pressures can be achieved in the discharge channel. A high voltage ceramic brake is welded to the anode for propellant feed. Three screws are welded also to the anode that are fastened to the support structure as shown in Figure 3.26a. Ceramic brake and screws are wrapped with ceramic tubes for electrical insulation. The screws are mounted on ceramic parts that are placed between the nuts and backplate. In order to avoid arcing between nuts, further electrical insulation is achieved with vacuum grade epoxy.

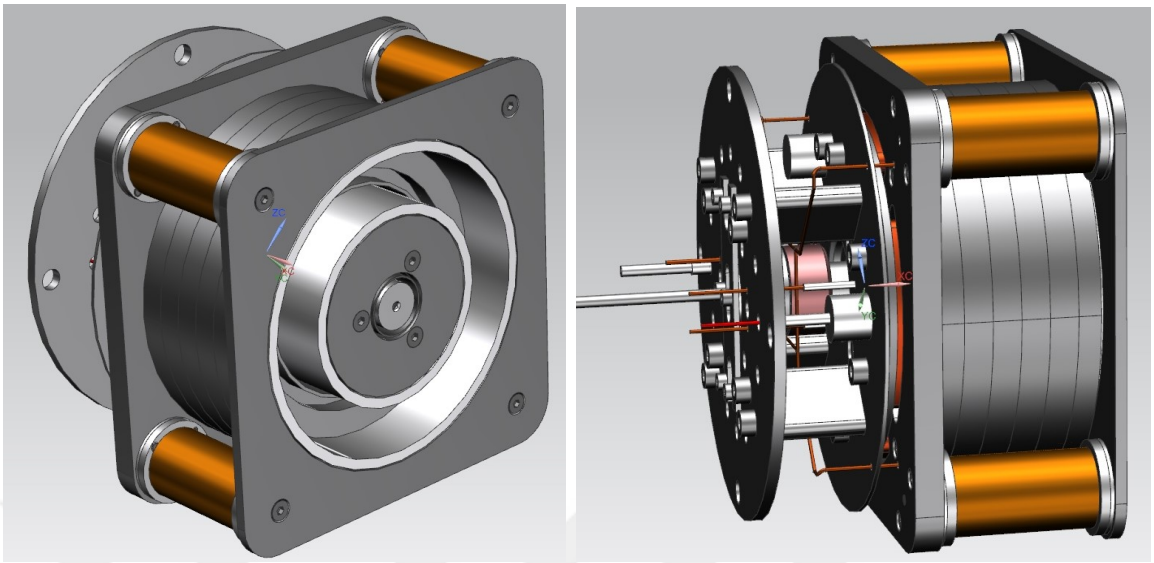

Figure 3.24. 3D drawings of Hall thruster

Boron nitride channel and anode is mounted on the copper thermal passive cooling structure as explained in section 3.7. Boron nitride channel is mounted on a copper disk, which is supported with four arc shaped copper parts that are placed in the gaps of the backplate. These gaps can be seen in Figure 3.25. These copper plates are mounted on another copper disk, which is attached to the copper radiator. Thermal contact between the thermal structure and other parts are minimized, so that heat transfer from the heat generating elements to other parts of the thruster can be kept at very low levels.

Support structure consists of two steel discs and four aluminium separators, which can be seen in Figure 3.27. Thermal structure, anode parts and magnetic circuit are attached to the front disc. Insulation of the anode screws and nuts is achieved with epoxy, and also electrical connection of electromagnets are performed between the discs of support structure. Cathode is attached to the rear disc. In order to reduce the radiative heat transfer from the cathode to the magnetic circuit, a radiator tube is attached to the front disc and isolated with ceramic parts. All cable and propellant line connections of the thruster are achieved through the backplate of the support structure. Completed assembly of the Hall thruster is shown in Figure 3.28.

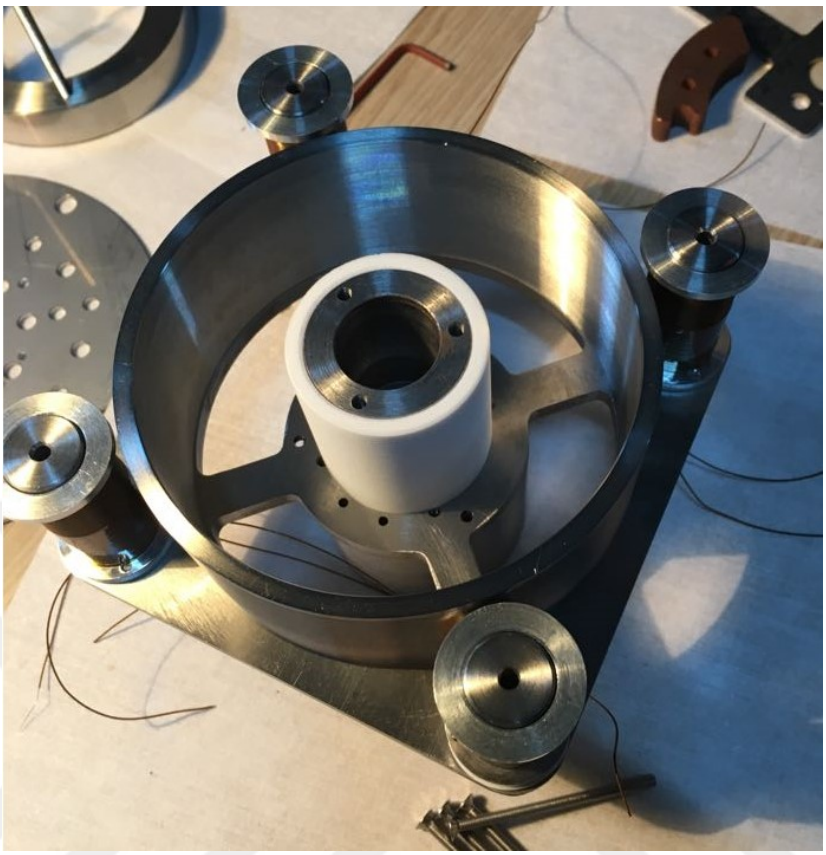

Figure 3.25. Magnetic circuit assembly with inner ceramic spool

Magnetic flux density measurements of the Hall thruster are conducted by using a Lakeshore DSP 455 Gaussmeter. The Gaussmeter utilizes a transverse Hall probe. The Hall probe is positioned at the center of the discharge channel exit, where the magnetic field is strongest. Radial magnetic flux density is measured (Figure 3.29). Magnetic flux density is measured for different inner and outer coil currents. Outer coils are connected in series with thin high temperature resistant electromagnet wires. Inner coil is a bare thick copper wire, as very high temperatures are expected at inner coil region. Therefore, higher coil current is applied to the inner coil, which has much lower resistance. In Figure 3.30, magnetic flux densities for different coil currents are shown. During thruster operation 200 G flux density is applied to the discharge channel exit. As can be seen in the measurements, magnetic circuit of the Hall thruster does not saturate at the desired discharge channel magnetic field strength.

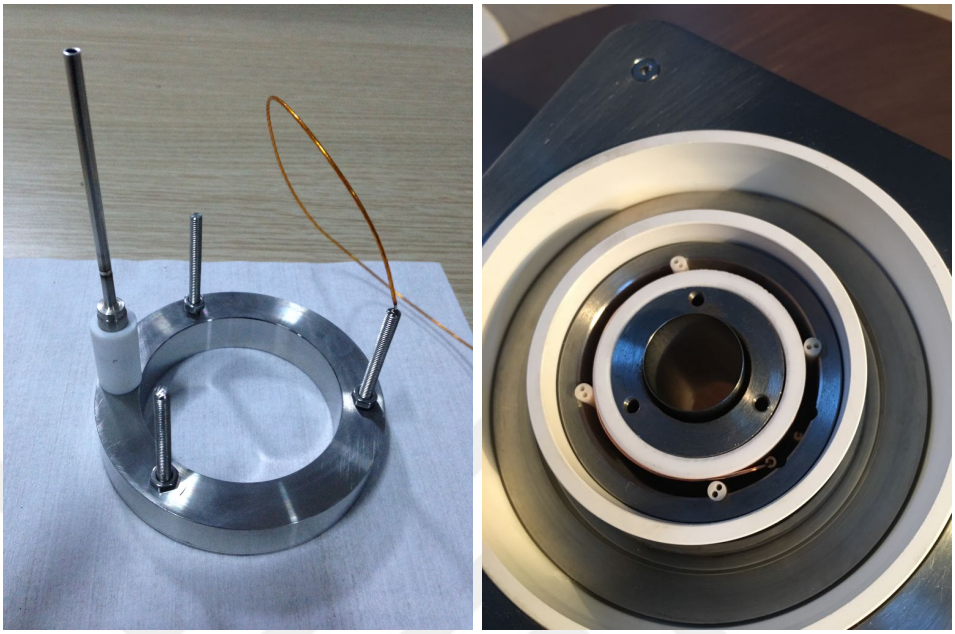

Figure 3.26. a) Anode assembly, b) Anode mounted inside discharge channel

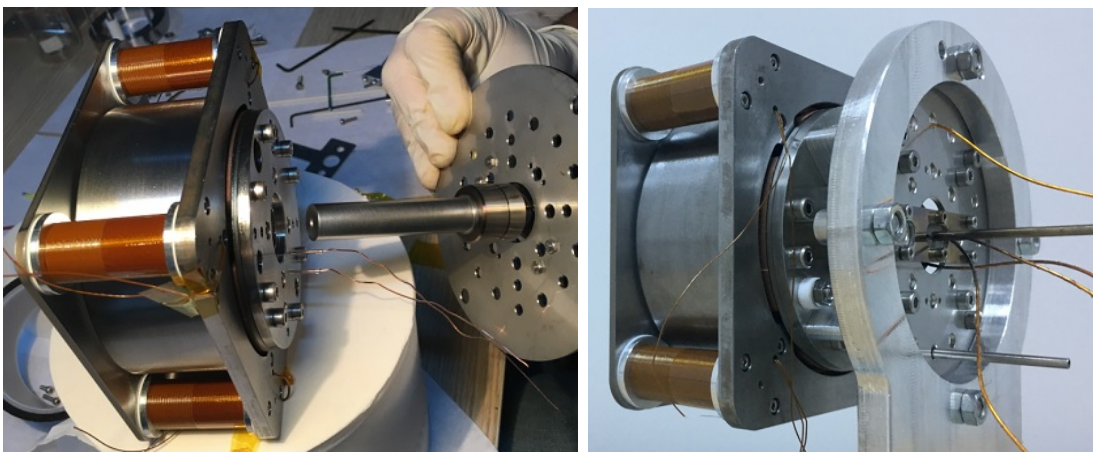

Figure 3.27. a) Mounting of support backplate and cathode, b) Cabling of Hall thruster

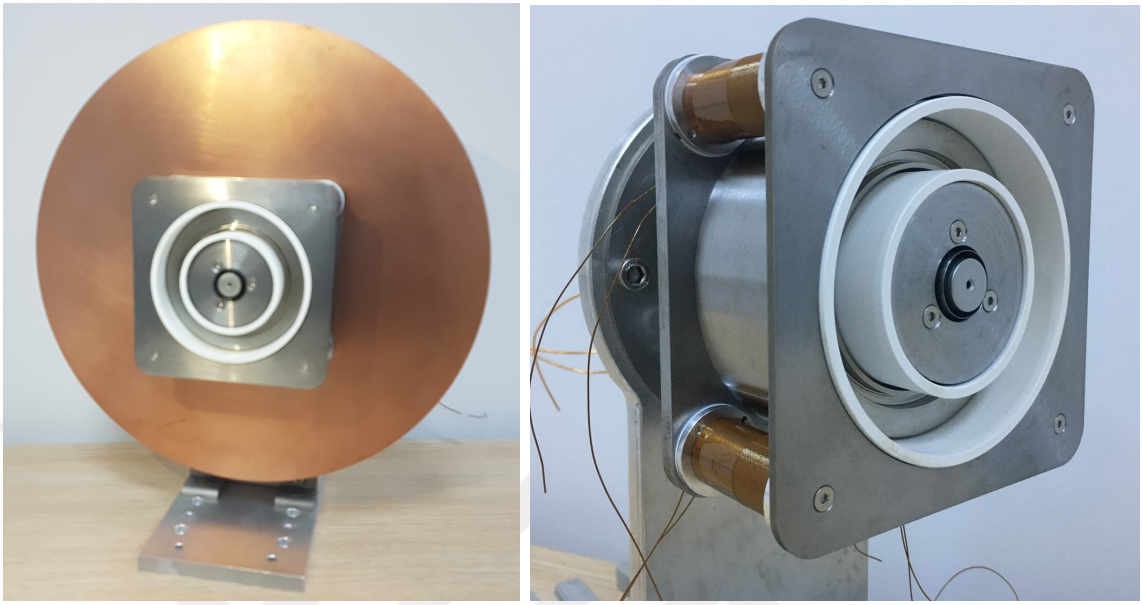

Figure 3.28. Completed assembly of Hall thruster with radiator (left) and without radiator (right)

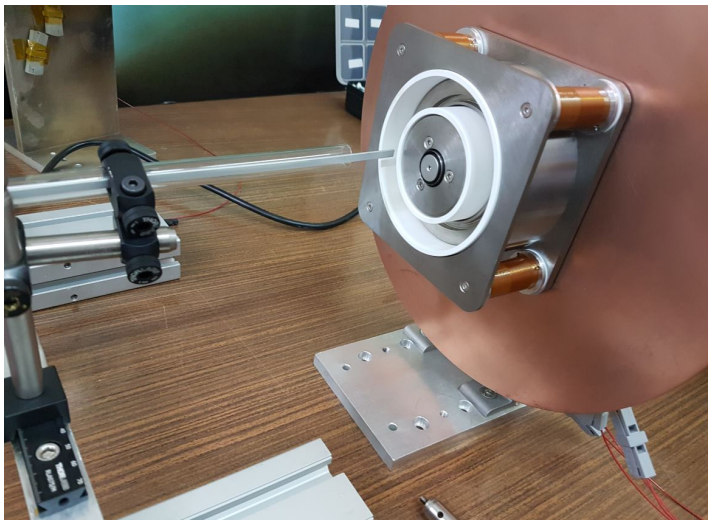

Figure 3.29. Magnetic field measurements with Gaussmeter

Inner Coil Current (A)	Outer Coil Current (A)	Inner Coil Power (W)	Outer Coil Power (W)	Magnetic Field Strength (G)
2,0	2,0	2,4	54,8	74
3,0	2,0	3,6	55,0	84
4,0	2,0	6,4	56,0	97
5,0	2,0	10,0	56,6	108
5,0	2,5	10,0	97,0	122
5,0	3,0	10,0	147,3	122
6,0	2,0	21,6	57,4	115
7,0	2,0	30,1	57,8	125
8,0	2,0	40,0	58,8	135
9,0	2,0	52,2	59,0	145
10,0	2,0	66,0	59,4	155
10,0	2,5	66,0	96,8	167
10,0	3,0	68,0	150,0	178
11,0	3,0	83,6	155,4	187
12,0	3,0	102,0	158,4	196
12,5	3,0	117,5	162,6	200
10,0	0,0	77,0	0,0	121
12,5	0,0	120,0	0,0	141
0,0	3,0	0,0	152,4	81

Figure 3.30. Magnetic flux density (Gauss) at the discharge channel exit for different coil currents

4. EXPERIMENTS AND RESULTS

4.1. Experimental Setup

As explained in Section 2.1, thrust measurements of electric propulsion systems are conducted in BUSTLab vacuum chamber. The vacuum chamber is 1.5 m in diameter and 2.7 m in length [44, 51]. The vacuum chamber is shown in Figure 4.1.



Figure 4.1. BUSTLab vacuum chamber

The vacuum chamber was manufactured by Kurt J. Lesker Company. One mechanical and two cryogenic pumps are utilized. The rough pumping is performed by using an Oerlikon rotary vane pump with roots blower that have a pumping capacity of 253 m^3/h. By using the mechanical pump, pressure inside the vacuum chamber is decreased to below 5×10^{-3} *Torr*. After completing the rough pumping step, pressure is reduced to 10^{-7} *Torr* level by using two 12-inch Sumimoto Marathon CP-12

cryopumps. Each cryopump has 3100 l/s argon pumping capacity. The cryopumps are cooled with two water cooled Sumimoto F-70H helium compressors. An air cooled chiller with a cooling capacity of 16.8 kW provides cold water to the compressors. An MKS Instruments 900 Series pressure sensor is utilized for pressure measurement. Propellants are supplied to the vacuum chamber through gas feedthroughs and propellant flows are controlled with MKS systems mass flow controllers. Swagelok valves and fittings are used at the propellant delivery lines.

Performance characteristics of the thrusters that are developed at BUSTLab are investigated.

4.2. HK40 Hall Thruster

HK40 Hall thruster is an SPT type Hall thruster with a channel diameter of 40 mm [22,46,63,95]. It utilizes four outer and an inner magnetic coils. Magnetic circuit is built with 1018 low carbon steel parts. Discharge channel is made of boron nitride and a 304 stainless steel anode is used. Hall thruster is operated with the hollow cathode that is also developed at BUSTLab (Figure 4.2). The hollow cathode that is used in HK40 tests utilizes a LaB_6 insert with 2 mm ID, 4 mm OD and 10 mm length [24,82]. A graphite keeper part is used. In Figure 4.3, HK40 Hall thruster is shown during measurements.

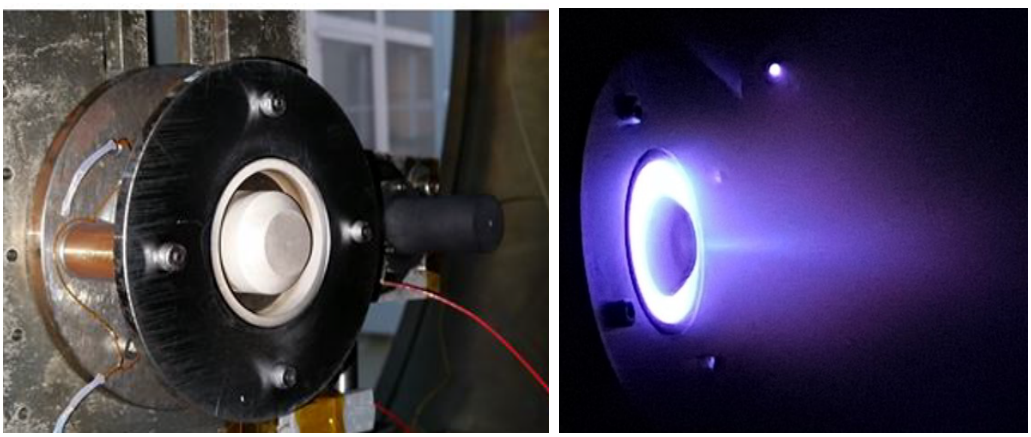

Figure 4.2. a) HK40 Hall thruster, b) HK40 Hall thruster during operation



Figure 4.3. HK40 Hall thruster mounted on thrust stand

As propellant, Argon is used during the tests. Thrust measurements are made for 1 A and 1.2 A discharge currents. Anode propellant mass flow rate is kept at 18 SCCM and cathode mass flow rate is 2.2 SCCM. Discharge power and thrust are measured for different magnet coil currents; specific impulse and thrust efficiency values are calculated. It can be seen that all values increase with increasing magnetic field at channel exit, as the plasma resistance and discharge voltage increases with increasing magnetic field strength. Performance characteristics of HK40 Hall thruster are shown in Table 4.2 and Figure 4.4. HK40 Hall thruster can generate thrust around 9.3 mN and specific impulse around 1772 s at 286 W discharge power. Thrust efficiency is between 0.25 and 0.30.

Table 4.1. Performance characteristics of HK40 Hall thruster

I_d (A)	V_d (V)	I_{in} (A)	I_{out} (A)	P_d (W)	T (mN)	I_{sp} (s)	η
1	137	0.75	1.00	137	6.2	1181	0.26
1	147	1.00	1.25	147	6.7	1277	0.29
1	153	1.25	1.50	153	6.9	1315	0.29
1	162	1.50	1.75	162	7.2	1372	0.30
1	175	1.75	2.00	175	7.5	1429	0.30
1	190	2.00	2.25	190	7.8	1486	0.30
1	201	2.25	2.50	201	8.0	1524	0.30

I_d (A)	V_d (V)	I_{in} (A)	I_{out} (A)	P_d (W)	T (mN)	I_{sp} (s)	η
1,2	150	0.75	1.00	180	7.0	1334	0.25
1,2	158	1.00	1.25	190	7.5	1429	0.28
1,2	170	1.25	1.50	204	7.8	1486	0.28
1,2	184	1.50	1.75	221	8.3	1582	0.29
1,2	200	1.75	2.00	240	8.7	1658	0.29
1,2	225	2.00	2.25	270	9.0	1715	0.28
1,2	238	2.25	2.50	286	9.3	1772	0.28

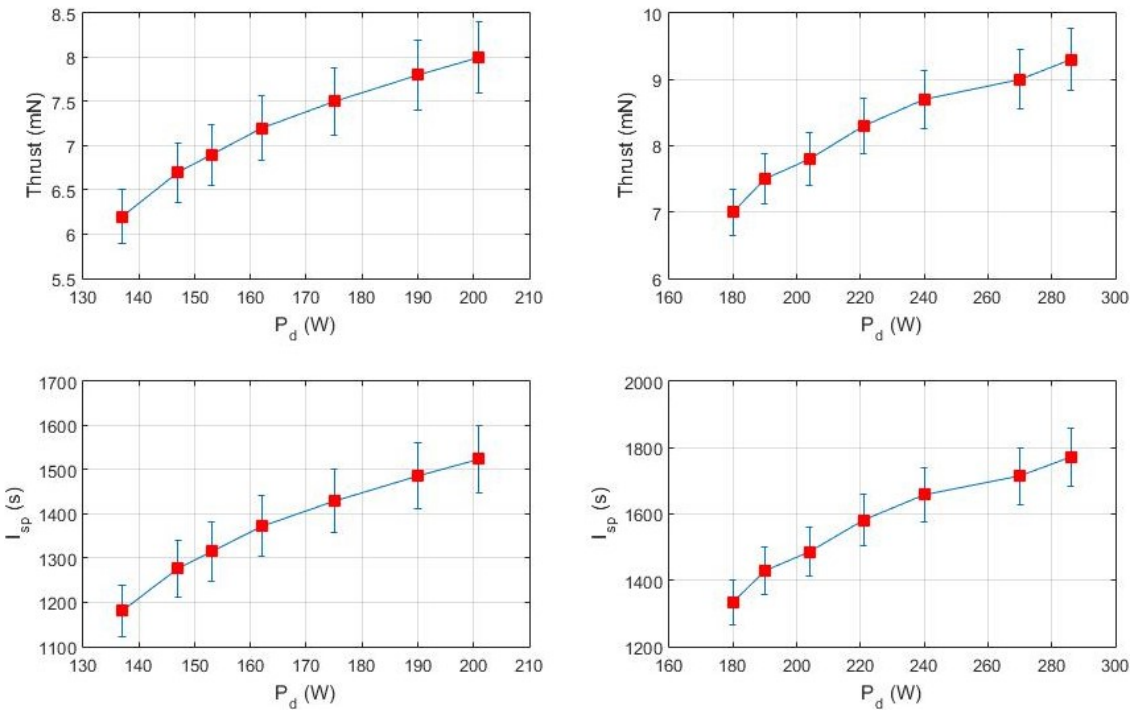

Figure 4.4. Thrust and specific impulse characteristics of HK40 Hall thruster

4.3. Microwave Electrothermal Thruster

The microwave electrothermal thruster that is developed at BUSTLab consists of a resonant cavity, which is designed to operate at TM_{011} mode for 2.45 GHz frequency. Resonance cavity is made of stainless steel (Figure 4.5). A quartz plate separates the antenna and the plasma regions. Microwaves are emitted into the cavity with a copper antenna, and a standing wave is generated within the cavity. Standing wave couples with the gas in the cavity and plasma is initiated. Propellant is injected into the cavity, and as it swirls around the plasma it is heated and then expelled through a converging-diverging nozzle [37, 38].

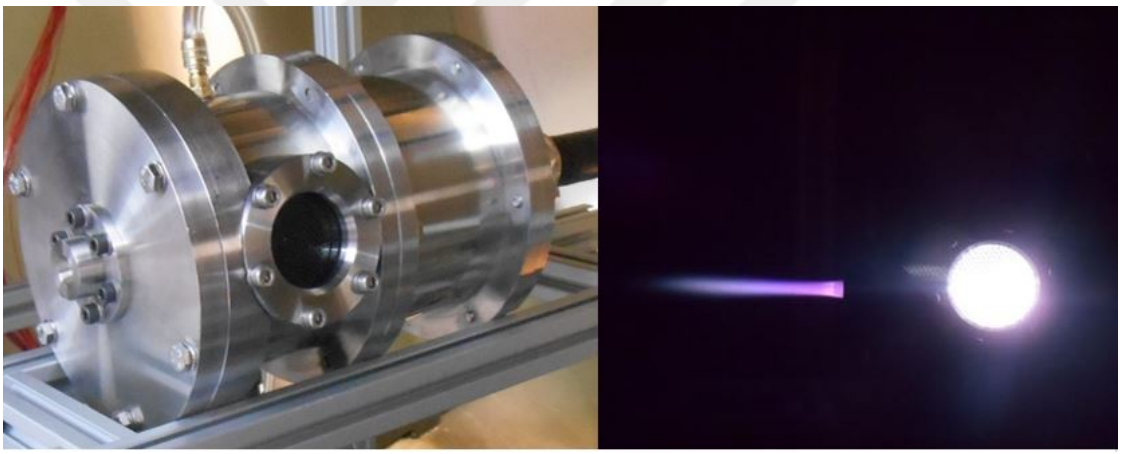

Figure 4.5. a) Microwave electrothermal thruster, b) MET during operation

Thrust measurement of MET is challenging because of the high stiffness of the microwave cable that is used to transmit the microwave power to the thruster. During the transient phase at the beginning of the operation, the microwave cable expands thermally, hence a thermal drift occurs within the system. This thermal drift is eliminated by moving the thrust stand using the linear stage that is placed under the thrust stand. After reaching the thermal steady state the thrust stand is shifted to a new position, so that the effect of the thermally expanded cable is eliminated. After this operation, calibration is repeated. During the tests it was observed that thermal drifts do not affect the stiffness of the system. However during this process the zero-thrust reference point changes, which prevents the determination of absolute applied thrust.

Therefore, thrust measurements are conducted by measuring the displacement with the LVDT first, and then by measuring the zero-thrust displacement point by turning off the power input and propellant gas flow to the thruster. As both measurements are conducted one after the other rapidly, thermal drift is assumed to not affect the measurement. For each measurement this process is repeated. The thrust stand responses highly linear with respect to the applied force. Also, hysteresis between measurements is negligible. MET while mounted on the thrust stand is shown in Figure 4.6.

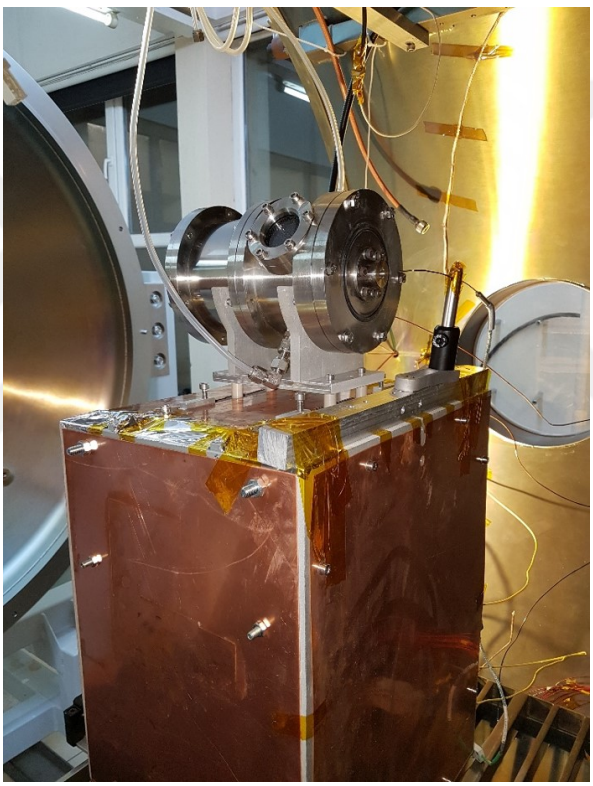

Figure 4.6. MET mounted on the thrust stand

During the measurements, the BUSTLab MET system is operated using Argon gas for mass flow rates of 178 to 356 mg/s and at a power level of 200 W. For each gas flow rate, the thrust is measured for the case of no microwave energy deposition (cold gas case), and for the case of 200 W of microwave power delivered to the gas. For the given flow rates, the chamber pressure and the measured thrust levels are presented in Figure 4.7 for the same two cases. The measured thrust values versus mass flow rate are shown in Figure 4.8 for cold gas and 200 W power delivered cases.

	Cold Gas		Hot Gas	
mfr [mg/s]	p_c [torr]	τ [mN]	p_c [torr]	τ [mN]
178	252	85	405	170
208	300	102	480	180
237	347	120	570	220
267	393	138	634	250
297	440	150	700	260
327	486	168	760	270
356	534	187	830	280

Figure 4.7. Performance characteristics of MET

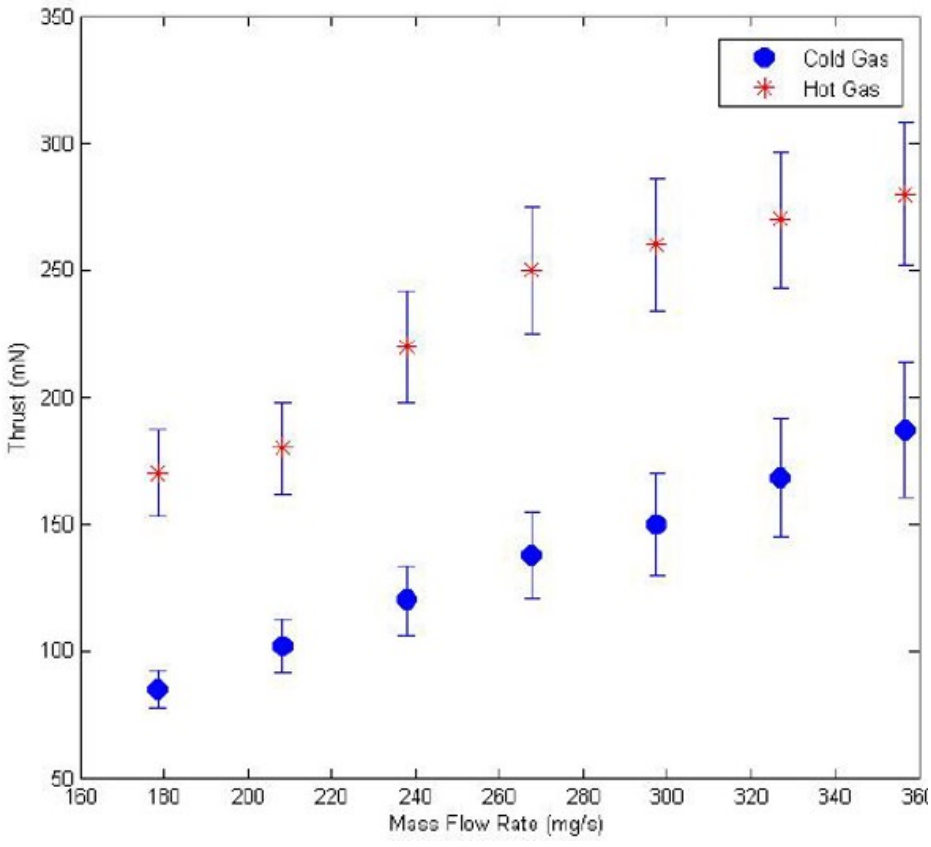

Figure 4.8. Thrust characteristics of MET

4.4. UK90 Hall Thruster

Preliminary tests of UK90 Hall thruster are conducted in vacuum chamber as shown in Figure 4.9. Thruster is operated at mass flow rates up to 70 SCCM argon and discharge current up to 5 A. Discharge plume is generated as expected. Propellant injection to the discharge channel is shown in Figure 4.10. A near axisymmetric discharge is achieved. It was seen that internal cathode couples well with the magnetic topology of the Hall thruster. Internal cathode is operated at different magnetic field strengths and cathode plume characteristics are investigated. As shown in Figure 4.11, cathode plume can be focused with axial magnetic field at the cathode exit. Cathode plume divergence can be changed by changing the magnetic field strength. Also, any drift in plume direction is a good indicator of an asymmetric magnetic field topology. As shown in the Figure 4.11, the magnetic topology of the thruster has a small asymmetry, which can be eliminated with more accurate assembly.

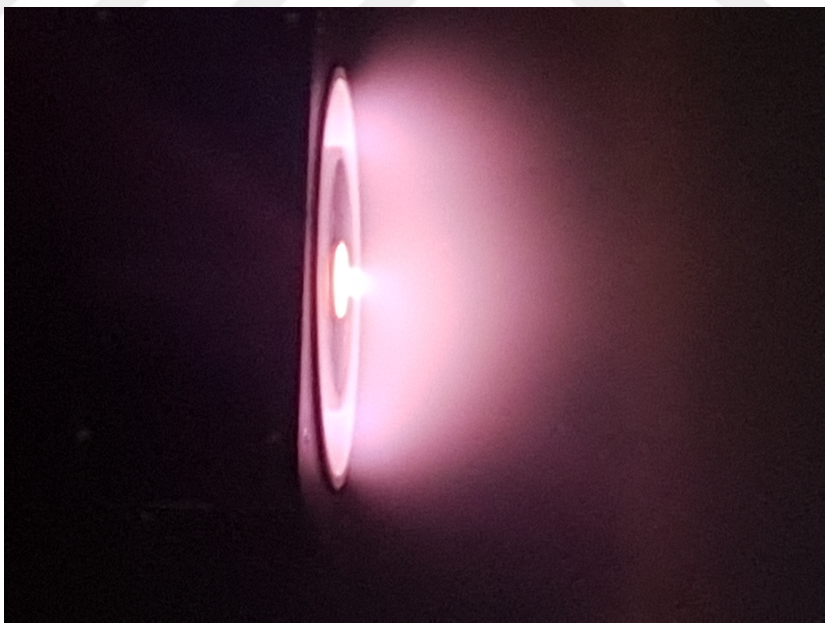

Figure 4.9. Initial operation on UK90 Hall thruster

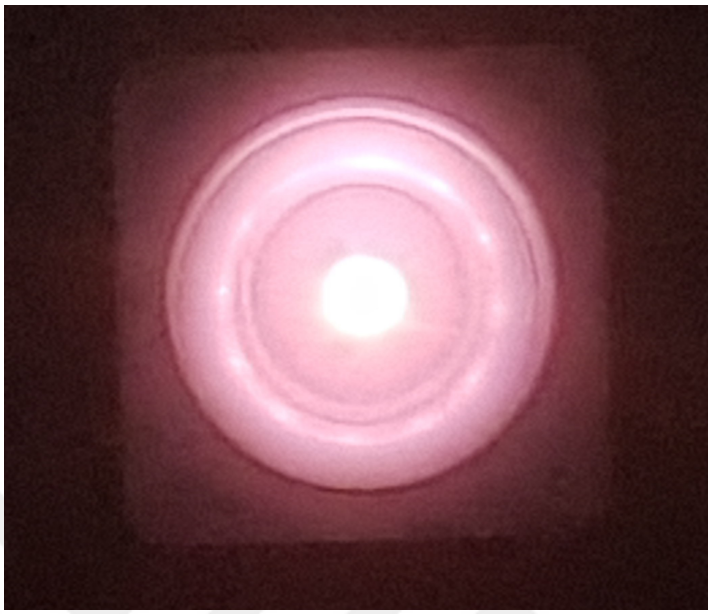

Figure 4.10. Front view of thruster operation

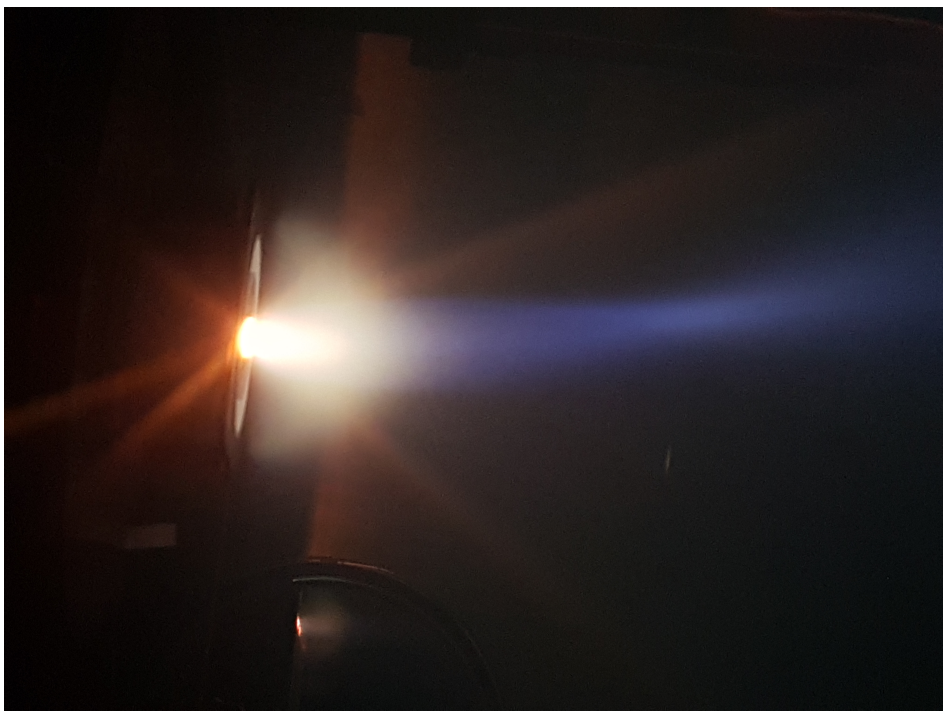

Figure 4.11. Plume of internal cathode

5. CONCLUSION

In this research, a thrust stand is developed for the thrust measurements of electric propulsion systems. The thrust stand is based on an inverted pendulum configuration and is capable of measuring thrusts at mili-Newton levels with resolutions at sub-miliNewtons. A double armed counterbalanced pendulum configuration is utilized. The double armed pendulum configuration prevents changes in the direction of the thrust vector during the thruster operation. Also, position of the thruster on the thrust stand does not affect thrust measurements with the double armed mechanism. Flexural joints are used between the pendulum parts, thus a very low friction level is achieved. Design parameters of the thrust stand are optimized according to the required sensitivity and measurement range. Most critical design parameters are pendulum arm length, flexure stiffness. During the optimization process, analytical and numerical models for the thrust stand are developed. By using these models, several parametric studies are conducted for different design variables. Effects of different design parameters on the measurement range and sensitivity are investigated. Also, the transient behavior of the thrust stand is investigated. Natural frequency of the pendulum mechanism is around 0.25 Hz. As natural frequency is much lower than the frequency of the vibrations (1 Hz) within the vacuum chamber that are caused by the cyropumps, transmission of these external vibrations to the pendulum structure is reduced. So that, the pendulum structure acts as a vibration isolation mechanism. Pendulum motion is damped with an Eddy current magnetic damper mechanism.

Deflection of the pendulum structure is measured with an LVDT displacement sensor. The LVDT has a core insert part, which is attached to the upper platform of the pendulum through a 2D linear stage. Position of the core part is adjusted with the linear stage. LVDT is attached to the bottom platform of the pendulum. Since LVDT sensor measures the displacement between upper and bottom platforms of the pendulum structure, the displacement measurement has limited noise that is caused by the external vibrations.

In situ calibration of the thrust stand can be performed within high vacuum inside the vacuum chamber. Calibration is performed by applying a dummy thrust to the pendulum and measuring the response with a displacement sensor. The dummy thrust is applied through a load cell. The load cell is mounted on a linear stage and can be pushed towards the upper platform of the pendulum. Several calibration measurements are performed for different load levels at each calibration sequence.

Counterweights are used to balance thruster weight. Counterweight mass affect the sensitivity of the system as it has an effect on the stability of the pendulum. By adjusting the counterweight, thrust measurement range and sensitivity of the thrust stand can be adjusted according to different thruster types. Thruster cables and pipes are hanged down from an upper bar that is attached to the vacuum chamber, so that cables and pipes are connected to the thrusters in the perpendicular direction to the thrust direction. Thus, the effect of the cables and pipes on the thrust measurements are reduced.

Thrust stand is thermally insulated from the thruster and the vacuum chamber, thus thrust stand temperature can be kept stable. Also, the thruster is insulated electrically from the thrust stand. Thrust stand and control hardware are also insulated from the electromagnetic waves in the vacuum chamber, which is critical when testing RF and microwave thrusters.

By using the thrust stand, operational characteristics of HK40 Hall thruster and the BUSTLab MET are measured. From the thrust measurements, specific impulse and efficiency values are calculated. HK40 Hall thruster is operated at 1 A and 1.2 A discharge currents with different magnetic field strengths and power levels. Measured thrust values are between 6.2 mN and 9.3 mN. Specific impulse of the thruster varies between 1181 s and 1772 s for different current and power levels. Anode efficiency of the thruster is between 0.25 and 0.30. MET is operated as mass flow rates of 178 to 356 mg/s and at a microwave power level of 200 W. When no microwave power is transmitted to the thruster, measured thrust values are between 85 and 187 mN. When 200 W power is utilized, measured thrust values varies between 170 and 280 mN.

In this study, also an SPT type Hall thruster, which is called UK90 Hall thruster, with discharge power level of 1.5 kW is designed and manufactured. This Hall thruster utilizes an internal cathode. Internal cathode configuration decreases beam divergence and provides a symmetric plume, so that an efficiency increase is achieved. Magnetic focusing of the internal cathode is tested in vacuum chamber. It was seen that magnetic topology of the thruster successfully focuses the electron beam of the cathode. Design parameters of the thruster such as channel diameter, channel width and channel length are optimized with scaling analysis. Operational parameters of other Hall thrusters around the world are investigated by using scaling laws in the literature. From the investigations, theoretical thrust and efficiency levels of the thruster are calculated.

Magnetic circuit of the thruster is investigated through numerical analysis. A magnetic circuit design is developed and magnetic circuit geometry is optimized through the numerical analysis. In the thruster design, four outer electromagnets and a single inner electromagnet are used. Magnetic shielding concept is investigated and applied to the thruster. In magnetic shielding concept, parallel magnetic field lines to the channel walls are used, so that these magnetic field lines collect the cold electrons from the anode region and transfer them along the channel walls. The channel walls are protected from high energy electron collisions, thus heat flux to the channel walls and erosion are decreased. The magnetic field strength at the center of the channel exit is determined to be 200 G. Magnetic field measurements are conducted with a Gaussmeter. Required current levels for the electromagnets are determined with the magnetic field measurements.

During the scaling process, heat fluxes from the channel plasma to channel walls and anode are calculated. Numerical thermal analysis is conducted according to these flux values. Temperature distribution and heat flux in the thruster are investigated. According to the thermal analysis results, thruster design is improved. It was seen that temperatures at the inner magnet region and discharge channel increase to high values. Therefore, the channel parts are insulated from the magnetic circuit parts with ceramic insulators and mounted on a copper heat sink. The copper heat sink is attached to a copper radiator for heat extraction from the channel parts. Conventional insulated

magnet wires cannot be used in the inner magnet because of high temperature. Therefore, a bare copper wire is wrapped around a ceramic cylinder and used as the inner electromagnet. Preliminary Hall thruster tests are performed successfully.

Hall thrusters utilize hollow cathodes to provide ionization and neutralization. The BUSTLab hollow cathode is analyzed and tested extensively. Thermal analyses are conducted for different heater designs. Temperature distribution, heat flux and required power for the ignition of the cathode are investigated. With these analyses, the heater design of the cathode is improved. Also, an electrical potential model is developed to investigate the electrical potential distribution within the orifice region of the cathode. During this study, several different cathode designs are built and tested many times. With these studies, a hollow cathode design close to a flight model is obtained.

Also, a new RF ion thruster design is built and tested. With this new design, various problems that are encountered with the previous RF thrusters such as arcing problems at the electrical connections of the grids are solved. The RF ion thruster utilizes an alumina discharge channel with a diameter of 80 mm. A copper RF antenna is utilized to ionize the propellant inside the discharge chamber. A ceramic propellant injector is designed to inject the propellant to the discharge chamber through radially directed holes. The injector has a hollow shape, so that it can sustain higher pressures in the hollow section and prevents plasma back flow to propellant lines. Accelerator grids are manufactured with water jet cutting and covered with teflon covers for electrical insulation. During the tests no arcing problems are encountered. The thruster is covered with a perforated steel cover to avoid RF leakage. In this study, the developed RF ion thruster design is presented in detail. Preliminary tests of the RF thruster are conducted.

5.1. Future Work

So far, thrust measurements are performed successfully with the HK40 Hall thruster and the MET. However, some problems are encountered during the tests of the RF ion thruster, such as electromagnetic coupling with the RF antenna. Propellant delivery system to the RF thruster also needs improvements to avoid plasma backflow to the propellant line. In order to avoid plasma backflow, a Teflon nozzle part is placed inside the propellant line. More tests should be conducted for the propellant injection system. Coating of the inner surface of discharge chamber caused by the sputtered material from the grids proved to be problematic, as coating acts as a Faraday cage and prevents RF coupling with the discharge plasma. Coating problem may be solved by improving the propellant diffusion and adjusting the pressure and propellant flow within the discharge chamber. Arcing problems of the grids are solved after a couple ignitions, however a better machining operation may be needed for the hole drilling operation of the grids. Long power lines prove to be problematic. Shorter power lines should be used, in fact if possible RF power supply systems should be integrated to the thruster. Also, different RF frequencies may be investigated. Lower frequencies are suggested for better RF coupling. More tests and theoretical analysis are needed for the RF thruster. Ion optics investigations are necessary for grid and discharge chamber optimization.

Similar thrust measurement problems are also encountered with the MET. As the microwave power is delivered through thick microwave cables, thrust measurements proved to be very difficult, even impossible as the cable heats with the microwave power. Therefore, an inverse approach is used with the thrust measurements of the MET. Thrust is measured by turning off the thruster immediately and measuring the difference between the thrust stand responses. This method proved to be practical, however it increases measurement errors and slows down the tests. Therefore, a new power supply system may improve measurements. Microwave power supply may be integrated to the thruster.

Thrust stand has also several drawbacks such as the available manufacturing methods. Pendulum structure should be manufactured with tighter tolerances with better quality. The displacement sensor is mounted and adjusted with a homemade 2D linear stage. A more precise linear stage may improve measurements. Also, the load cell is mounted on a homemade 1D linear stage, which proved to be problematic during the calibration procedure. A better motion mechanism is needed. Thrust stand is controlled via Arduino micro controller, which has a limited input and output resolution. A more competent controller with higher resolution is needed.

UK90 Hall thruster is at the preliminary test stage. Power supply shortage was encountered during the preliminary tests. More tests should be conducted with a more adequate power supply, which can deliver enough discharge voltage at the required high current levels. Thermal characteristics of the thruster during operation may be investigated. Also, plasma measurements may be performed with the thruster using the available plasma measurement devices at BUSTLab such as Langmuir probe, Faraday probe and RPA. Initial Hall thruster prototype utilizes 1018 steel magnetic parts. Better magnetic topology may be achieved with Hiperco parts.

REFERENCES

1. Florenz, R. E., *The X3 100-kW Class Nested-Channel Hall Thruster: Motivation, Implementation and Initial Performance*, Ph.D. Thesis, The University of Michigan, MI, USA, 2014.

2. Sutton, G. P. and O. Biblarz, *Rocket Propulsion Elements*, J. Wiley and Sons, New York, NY, USA, 2010.

3. Martinez-Sanchez, M. and J. E. Pollard, "Spacecraft Electric Propulsion-An Overview", *Journal of Propulsion and Power*, Vol. 14:5, pp. 688–699, 1998.

4. Turkoz, E., *Numerical Model for Axisymmetric Inductively Coupled Plasma (ICP) in Radio-Frequency (RF) Ion Thrusters*, M.S. Thesis, Bogazici University, Bebek, Istanbul, Turkey, May 2014.

5. Hofer, R. R., "Magnetic Shielding in Hall Thrusters: Breakthrough Space Propulsion Technology for the 21st Century", *Plasma Science and Engineering Seminar Series*, March 20 2013.

6. Goebel, D. M. and I. Katz, *Fundamentals of Electric Propulsion: Ion and Hall Thrusters*, J. Wiley and Sons, Oxford, 2008.

7. Lev, D. *et al.*, "The Technological and Commercial Expansion of Electric Propulsion in the Past 24 Years", 35nd *International Electric Propulsion Conference*, Atlanta, GA, USA, October 2017, IEPC-2017-242.

8. Pancotti, A., T. Haag, S. King and M. Walker, "Recommended Practices in Thrust Measurements", 33rd *International Electric Propulsion Conference*, Washington, DC, USA, October 2013, IEPC-2013-440.

9. Luna, J. P., C. Edwards, J. G. Del Amo and B. Hughes, "Development status

of the ESA micro-Newton thrust balance", 32nd *International Electric Propulsion Conference*, Wiesbaden, Germany, September 2011, IEPC-2011-011.

10. Packan, D., J. Bonnet and S. Rocca, "Thrust Measurements with the ONERA Micro-Newton Balance", 31st *International Electric Propulsion Conference*, Ann Arbor, MI, USA, September 2009, IEPC-2009-185.

11. Xu, K. G. and M. L. R. Walker, "High-power, null-type, inverted pendulum thrust stand", *Review of Scientific Instruments*, Vol. 80, No. 5, 2009.

12. Neumann, A., J. Sinskes and H.-P. Harmann, "The 250mN Thrust Balance for the DLR Goettingen EP Test Facility", 33rd *International Electric Propulsion Conference*, Washington, DC, USA, October 2013, IEPC-2013-211.

13. Harmann, H.-P., H. Dartsch and E. Werner, "Low Drift Thrust Balance with High Resolution", 34th *International Electric Propulsion Conference*, Hyogo-Kobe, Japan, July 2015, IEPC-2015-257.

14. Hey, F. G., A. Keller, D. Papendorf, C. Braxmaier, M. Tajmar, U. Johann and D. Weise, "Development of a Highly Precise Micro-Newton Thrust Balance", 33rd *International Electric Propulsion Conference*, Washington, DC, USA, October 2013, IEPC-2013-275.

15. Borras, E. B. and B. Hughes, "ISO17025 Accreditation of the ESA Micro-Newton Thrust Balance", 34th *International Electric Propulsion Conference*, Hyogo-Kobe, Japan, July 2015, IEPC-2015-259.

16. Cara, D. D., L. Massotti, S. Cesare, F. Musso, G. Castorina, D. Feili and B. Lotz, "Performance Verification of the μNRIT-2.5 Thruster on the Nanobalance Facility", 32nd *International Electric Propulsion Conference*, Wiesbaden, Germany, September 2011, IEPC-2011-013.

17. Frollani, D., M. Coletti and S. B. Gabriel, "Thrust Measurements on the T6 Hol-

low Cathode Thruster Using Direct Thrust Balances", 33rd *International Electric Propulsion Conference*, Washington, DC, USA, October 2013, IEPC-2013-129.

18. Ciaralli, S., M. Coletti, S. B. Gabriel, F. Transform, P. P. Thruster, P. Sciences and P. Sciences, "μ-PPTs Diagnostics: A High Accuracy Impulsive Thrust Balance", 33rd *International Electric Propulsion Conference*, Washington, DC, USA, October 2013, IEPC-2013-165.

19. Seifert, B., A. Reissner, N. Buldrini, F. Plesescu, A. Bulit and E. B. Borras, "Verification of the FOTEC μN Thrust Balance at the ESA Propulsion Lab", 34th *International Electric Propulsion Conference*, Hyogo-Kobe, Japan, July 2015, IEPC-2015-258.

20. Marhold, K. and M. Tajmar, "Direct Thrust Measurement of In-FEEP Clusters", 29th *International Electric Propulsion Conference*, Princeton, NJ, USA, October 2005, IEPC-2005-235.

21. Koizumi, H., K. Komurasaki and Y. Arakawa, "Development of Thrust Stand for Low Impulse Measurement from Microthrusters", *Review of Scientific Instruments*, Vol. 75, No. 10, pp. 3185–3190, October 2004.

22. Turan, N., U. Kokal, H. Kurt and M. Celik, "Experimental Study of the Effects of the Cathode Position and the Electrical Circuit Configuration on the Operation of HK40 Hall Thruster and BUSTLab Hollow Cathode", 52nd *Joint Propulsion Conference*, Salt Lake City, UT, USA, July 2016, AIAA-2016-4834.

23. Conversano, R. W., D. M. Goebel, R. R. Hofer, I. G. Mikellides, I. Katz and R. E. Wirz, "Magnetically Shielded Miniature Hall Thruster: Design Improvement and Performance Analysis", 34th *International Electric Propulsion Conference*, Hyogo-Kobe, Japan, July 4-10 2015, IEPC-2015-100.

24. Kokal, U., N. Turan, H. Kurt and M. Celik, "Thermal Analysis and Testing of Different Designs of Lanthanum Hexaboride Hollow Cathodes", *8th International*

Conference on Recent Advances in Space Technologies (RAST), Istanbul, Turkey, June 2017.

25. Powell, R. W., Ho, C. Y. and Liley, P. E., *Thermal Conductivity of Selected Materials*, National Bureau of Standards, 1966.

26. Kwon, K., *A Novel Numerical Analysis of Hall Effect Thruster and Its Application in Simultaneous Design of Thruster and Optimal Low-Thrust Trajectory*, Ph.D. Thesis, Georgia Institute of Technology, GA, USA, 2010.

27. Gallimore, A. D., "What We Have Learned by Studying The P5 Hall Thruster", *AIP Conference Proceedings - Rarefied Gas Dynamics:* 23rd *International Symposium*, Vol. 663, pp. 533–540, 2003.

28. Manzella, D., C. Sarmiento, J. Sankovic and T. Haag, "Performance Evaluation of the SPT-140", 25th *International Electric Propulsion Conference*, Cleveland, OH, USA, August 24-28 1997, IEPC-1997-059.

29. Stuckey, P., C. Clauss, M. Day, V. Murashko, N. Maslennikov, R. Kozubsky, R. Gnizdor, V. Kim, D. Kozlov and D. Grdlichko, "SPT-140 High Performance Hall System (HPHS) Development", 34th *Joint Propulsion Conference*, Cleveland, OH, USA, July 13-15 1998.

30. Loyan, A. V. and T. A. Maksymenko, "Performance Investigation of SPT-20M Low Power Hall Effect Thruster", 30th *International Electric Propulsion Conference*, Florence, Italy, September 17-20 2007, IEPC-2007-100.

31. Mitrofanova, O. A., R. Y. Gnizdor and V. M. Murashkı, "New Generation of SPT-100", 32nd *International Electric Propulsion Conference*, Wiesbaden, Germany, September 11-15 2011, IEPC-2011-041.

32. Sankovic, J. M., J. A. Hamley and T. W. Haad, "Performance Evaluation of the Russian SPT-100 Thruster at NASA LeRC", 23rd *International Electric Propul-*

sion Conference, Seattle, WA, USA, September 13-16 1993, IEPC-1993-094.

33. *Space Mission Engineering: The New SMAD*, Space Technology Library, 2011.

34. Macdonald, M. and V. Badescu, *The International Handbook of Space Technology*, Springer, 2014.

35. Cantwell, B., A. Karabeyoglu and D. Altman, "Recent Advances in Hybrid Propulsion", *International Journal of Energetic Materials and Chemical Propulsion*, Vol. 9, No. 4, 2010.

36. Stuhlinger, E., *Ion Propulsion for Space Flight*, McGraw Hill, New York, NY, USA, 1964.

37. Yildiz, S. and M. Celik, "Experimental Performance Analysis of the BUSTLab Microwave Electrothermal Thruster", 52nd *Joint Propulsion Conference*, Salt Lake City, UT, USA, July 2016, AIAA-2016-4949.

38. Yildiz, S., U. Kokal, and M. Celik, "Preliminary Thrust Measurement Results of the BUSTLab Microwave Electrothermal Thruster", 53nd *Joint Propulsion Conference*, Atlanta, GA, USA, July 2017, AIAA-2017-4725.

39. Jahn, R. G., *Physics of Electric Propulsion*, McGraw Hill, New York, NY, USA, 1968.

40. Jahn, R. G. and E. Y. Choueiri, *Electric Propuslsion, Encyclopedia of Physical Science and Technology, Third Edition*, Vol. 5, Academic Press, New York, 2002.

41. Thomson, J. J., "Nobel Lecture, December 11, 1906, In Nobel Lectures: Physics, 1901-1921", *Elsevier*, pp. 145–153, 1967.

42. Choueiri, E. Y., "A Critical History of Electric Propulsion: The First 50 Years (1906-1956)", *Journal of Propulsion and Power*, Vol. 20, pp. 193–203, 2004.

43. Casaregola, C., "Electric Propulsion for Satellite Keeping and Electric Orbit Raising on Eutelsat Platforms", 34th *International Electric Propulsion Conference*, Hyogo-Kobe, Japan, July 4-10 2015, IEPC-2015-97.

44. Korkmaz, O., S. Jahanbakhsh, M. Celik and H. Kurt, "Space Propulsion Research Vacuum Facility of the Bogazici University Space Technologies Laboratory", *7th International Conference on Recent Advances in Space Technologies (RAST)*, Istanbul, Turkey, June 2015.

45. Tartler, B. and M. Martinez-Sanchez, *Construction and Performance of an Inverted Pendulum Thrust Balance*, Master's Thesis, MIT, May 2010.

46. Kokal, U. and M. Celik, "Development of BUSTLab Thrust Stand for mili-Newton Level Thrust Measurements of Electric Propulsion Systems", 35nd *International Electric Propulsion Conference*, Atlanta, GA, USA, October 2017, IEPC-2017-317.

47. Kokal, U., H. Kurt and M. Celik, "Development of a mili-Newton Level Thrust Stand for Thrust Measurements of Electric Propulsion Systems", *8th International Conference on Recent Advances in Space Technologies (RAST)*, Istanbul, Turkey, June 2017.

48. Measurement Specialties Inc., *The LVDT: construction and principles of operation*, 1000 Lucas Way, Hampton, VA 23666, United States, April 2013.

49. Cunningham, R. E., "Passive Eddy-Current Damping as a Means of Vibration Control in Cyrogenic Turbomachinery", *NASA Technical Paper*, Vol. 2562, 1986.

50. Jameson, K. K., *Investigation of Hollow Cathode Effects on Total Thruster Efficiency in a 6 KW Hall Thruster*, Ph.D. Thesis, University of California, Los Angeles, 2008.

51. Turan, N., *Experimental Investigation of the Effects of Cathode Position on*

HK40 Hall Effect Thruster Performance and Cathode Coupling, Master's Thesis, Bogazici University, Bebek, Istanbul, Turkey, December 2016.

52. Liang, R., *The Combination of Two Concentric Discharge Channels into a Nested Hall-Effect Thruster*, Ph.D. Thesis, The University of Michigan, Ann Arbor MI, USA, 2013.

53. Xu, K. G. and M. L. R. Walker, "Effect of External Cathode Azimuthal Position on Hall Effect Thruster Plume and Diagnostics", *Journal of Propulsion and Power*, Vol. 30/2, pp. 506–513, March-April 2014.

54. Hofer, R. R., L. K. Johnson and D. M. Goebel, "Effects of an Internally-Mounted Cathode on Hall Thruster Plume Properties", *IEEE Transactions on Plasma Science*, Vol. 36, October 2008.

55. Hofer, R. R., L. K. Johnson, D. M. Goebel and D. J. Fitzgerald, "Effects of an Internally-Mounted Cathode on Hall Thruster Plume Properties", 42nd *Joint Propulsion Conference*, Sacramento CA., USA, July 9-12 2006, AIAA-2006-4482.

56. Szabo, J. *et al.*, "Eight Kilowatt Hall Thruster System Characterization", 33rd *International Electric Propulsion Conference*, The George Washington University, Washington, D.C., USA, October 6-10 2013, IEPC-2013-317.

57. Sommerville, J. D. and L. B. King, "Effect of Cathode Position on Hall-Effect Thruster Performance and Cathode Coupling Voltage", 43rd *Joint Propulsion Conference*, Cincinnati, OH, USA, July 8-11 2007, AIAA-2007-5174.

58. Sommerville, J., *Hall-Effect Thruster Cathode Coupling: The Effect of Cathode Position and Magnetic Field Topology*, Ph.D. Thesis, Michigan Technological University, Houghton, MI, USA, 2009.

59. Tilley, D. L., K. H. de Grys and R. M. Myers, "Hall Thruster-Cathode Coupling", 35nd *Joint Propulsion Conference*, Los Angeles, CA, USA, June 1999, AIAA-1999-

2865.

60. Beiting, E. J., W. A. Cox, K. D. Diamant, R. Spektor, B. Pote and V. Hruby, "Busek BHT-1500 External vs Center Cathode EMC Study", 34th *International Electric Propulsion Conference*, Hyogo-Kobe, Japan, July 4-10 2015, IEPC-2015.

61. Diamant, K. D. *et al.*, "Performance and Plume Characterization of the BHT-1500 Hall Thruster", 34th *International Electric Propulsion Conference*, Hyogo-Kobe, Japan, July 4-10 2015, IEPC-2015-69.

62. Jameson, K. K., D. M. Goebel, R. R. Hofer and R. M. Watkns, "Cathode Coupling in Hall Thrusters", 30th *International Electric Propulsion Conference*, Florence, Italy, September 17-20 2007, IEPC-2007-278.

63. Kokal, U., N. Turan, H. Kurt and M. Celik, "Development of the New BUST-Lab Hall Thruster with Internal Coaxial Hollow Cathode", 53rd *Joint Propulsion Conference*, Atlanta, GA, USA, July 2017, AIAA-2017-4810.

64. Shagayda, A. A., "On Scaling of Hall Effect Thrusters", 33rd *International Electric Propulsion Conference*, The George Washington University, Washington, D.C., USA, October 6-10 2013, IEPC-2013-056.

65. Belikov, M. B., O. A. Gorshkov and E. N. Dyshlyuk, "Development of Low-Power Hall Thruster with Lifetime up to 3000 Hours", 30th *International Electric Propulsion Conference*, Florence, Italy, September 17-20 2007, IEPC-2007-129.

66. Ahedo, E. and J. M. Gallardo, "Low Power Hall Thrusters: Physics, Technical Limitations and Design", *Micropropulsion Workshop*, May 2002.

67. Misuri, T. and M. Andrenucci, "HET Scaling Methodology: Improvement and Assessment", 44th *Joint Propulsion Conference*, Hartford, CT, USA, July 2008, AIAA-2008-4806.

68. Nurmberger, F., A. Hock and M. Tajmar, "Design and Experimental Investigation of a Low-Power Hall Effect Thruster and a Low-Current Hollow Cathode", 51st *Joint Propulsion Conference*, Orlando, FL, USA, July 27-29 2015, AIAA-2015.

69. Ahedo, E., J. M. Gallardo and M. Martinez-Sanchez., "Effects of the Radial Plasma-Wall Interaction on the Hall Thruster Discharge", *Physics of Plasmas*, Vol. 10, May 2003, 3397-3409.

70. Szabo, J. J., *Fully Kinetic Numerical Modeling of a Plasma Thruster*, Ph.D. Thesis, Massachusetts Institute of Technology, Cambridge, MA, USA, 2001.

71. Warner, N. Z., *Performance Testing and Internal Probe Measurements of a High Specific Impulse Hall Thruster*, Ph.D. Thesis, Massachusetts Institute of Technology, Cambrigde, MA, USA, 2003.

72. Conversano, R. W., D. M. Goebel, R. R. Hofer, T. S. Matlock and R. E. Wirz, "Magnetically Shielded Miniature Hall Thruster: Development and Initial Testing", 33rd *International Electric Propulsion Conference*, The George Washington University, Washington, D.C., USA, October 6-10 2013, IEPC-2013-201.

73. Kim, V., "Main Physical Features and Processes Determining the Performance of Stationary Plasma Thrusters", *Journal of Propulsion and Power*, Vol. 14, pp. 736–743, September-October 1998.

74. Hofer, R. R., *Development and Characterization of High-Efficiency, High Specific Impulse Xenon Hall Thrusters*, Ph.D. Thesis, The University of Michigan, Ann Arbor, MI, USA, 2004.

75. Mikellides, I. G., I. Katz, R. R. Hofer, D. M. Goebel, K. de Grys and A. Mathers, "Magnetic Shielding of the Acceleration Channel Walls in a Long-Life Hall Thruster", 46th *Joint Propulsion Conference*, Nashville, TN, USA, July 25-28 2010, AIAA-2010-6942.

76. de Grys, K., A. Mathers, B. Welander and V. Khayms, "Demonstration of 10,400 Hours of Operation on a 4.5 kW Qualification Model Hall Thruster", 46th *Joint Propulsion Conference*, Nashville, TN, USA, July 25-28 2010, AIAA-2010-6698.

77. Sekerak, M. J., R. R. Hofer, J. E. Polk, B. A. Jorns and I. G. Mikellides, "Wear Testing of a Magnetically Shielded Hall Thruster at 2000 s Specific Impulse", 34th *International Electric Propulsion Conference*, Hyogo-Kobe, Japan, July 4-10 2015, IEPC-2015-155.

78. Kamhawi, H. *et al.*, "Performance and Facility Background Pressure Characterization Tests of NASA's 12.5 kW Hall Effect Rocket with Magnetic Shielding Thruster", 34th *International Electric Propulsion Conference*, Hyogo-Kobe, Japan, July 4-10 2015, IEPC-2015-07.

79. Hofer, R. R., B. A. Jorns, J. E. Polk, I. G. Mikellides and J. S. Snyder, "Wear Testing of a Magnetically Shielded Hall Thruster at 3000 s Specific Impulse", 33rd *International Electric Propulsion Conference*, The George Washington University, Washington, D.C., USA, October 6-10 2013, IEPC-2013-03.

80. Hofer, R. R. *et al.*, "Development Approach and Status of the 12.5 kW HERMeS Hall Thruster for the Solar Electric Propulsion Technology Demonstration Mission", 34th *International Electric Propulsion Conference*, Hyogo-Kobe, Japan, July 4-10 2015, IEPC-2015-186.

81. Mazouffre, S., J. Vaudolon, S. Tsikata, C. Henaux, D. Harribey and A. Rossi, "Optimization of the Design of a Wall-Less Hall Thruster", 34th *International Electric Propulsion Conference*, Hyogo-Kobe, Japan, July 4-10 2015, IEPC-2015-182.

82. Kurt, H., N. Turan, U. Kokal and M. Celik, "Note: Coaxial-heater Hollow Cathode", *Review of Scientific Instruments*, Vol. 88, p. 066103, 2017.

83. Polk, J. E., D. M. Goebel, R. Watkins, K. Jameson, L. Yoneshige, J. Przyby-

lowski and L. Cho, "Characterization of Hollow Cathode Performance and Thermal Behavior", 42nd *Joint Propulsion Conference*, Sacramento, CA, USA, 2006, AIAA-2006-5150.

84. Goebel, D. M., R. M. Watkins and K. K. Jameson, "LaB6 Hollow Cathodes for Ion and Hall Thrusters", *Journal of Propulsion and Power*, Vol. 23, pp. 552–558, 2007.

85. Warner, D. J., *Advanced Technologies for Next Generation Electric Propulsion Technology*, Master's Thesis, Air Force Institute of Technology, Dayton, OH, USA, December 2008.

86. Warner, D. J., R. D. Branam and W. A. Hargus, "Ignition and Plume Characteristics of Low-Current Cerium and Lanthanum Hexaboride Hollow Cathodes", *Journal of Propulsion and Power*, Vol. 26, pp. 130–134, 2010.

87. Goebel, D. M. and E. Chu, "High Current Lanthanum Hexaboride Hollow Cathodes for High Power Hall Thrusters", 32nd *International Electric Propulsion Conference*, Wiesbaden, Germany, September 11-15 2011, IEPC-2011-053.

88. Courtney, D. G., *Development and Characterization of a Diverging Cusped Field Thruster and a Lanthanum Hexaboride Hollow Cathode*, Master's Thesis, Massachusetts Institute Of Technology, Cambridge, MA, USA, May 2008.

89. Jacobson, D. and E. Storms, "Work Function Measurement Of Lanthanum-Boron Compounds", *IEEE Transactions on Plasma Science*, Vol. 6, pp. 191–199, 1978.

90. Goebel, D. M. and R. M. Watkins, "Compact Lanthanum Hexaboride Hollow Cathode", *Review of Scientific Instruments*, Vol. 81, p. 083504, 2010.

91. Hofer, R. R., *Evaluation of Low-Current Orificed Hollow Cathodes*, Ph.D. Thesis, The University of Michigan, MI, USA, 1999.

92. Neamen, D. A., *Semiconductor Physics and Devices*, McGraw Hill Higher Education, 2003.

93. Mikellides, I. G., I. Katz, D. M. Goebel and J. E. Polk, "Hollow Cathode Theory and Experiment. II. A Two-Dimensinal Theoretical Model of the Emitter Region", *Journal Of Applied Physics*, Vol. 98, 2005.

94. Ozturk, A. E., E. Turkoz, A. Ozgen and M. Celik, "Design and Thermal Analysis of the Insert Region Heater of a Lanthanum Hexaboride Hollow Cathode", *6th International Conference on Recent Advances in Space Technologies (RAST)*, Istanbul, Turkey, June 2013.

95. Turan, N., U. Kokal and M. Celik, "Experimental Investigation of the Effects of Cathode Current on HK40 Hall Thruster Operation", *5th Space Propulsion Conference*, Rome, Italy, May 2016, SP2016-3125333.

96. Jahanbakhsh, S., Satir, M. and Celik, M., "Study of Electron Current Extraction from a Radio Frequency Plasma Cathode Designed as a Neutralizer for Ion Source Applications", *Review of Scientific Instruments*, Vol. 87, p. 02B922, 2016.

97. Turkoz, E., Sik, F. and Celik, M., "Numerical Simulation of Particle Trajectories in Ion Thruster Grid Region Plasma using a PIC-DSMC Code", *European Physical Journal*, 2015.

98. Kokal, U., Turan, N., Kurt, H. and Celik, M., "Design Improvements and Experimental Measurements of BURFIT-80 RF Ion Thruster", 53rd *Joint Propulsion Conference*, Atlanta, GA, USA, July 2017, AIAA-2017-4891.

99. Turkoz, E. and Celik, M., "2D Fluid Model for Axisymmetric RF Ion Thruster Cylindrical Discharge Chamber", 49th *Joint Propulsion Conference*, San Jose, CA, USA, July 2013, AIAA-2013-4110.

100. Jahanbakhsh, S., Satir, M. and Celik, M., "Study of Electron Current Extraction

from a Radio Frequency Plasma Cathode Designed as a Neutralizer for Ion Source Applications", 16th *International Conference on Ion Sources*, New York, NY, USA, August 2015.

101. Satir, M., Sik, F., Turkoz, E. and Celik, M., "Design of the Retarding Potential Analyzer to be used with BURFIT-80 Ion Thruster and Validation Using PIC-DSMC Code", 7th *International Conference on Recent Advances in Space Technologies (RAST)*, Istanbul, Turkey, June 2015.

102. Turkoz, E., Sik, F. and Celik, M., "Trajectory Studies through Numerical Simulation of Ion Thruster Grid Region Plasma with PIC-DSMC Approach in 3D", 5th *Russian-German Conference on Electric Propulsion*, Dresden, Germany, September 2014.

103. Turkoz, E. and Celik, M., "2D RF Ion Thruster Modeling with Fluid Plasma and Analytical Sheath Formulation", *Space Propulsion Conference*, Cologne, Germany, May 2014.

104. Turkoz, E. and Celik, M, "2D Axisymmetric Fluid and Electromagnetic Models for Inductively Coupled Plasma (ICP) in RF Ion Thrusters", 33rd *International Electric Propulsion Conference*, The George Washington University, Washington, D.C., USA, October 6-10 2013, IEPC-2013-294.

105. Turkoz, E. and Celik, M., "Optimization of Radio-Frequency Ion Thruster Discharge Chamber Using an Analytical Model", 6th *International Conference on Recent Advances in Space Technologies (RAST)*, Istanbul, Turkey, June 2013.

106. Yavuz, B., Turkoz, E. and Celik, M., "Prototype Design and Manufacturing Method of an 8 cm Diameter RF Ion Thruster", 6th *International Conference on Recent Advances in Space Technologies (RAST)*, Istanbul, Turkey, June 2013.

APPENDIX A: BURFIT-80 ION THRUSTER DESIGN

An ion thruster called BURFIT-80 is developed at BUSTLab. So far several design iterations have been performed. According to the problems that are observed in these previous studies [4, 96–106] , a new and more advanced RF ion thruster is designed and built. Ion thruster is shown in Figure A.1.

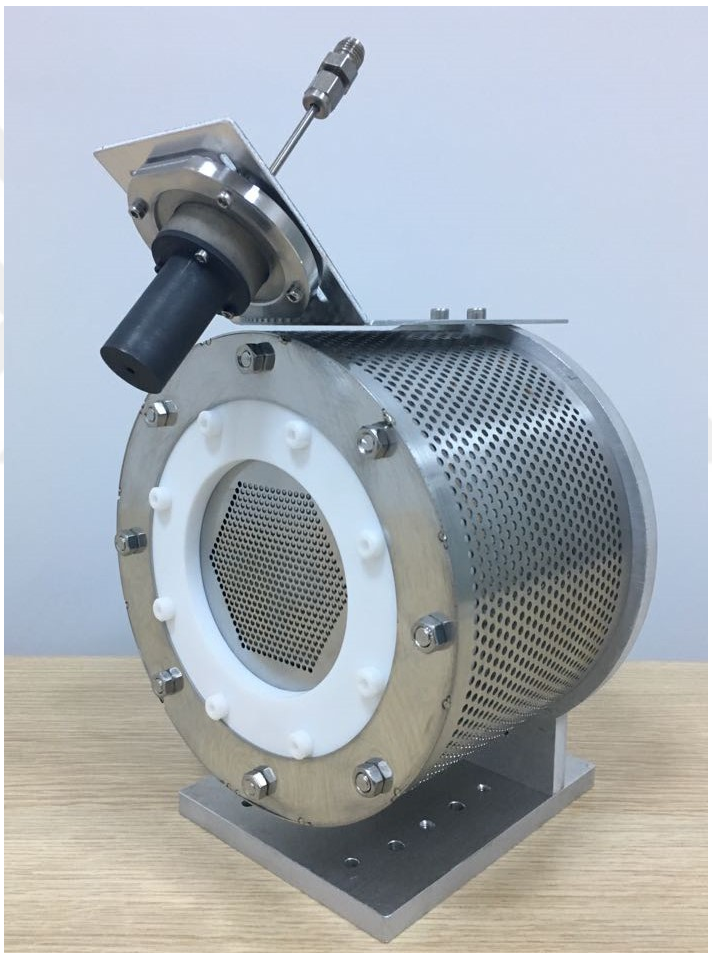

Figure A.1. BURFIT-80 Ion Thruster with Hollow Cathode

In BURFIT-80 thruster ionization is achieved in an alumina discharge chamber with 80 mm diameter and 70 mm length. Propellant is injected to the discharge chamber through a Macor diffuser part. Injector consists of two parts (FigureA.2). Inner part is connected to propellant pipe with Teflon Swagelok fittings. Helical grooves are machined on both parts. When outer part is attached to the inner part, a hollow

injector part is obtained. Propellant is injected to the discharge channel through small radial holes, while hollow region sustains higher pressure and avoids plasma leakage to the propellant lines from the discharge channel.

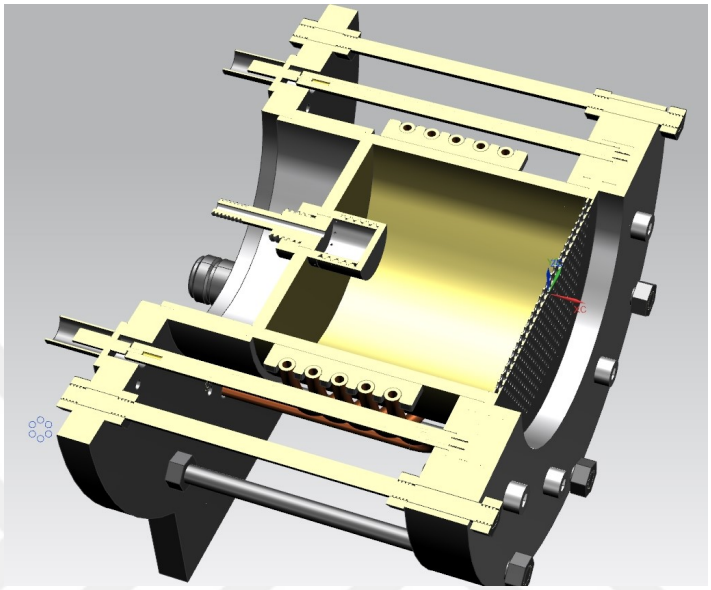

Figure A.2. Section view of BURFIT-80 Ion Thruster

Ionization is achieved by using RF waves. A radio-frequency antenna is wrapped around the discharge channel. The antenna is made of 4 mm diameter copper tube. Four Macor parts are used for positioning of the antenna as shown in Figure A.3. When radiofrequency is applied to the antenna, an oscillating magnetic field is induced in axial direction, also an oscillating electric field is induced in tangential direction. Electrons within the propellant is coupled with this electric field and accelerated into an oscillatory motion, so that they collide with the neutral atoms and an ICP plasma is generated. During the tests 13.56 MHz RF power is carried to the RF antenna through RG393 coaxial cables. In order to decrease Joule heating caused by the induced electric fields in the support backplate, a Teflon separator ring is placed between the discharge channel and the backplate. Also, thruster is covered with a 304 grade perforated stainless steel shroud to avoid RF leakage from the thruster. Holes in the cover allow radiative cooling.

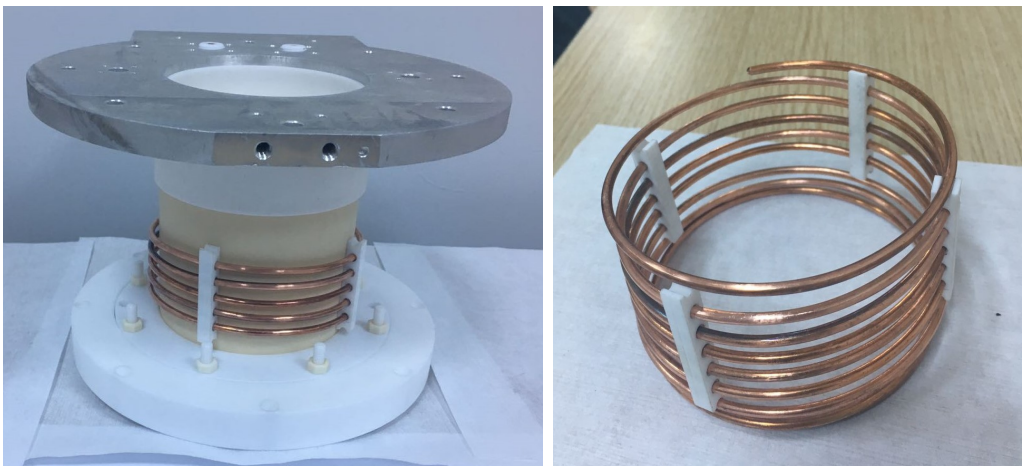

Figure A.3. Copper antenna wrapped around the discharge channel

Ion thruster utilizes two parallel flat grids. In earlier designs, stainless steel plates with 1 mm thickness are used. Later these grids are changed with molybdenum plates. Each grid has 469 holes packed in a hexagonal shape. The diameter of the screen grid holes are 2.2 mm, and the diameter of the accelerator grid holes are 1.2 mm. Grids are manufactured with water jet cutting and then surface finishing is applied. A high positive voltage (around +1000 V) is applied to screen grid, which is in contact with the plasma inside the discharge channel and provides the plasma voltage. A negative voltage (around -200 V) is applied to accelerator grid to avoid electron flow from the cathode. Ions are accelerated between the grids by the potential drop. A 1 mm thick dielectric insulation plate that is made of micanite is used to separate the grids. Each grid is attached to an aluminum ring. DC voltages are applied to the grids through these rings. Metal rings are covered with two Teflon covers. The grid assembly is fastened with zirconia screws. An exploded view of the thruster is shown in Figure A.4. In Figure A.5, BURFIT-80 is shown during operation.

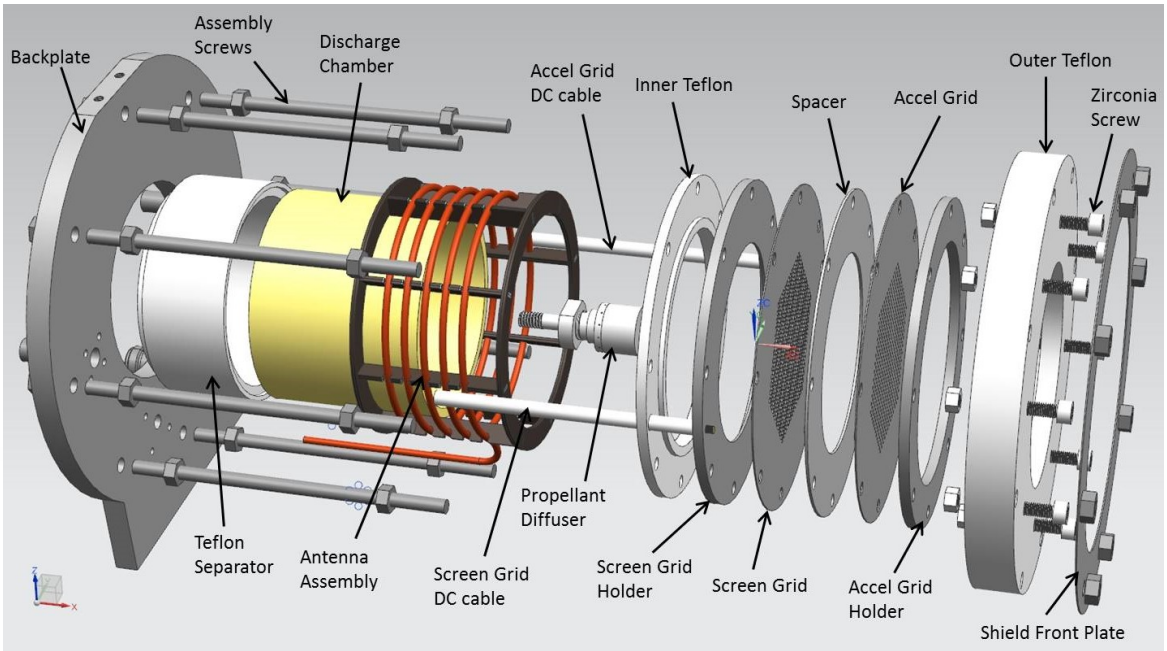

Figure A.4. Exploded view of BURFIT-80 Ion Thruster

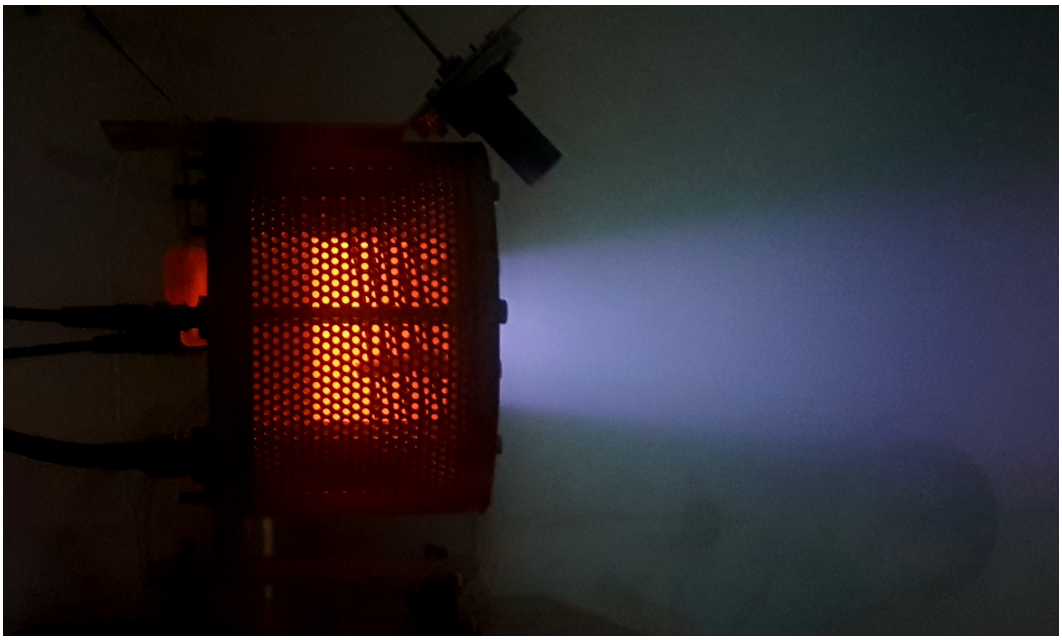

Figure A.5. Operation of BURFIT-80 Ion Thruster